OPEN ACCESS



Birds of a Feather: Resolving Stellar Mass Assembly with JWST/NIRCam in a Pair of Kindred $z \sim 2$ Dusty Star-forming Galaxies Lensed by the PLCK G165.7+67.0 Cluster

```
Patrick S. Kamieneski<sup>1</sup>, Brenda L. Frye<sup>2</sup>, Rogier A. Windhorst<sup>1</sup>, Kevin C. Harrington<sup>3,4</sup>, Min S. Yun<sup>5</sup>,
         Allison Noble 0, Massimo Pascale 0, Nicholas Foo 0, Seth H. Cohen 0, Rolf A. Jansen 0, Timothy Carleton 0,
        Anton M. Koekemoer<sup>7</sup>, Christopher N. A. Willmer<sup>2</sup>, Jake S. Summers<sup>1</sup>, Nikhil Garuda<sup>2</sup>, Reagen Leimbach<sup>2</sup>,
Benne W. Holwerda<sup>8</sup>, Justin D. R. Pierel<sup>7</sup>, Eric F. Jiménez-Andrade<sup>9</sup>, S. P. Willner<sup>10</sup>, Belén Alcalde Pampliega<sup>3</sup>, Amit Vishwas<sup>11</sup>, William C. Keel<sup>12</sup>, Q. Daniel Wang<sup>5</sup>, Cheng C
                        Madeline A. Marshall<sup>18,20</sup>, Mario Nonino<sup>21</sup>, Rafael Ortiz, III<sup>1</sup>, Alex Pigarelli<sup>1</sup>, Nor Pirzkal<sup>7</sup>,
                     Maria del Carmen Polletta<sup>22</sup>, Aaron S. G. Robotham<sup>17</sup>, Russell E. Ryan, Jr.<sup>7</sup>, and Haojing Yan<sup>23</sup>
                    School of Earth and Space Exploration, Arizona State University, PO Box 876004, Tempe, AZ 85287-6004, USA; pkamiene@asu.edu
                               Department of Astronomy/Steward Observatory, University of Arizona, 933 N Cherry Ave., Tucson, AZ 85721-0009, USA
                                         <sup>3</sup> European Southern Observatory, Alonso de Córdova 3107, Vitacura, Casilla 19001, Santiago de Chile, Chile
         <sup>4</sup> Universidad Diego Portales Núcleo de Astronomía, Facultad de Ingeniería y Ciencias, Universidad Diego Portales, Av. Ejército 441, Santiago, Chile
                                                              Department of Astronomy, University of Massachusetts, Amherst, MA 01003, USA
                                          <sup>6</sup> Department of Astronomy, University of California, 501 Campbell Hall #3411, Berkeley, CA 94720, USA
                                                             Space Telescope Science Institute, 3700 San Martin Dr., Baltimore, MD 21218, USA
                                                     <sup>8</sup> Department of Physics and Astronomy, University of Louisville, Louisville, KY 40292, USA
9 Instituto de Radioastronomía y Astrofísica, Universidad Nacional Autónoma de México, Antigua Carretera a Pátzcuaro # 8701, Ex-Hda. San José de la Huerta,
                                                                                              Morelia, Michoacán, C.P. 58089, Mexico
                                                   <sup>10</sup> Center for Astrophysics | Harvard & Smithsonian, 60 Garden St., Cambridge, MA 02138, USA
                           <sup>11</sup> Cornell Center for Astrophysics and Planetary Science, Cornell University, Space Sciences Building, Ithaca, NY 14853, USA
                                             Department of Physics and Astronomy, University of Alabama, Box 870324, Tuscaloosa, AL 35404, USA
13 Chinese Academy of Sciences South America Center for Astronomy, National Astronomical Observatories, CAS, Beijing, 100101, People's Republic of China
                  Association of Universities for Research in Astronomy (AURA) for the European Space Agency (ESA), STScI, Baltimore, MD 21218, USA
   15 Center for Astrophysical Sciences, Department of Physics and Astronomy, The Johns Hopkins University, 3400 N Charles St. Baltimore, MD 21218, USA
16 Jodrell Bank Centre for Astrophysics, Alan Turing Building, University of Manchester, Oxford Rd., Manchester M13 9PL, UK
<sup>17</sup> International Centre for Radio Astronomy Research (ICRAR) and the International Space Centre (ISC), The University of Western Australia, M468, 35 Stirling
                                                                                                  Hwy., Crawley, WA 6009, Australia
                                                   <sup>18</sup> ARC Centre of Excellence for All Sky Astrophysics in 3 Dimensions (ASTRO 3D), Australia
                                                                                            Smith College, Northampton, MA 01063, USA
      National Research Council of Canada, Herzberg Astronomy & Astrophysics Research Centre, 5071 West Saanich Rd., Victoria, BC V9E 2E7, Canada INAF-Osservatorio Astronomico di Trieste, Via Bazzoni 2, I-34124 Trieste, Italy
                                         <sup>22</sup> INAF-Istituto di Astrofisica Spaziale e Fisica cosmica (IASF) Milano, Via A. Corti 12, 20133 Milan, Italy
                                                         Department of Physics and Astronomy, University of Missouri, Columbia, MO 65211, USA
                                               Received 2024 April 10; revised 2024 June 12; accepted 2024 June 27; published 2024 September 12
```

Abstract

We present a new parametric lens model for the G165.7+67.0 galaxy cluster, which was discovered with Planck through its bright submillimeter flux, originating from a pair of extraordinary dusty star-forming galaxies (DSFGs) at $z \approx 2.2$. Using JWST and interferometric mm/radio observations, we characterize the intrinsic physical properties of the DSFGs, which are separated by only $\sim 1''$ (8 kpc) and a velocity difference $\Delta V \lesssim 600 \, \mathrm{km \, s^{-1}}$ in the source plane, and thus are likely undergoing a major merger. Boasting intrinsic star formation rates $SFR_{IR} = 320 \pm 70$ and $400 \pm 80 \, M_{\odot} \, \text{yr}^{-1}$, stellar masses of $\log[M_{\star}/M_{\odot}] = 10.2 \pm 0.1$ and 10.3 ± 0.1 , and dust attenuations of $A_V = 1.5 \pm 0.3$ and 1.2 ± 0.3 , they are remarkably similar objects. We perform spatially resolved pixel-by-pixel spectral energy distribution (SED) fitting using rest-frame near-UV to near-IR imaging from JWST/ NIRCam for both galaxies, resolving some stellar structures down to 100 pc scales. Based on their resolved specific star formation rates (SFRs) and UVJ colors, both DSFGs are experiencing significant galaxy-scale star formation events. If they are indeed interacting gravitationally, this strong starburst could be the hallmark of gas that has been disrupted by an initial close passage. In contrast, the host galaxy of SN H0pe has a much lower SFR than the DSFGs, and we present evidence for the onset of inside-out quenching and large column densities of dust even in regions of low specific SFR. Based on the intrinsic SFRs of the DSFGs inferred from UV through far-infrared SED modeling, this pair of objects alone is predicted to yield an observable 1.1 ± 0.2 core-collapse supernovae per year, making this cluster field ripe for continued monitoring.

Unified Astronomy Thesaurus concepts: Strong gravitational lensing (1643); Starburst galaxies (1570); James Webb Space Telescope (2291)

Original content from this work may be used under the terms of the Creative Commons Attribution 4.0 licence. Any further distribution of this work must maintain attribution to the author(s) and the title of the work, journal citation and DOI.

1. Introduction

Out to at least $z \sim 3$, the fraction of obscured star formation in galaxies appears to increase nearly monotonically with increasing stellar mass (Bourne et al. 2017; Whitaker et al. 2017; McLure et al. 2018), a relation that has also been recovered by simulations at $z \lesssim 2$ (e.g., Zimmerman et al. 2024). Recent results from the Atacama Large Millimeter/submillimeter Array (ALMA) have even suggested the presence of a population of galaxies that are both massive and dust-rich as early as $z \approx 7$ (Algera et al. 2024). The dust-obscured mode of star formation has been found to dominate the cosmic star formation rate density (SFRD) for 12 billion years, to at least $z \sim 4$ (e.g., Bouwens et al. 2020; Zavala et al. 2021). Long et al. (2023) predicted that, at the peak of the Universe's star formation history at $z \sim 2$ ("Cosmic Noon"), 25%–60% of the stellar mass density of the Universe may be contributed by dusty starforming galaxies²⁴ (DSFGs) and their quiescent descendants. Together, this implies that our understanding of the growth and evolution of stellar mass in the Universe from rest-frame UV/ optical studies alone would be horribly incomplete.

Conversely, our knowledge of the typical stellar masses and properties of older, extant stellar populations of DSFGs is still woefully lacking, due in large part to intense dust attenuation at crucial rest-frame UV/optical wavelengths. Now, the sensitivity and resolution of JWST in this regime is beginning to facilitate novel interpretations of this frequently perplexing population—often also referred to as submillimeter galaxies (SMGs; Blain et al. 2002), although these may more accurately be said to comprise a subset of DSFGs (Casey et al. 2014a). They are widely believed to be the progenitors of massive quiescent, early-type galaxies seen at lower redshifts (Lilly et al. 1999; Farrah et al. 2006; Toft et al. 2014), and given their association with galaxy overdensities and protoclusters (Geach et al. 2006; Chapman et al. 2009; Clements et al. 2014, 2016; Dannerbauer et al. 2014; Casey et al. 2015; Umehata et al. 2015; Casey 2016; Hung et al. 2016; Miller et al. 2018; Long et al. 2020; Caputi et al. 2021; Calvi et al. 2023), it is presumed that many will evolve into the ultramassive population of brightest cluster galaxies (BCGs).

DSFGs at Cosmic Noon are typically considered to be dominated by compact nuclear starburst events, occurring within a thick shroud of dust. These have been postulated to signal the inside-out growth of galactic bulges that will persist in the massive descendants (e.g., Gullberg et al. 2019; Nelson et al. 2019). This activity may be driven by major mergers (Hopkins et al. 2008), or more secularly through in situ star formation in gravitationally unstable, gas-rich disks, followed by inward clump migration (e.g., Bournaud et al. 2007, 2008; Elmegreen et al. 2008; Ceverino et al. 2010; Elmegreen 2011; Wuyts et al. 2012). However, for DSFGs, this picture often lacks the context of how the extant stellar mass (or even ongoing unobscured star formation) is distributed. Many studies have found a factor of >2 larger effective radii in the rest-frame UV/optical versus far-infrared (FIR) continuum for DSFGs (including Ikarashi et al. 2015; Simpson et al. 2015; Barro et al. 2016; Hodge et al. 2016; Pantoni et al. 2021). However, these half-light sizes are subject to gradients in the mass-to-light (M/L) ratios, which may be the result of spatial variation in dust attenuation (e.g., Byun et al. 1994; Jansen et al. 1994; Tuffs et al. 2004; Möllenhoff et al. 2006; Pastrav et al. 2013; Popping et al. 2022), stellar population ages (e.g.,

Carrasco et al. 2010; van Dokkum et al. 2010; Tacchella et al. 2015), and metallicities (Franx & Illingworth 1990; Mollá et al. 1997; Carrera et al. 2008; Cresci et al. 2010; Kewley et al. 2010; Pilkington et al. 2012)—or realistically, some combination of all three (e.g., Keel & White 2001; Miller et al. 2022).

In the era of JWST, great progress is being made in directly capturing the rest-frame near-IR structure of galaxies at Cosmic Noon and earlier, offering a significantly less biased view of the actual distribution of stellar mass (Lang et al. 2019; Chen et al. 2022; Cheng et al. 2022; Suess et al. 2022; Abdurro'uf et al. 2023; Cheng et al. 2023; Colina et al. 2023; Kamieneski et al. 2023; Kokorev et al. 2023; Le Bail et al. 2024; Liu et al. 2024; Rujopakarn et al. 2023; Smail et al. 2023; Amvrosiadis et al. 2024; Kalita et al. 2024; Sun et al. 2024), including their clumpiness, compactness, and lopsidedness. This pixel-by-pixel comparison of stellar mass and star formation provides a key snapshot of the structural history of a galaxy, especially when supplemented with mapping of the molecular gas kinematics and dust continuum at comparable resolutions with facilities like ALMA. For example, an examination of how the star-forming main sequence of galaxies translates on resolved scales at z > 1 has now been made feasible (e.g., Abdurro'uf & Akiyama 2018, hereafter A18), along with its connection to fundamental scaling relations between the surface density of gas mass versus star formation rate and between gas mass surface density versus stellar mass surface density. While a full systematic study has not yet been carried out, results for a small number of objects can offer preliminary insights.

In this work, we focus on two DSFGs and a massive red galaxy at Cosmic Noon that have been strongly lensed by a massive galaxy cluster at z = 0.35. PLCK G165.7+67.0 (hereafter G165) was first identified by Cañameras et al. (2015) and Harrington et al. (2016), 25 hereafter H16, as an exceptionally IR-bright source in Planck and Herschel surveys, but it was first examined in-depth by Cañameras et al. (2018), Frye et al. (2019), and Pascale et al. (2022). Multiwavelength follow-up imaging at higher resolution revealed that the substantial submillimeter flux is driven by a highly magnified DSFG (Table 1) at z = 2.236 (H16), lensed into a giant arc by a galaxy cluster that appears to be undergoing a merger of two primary mass components (Figure 1, and Pascale et al. 2022). Hereafter, we refer to this known DSFG, PLCK G165.6295 +67.0026, ²⁶ as G165-DSFG-1 (or just DSFG-1), given its appearance as Arcs 1a and 1bc, per the labeling introduced by Frye et al. (2019). JWST NIRSpec spectroscopy from Frye et al. (2024), hereafter F24, recently revealed that DSFG-1 is associated with components at z = 2.2355 and z = 2.2401 (their IDs NS_969/Arc 1a and NS_46, respectively), with redshifts determined through multiple emission lines. These objects both appear to be starbursting, and are separated by 420 km s⁻¹ in the rest frame. With this work, we identify another strongly lensed submillimeter source, which is believed to lie at the same redshift (Cañameras et al. 2018). Our current photometric redshift and lens-model-predicted geometric redshift are also consistent with $z \approx 2.23$, making it likely that the two are gravitationally interacting (see Figure 2). For this second object, G165.6354+67.0087, we use the nickname G165-

 $^{^{24}}$ There is no widely adopted strict definition for DSFGs, but they are generally considered to have large SFRs $\gtrsim \! 100\,M_\odot\,{\rm yr}^{-1}$ and significant quantities of dust capable of reprocessing a sizable fraction of the ultraviolet (UV) emission from young stars into the infrared. A subset of DSFGs, hyperluminous infrared galaxies (HyLIRGs) are more clearly defined, such that they exceed $L_{\rm IR} > 10^{13}\,L_\odot$.

The cluster has also been denoted in literature as PJ112714.5.

²⁶ Galactic coordinates are used to remain consistent with the name of the cluster, and the location of Arc 1a is chosen as it contains the entire object, in contrast with the fold image 1bc.

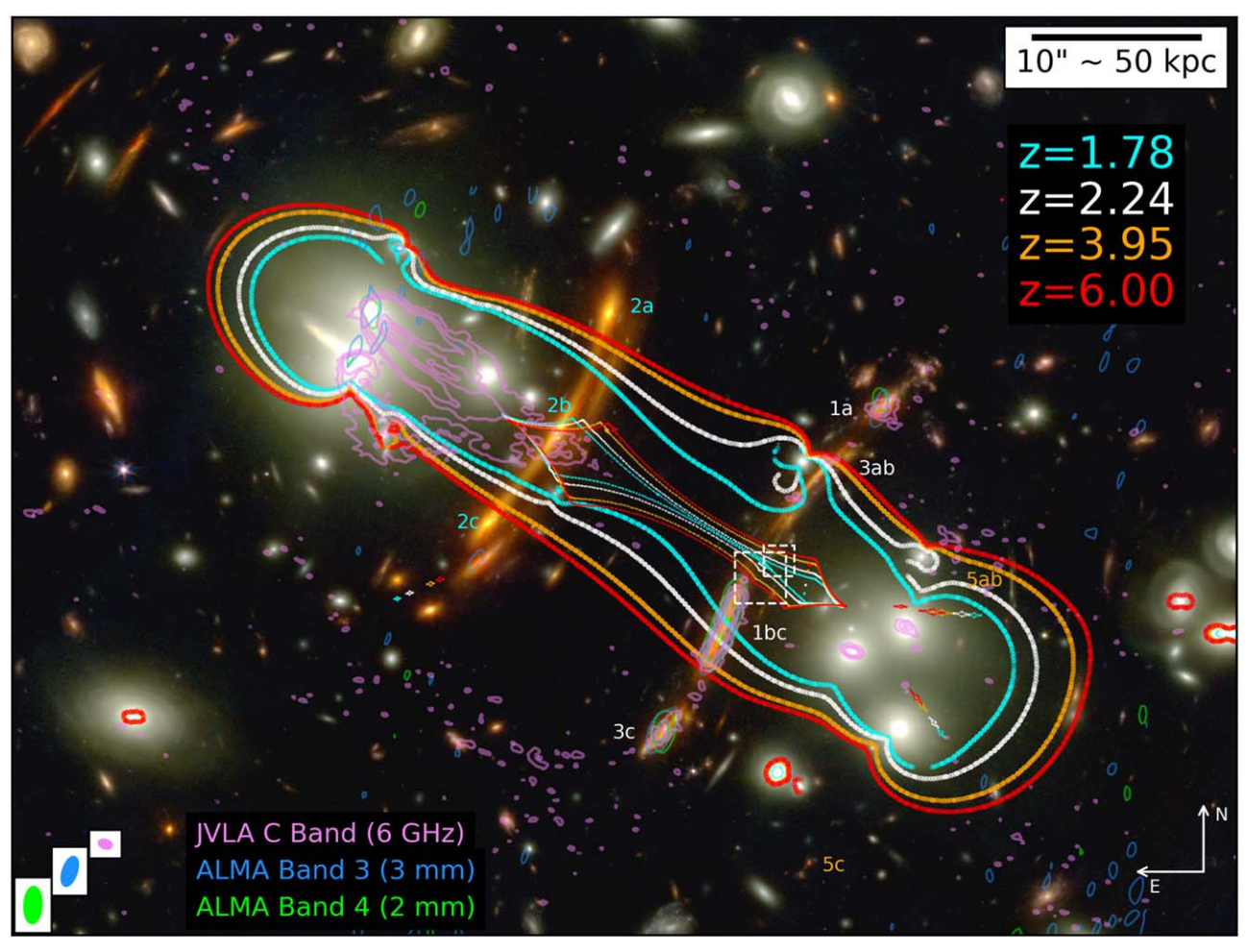


Figure 1. North-aligned RGB image of the G165 cluster, with (R, G, B) = (F444W + F356W, F277W + F200W, F150W + F090W). Colored curves show the best-fit model-derived lensing caustics at the source-plane redshifts of Arc system 2abc (the host of SN H0pe; z = 1.78), Arc 1abc (z = 2.24), Arc 5abc (z = 3.95), and at z = 6; see Figure 2 of F24 for the full set of arcs. Violet contours show JVLA 6 GHz continuum, blue contours show ALMA 3 mm continuum, and green contours show ALMA 2 mm continuum. Their respective synthesized beams are shown in the lower left. Spurious features in the ALMA contours toward the edge of the field of view are due to lower sensitivity near the edge of the primary beam. Arcs 1a, 1bc, and 3c are strongly detected at 2 mm, 3 mm, and 6 GHz. Arc 3ab yields only a marginal detection at 6 GHz, which is due to the lack of dust/radio continuum in the region of the galaxy that is lensed into this merging pair of arcs (see Figure 2, for example). Dashed white boxes show the source-plane locations of DSFG-1 and DSFG-3 (smaller northwest and larger southeast boxes, respectively), and they match the fields of view shown in Figure 3.

 Table 1

 Model-derived Magnifications and Observed mm/radio Fluxes

Arc	$\mu_{2~\mu\mathrm{m}}$, JWST	$\mu_{2 \; \mathrm{mm}}$	$\mu_{3 \mathrm{mm}}$	$\mu_{ m 6~GHz}$	$S_{2 \text{ mm}} \ (\mu \text{Jy})$	S _{3 mm} (μJy)	S _{6 GHz} (μ J y)
Arc 1a Arc 1bc Arc 1abc	5.5 ± 0.1 42 ± 1 	7.6 ± 0.2 44 ± 3 28.4 ± 2.4	8.1 ± 0.2 41 ± 4 29.1 ± 1.7	$6.6 \pm 0.2 \\ 46 \pm 5 \\ 24^{+6}_{-3}$	260 ± 30 1620 ± 90 1900 ± 100^{a}	$ 110 \pm 30 \\ 860 \pm 60 \\ 980 \pm 60^{a} $	$ 190 \pm 10 \\ 960 \pm 50 \\ 1150 \pm 50 $
Arc 3ab Arc 3 c Arc 3abc	40 ± 2 5.9 ± 0.1 	6.8 ± 0.2 7.3 ± 0.7	7.5 ± 0.3 7.4 ± 0.6	29 ± 5 5.9 ± 0.2 $6.8^{+1.1}_{-0.4}$	<80 620 ± 40 620 ± 40^{a}	<90 310 ± 30 310 ± 30^{a}	39 ± 5 132 ± 8 171 ± 9

Notes. Magnifications are measured for the F200W filter (as representative for all of the NIRCam filters) by taking the source-plane flux-weighed average over the magnification map. For the mm and radio images, magnifications are measured by simply taking the ratio of image-plane to source-plane areas.

DSFG-3 (or DSFG-3), in accordance with its appearance in Arcs 3c and 3ab. Through its inferred properties (including $L_{\rm IR} > 10^{12.6}$), it is safely classified as a DSFG.

As first reported by Frye et al. (2023) and Polletta et al. (2023), initial inspection of the NIRCam observations immediately revealed a conspicuous multiply imaged

^a The combined flux of Arcs 1abc and 3abc at 2 mm ($S \approx 2.5$ mJy) is consistent with that expected from a modified blackbody (dust emissivity index $\beta = 1.8$) with $S_{1mm} = 24 \pm 2.0$ mJy (H16), which is $S_{2mm} \approx 2.5$ mJy. The observed flux at 3 mm (1.3 mJy) exceeds the modified blackbody prediction (0.5 mJy), possibly owing to contamination from synchrotron emission.

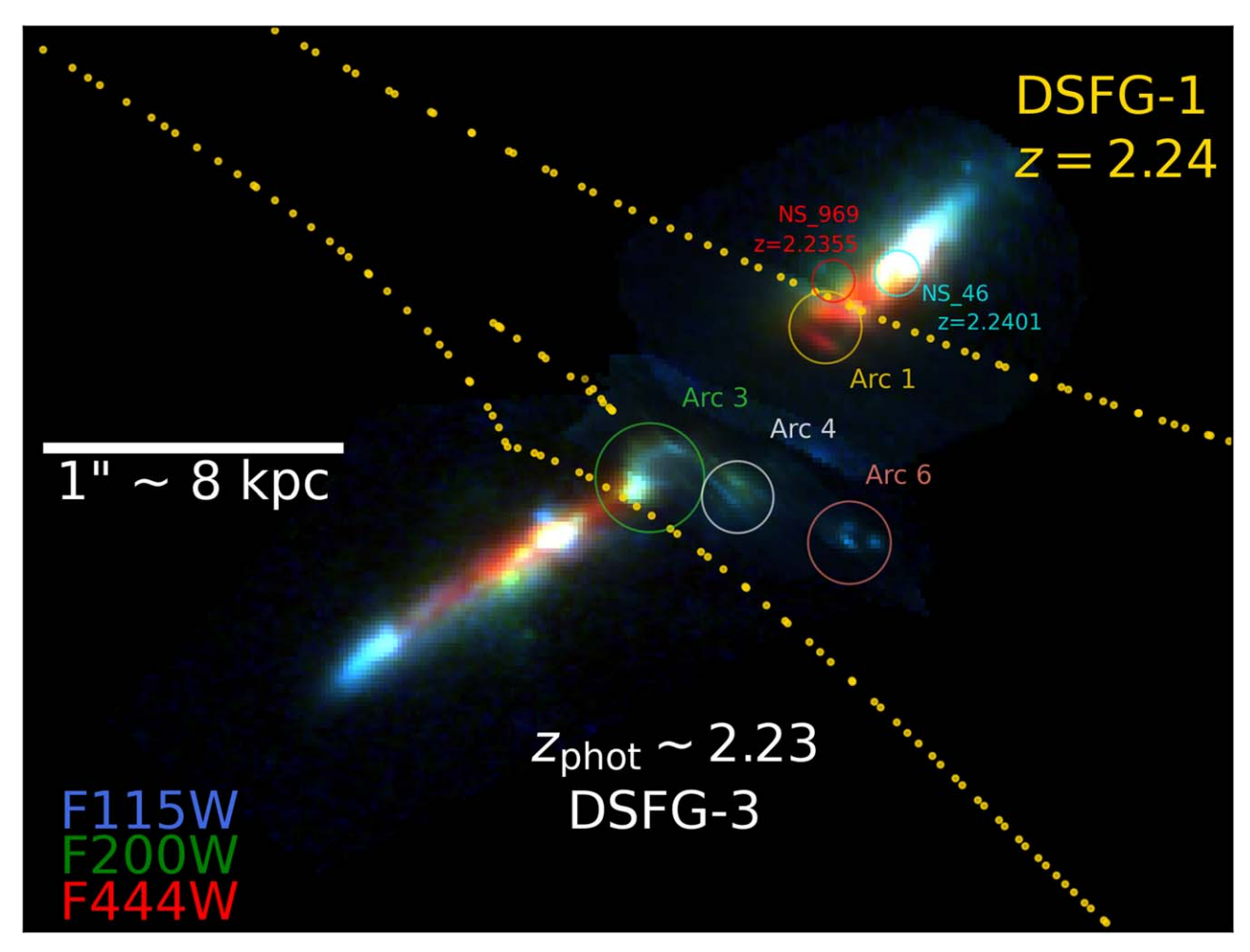


Figure 2. Source-plane reconstruction of the DSFG system at z=2.24. The background RGB image shows JWST filters F444W, F200W, and F115W (respectively). The gold dotted line shows the lens-model-derived caustic curve at z=2.24 The portions of the source plane interior to the caustics are triply imaged; structures above and below the caustics in this figure are only singly imaged (but still magnified by $\mu \gtrsim 5$, primarily in the direction perpendicular to the caustic). The constituent arcs (Arcs 1, 3, 4, and 6), as labeled by Frye et al. (2024), are indicated with circles, in addition to the NS_969 and NS_46 components that are associated with DSFG-1 (but at slightly different redshifts, indicating perhaps the presence of two orbiting clumps seen in projection).

supernova in a set of arcs on the opposite side of the cluster from the DSFGs. Named SN H0pe, this serendipitous discovery was quickly followed-up with additional NIRCam imaging and NIRSpec spectroscopy to track the transient's light curve and classify its type. At z=1.78, it was confirmed to be one of the most distant known Type Ia supernovae. This discovery may not be purely coincidence: the fortuitous alignment of a rich collection of star-forming $z\sim2$ objects with a massive and highly elliptical foreground cluster $(M_{600~\rm kpc}=(2.6\pm0.3)\times10^{14}M_\odot; F24)$ along the line of sight provides ideal conditions for the detection of Type Ia and corecollapse supernovae. As the area of time-delay cosmography has become increasingly fruitful in recent years (Treu et al. 2022), the G165 cluster is likely to endure as a subject of intense interest and legacy value for years to come.

This paper is organized as follows: in Section 2, we outline the near-IR, radio, and mm-wave imaging used in this study. In Section 3, we discuss our approach to lens modeling and pixel-by-pixel spectral energy distribution (SED) fitting. The results of these analyses are outlined in Section 4, and their implications are discussed in Section 5 and summarized in Section 6.

In this work, we adopt a ΛCDM cosmological model of $\Omega_m = 0.3$, $\Omega_{\Lambda} = 0.7$, and $H_0 = 70 \, \text{km s}^{-1} \, \text{Mpc}^{-1}$, and a Kroupa (2001) initial mass function (IMF). At the redshift of the cluster (z = 0.348), the angular-to-physical size conversion is $1'' = 4.921 \, \text{kpc}$, and at the redshift of the DSFGs (z = 2.236), $1'' = 8.243 \, \text{kpc}$ (Wright 2006). To comment on our notation: throughout, we frequently use DSFG-1 and DSFG-3 as shorthand for PLCK_G165.6295+67.0026 and G165.6354+67.0087, respectively. These names themselves are introduced to avoid confusion when referring to the actual objects in the background of the cluster. To clarify, DSFG-1 is visible in its entirety in Arc 1a, while only a fraction of the intrinsic source is visible in the merging pair Arc 1bc. Likewise, DSFG-3 is visible entirely in Arc 3c, with a small portion of the source visible in the merging pair Arc 3ab.

2. Data

2.1. JWST NIRCam

A more in-depth description of the JWST NIRCam data is given in Windhorst et al. (2023) and Frye et al. (2024), but we provide relevant details here. G165 was observed with NIRCam in three epochs: first through the Prime Extragalactic

Table 2
Properties of DSFG-1 and DSFG-3 from Total IR Dust SED, and Corresponding SN Rates

Object	$\mu_{2 \text{ mm}} \text{SFR}_{\text{IR}}^{\text{ a}} (M_{\odot} \text{ yr}^{-1})$	$SFR_{IR} (M_{\odot} \text{ yr}^{-1})$	$\log[L_{ m IR}/L_{\odot}]$	$R_{\text{CC}}^{}^{}}}$ (yr^{-1})	$R_{\rm CC}(1+z)^{-1}$ (yr ⁻¹)	$R_{e,2\mathrm{mm}}$ (arcsec)	$R_{e,2\mathrm{mm}} \ \mathrm{(kpc)}$
G165-DSFG-1	9100 ± 1900	320 ± 70	12.5 ± 0.1	3.3 ± 0.7	1.0 ± 0.2	0.20 ± 0.02	1.6 ± 0.2
G165-DSFG-3	2900 ± 500	400 ± 80	12.6 ± 0.1	4.2 ± 0.8	1.3 ± 0.2	0.25 ± 0.03	2.1 ± 0.2

Notes. We derive the SFR of the two DSFGs independently using the far-IR photometry (H16) versus the rest-frame UV-NIR photometry from NIRCam (which is shown in Table 3). As the far-IR photometry largely does not resolve Arcs 1abc and 3abc, we make a preliminary estimate by apportioning the total SFR_{IR} according to their share of flux at 2 mm and 3 mm (combining Arcs 1a and 1bc, and Arcs 3ab and 3c), as both arc systems are understood to be at similar enough redshifts. Then, these apportioned SFRs are corrected for the total 2 mm magnifications of Arc 1abc and Arc 3abc, respectively. Based on these various SFRs, we estimate the rate of occurrence of core-collapse supernovae (for the rest frame of each galaxy); the observable rate is likely bracketed by the SED- versus IR-inferred SFRs, given that SNe in some very dusty environments may be missed (or, alternatively, the extreme star formation may lead to a porosity in the dust geometry that lends to a more favorable chance for discovery).

Areas for Reionization and Lensing Science (PEARLS) program (PID 1176; PI: Windhorst) on 2023 March 30 (Epoch 1), followed by two later epochs on 2023 April 22 (Epoch 2) and 2023 May 9 (Epoch 3) through a DDT program (PID 4446, PI: Frye); these programs were designed to track the light curve of SN H0pe following its discovery in Epoch 1. As the exposure times of Epoch 1 were longer (see Table 1 of F24), and eight filters were used instead of six, for simplicity we performed most of our analysis in this work on data from Epoch 1 only, in part to minimize variance in the point-spread function (PSF) that could impact the spatially resolved SED analysis. Moreover, the primary targets here are detected with very high significance, and do not benefit enormously from stacking additional exposures. However, the image families used in constraining the lens model (which are often faint) benefit greatly from this additional effective exposure time, and so the stacked images are employed for that purpose. Limiting magnitudes are $m_{\rm AB} \sim 28.4 - 28.5$ for the four short-wavelength (SW) filters (F090W/F115W/F150W/F200W) and $m_{\rm AB} \sim$ 28.6–28.9 for the four long-wavelength (LW) filters (F277W/ F356W/F410M/F444W); see Figure 6 of F24. Data were reduced in line with Windhorst et al. (2023), using the STScI JWST Pipeline²⁷ version 1.11.2 (Bushouse et al. 2023) and context file pmap_1100, but with additional improvements in "wisp" removal as described by Robotham et al. (2023). Images in this work were drizzled onto 30 mas square pixels.

2.2. ALMA Bands 3 and 4

G165 was observed with ALMA band 3 (representative wavelength 2.7 mm, 111 GHz, hereafter referred to as 3 mm) and band 4 (2.2 mm, 138 GHz, hereafter referred to as 2 mm) as part of program 2021.1.00607.S (PI: R. Cañameras). These data were retrieved from the public ALMA archive. ²⁸

Continuum multifrequency synthesis images and spectral cubes were created using the Common Astronomy Software Applications (CASA) version 6.2.1 (McMullin et al. 2007), with robust=0.5 Briggs weighting (Briggs 1995). The unweighted baselines ranged from 0.03 to 0.3 km (5th-80th

percentile). This results in synthesized beams of $2.0^{\circ} \times 0.0^{\circ}$ at PA = -2.0° 7 for 3 mm (maximum recoverable scale of 18.0° 4) and $1.0^{\circ} \times 0.0^{\circ}$ 7 at PA = -18.0° 4 for 2 mm (maximum recoverable scale of 15.0° 1). The continuum noise rms levels achieved are 22 μ Jy beam⁻¹ (3 mm) and 20 μ Jy beam⁻¹ (2 mm), both over a 3.3 GHz bandwidth. Weather conditions were favorable, with mean precipitable water vapor PWV = 0.9 mm for the 3 mm observations (executed on 2022 May 26) and PWV = 1.4 mm for the 2mm observations (executed on 2022 May 28).

As the lensed objects of interest are spatially resolved, photometry was performed using the flood-filling algorithm BLOBCAT (Hales et al. 2012). In Table 1, we compare the measured 2 mm and 3 mm fluxes against the 1 mm flux from the Large Millimeter Telescope (LMT) AzTEC, reported by H16, under assumption of a modified blackbody SED, and find relative consistency.

2.3. VLA C Band

G165 was observed with the Karl G. Jansky Very Large Array in C band (4–8 GHz) in full polarization during the most extended A configuration through our program 18A-399 (PI: P. Kamieneski), which targeted 26 members of the Planck All-Sky Survey to Analyze Gravitationally-lensed Extreme Starbursts (PASSAGES) sample; see Kamieneski et al. (2024) for additional details. The target was observed on 2018 April 6 during a shared track (switching with another nearby object) lasting a total of 3.0 hr, with an effective total on-source integration time of 1.1 hr. Weather conditions were favorable during the observations: the phase rms measured by the Atmospheric Phase Interferometer at the Very Large Array (VLA) site was $\approx 2^{\circ}$. Antenna baselines ranged from 0.8 to 36.6 km, yielding a maximum recoverable scale of 9". The sensitivity reached was 2.7 μ Jy beam $^{-1}$. Natural weighting achieved a synthesized beam of 0."65 \times 0."37 at PA = 72.°2.

The data were reduced using CASA v6.1.0. Initial flagging and calibration were carried out through the VLA Calibration pipeline v2018.1. The Högbom (1974) CLEAN algorithm was

^a The total apparent (i.e., lensing-uncorrected) IR-derived SFR of $12000 \pm 2000 \, M_{\odot} \text{yr}^{-1}$ from H16 is divided between Arcs 1abc and 3abc according to their ratio of millimeter flux, $S_{1abc}/S_{3abc} = 3.1 \pm 0.3$ (averaged for 2 mm and 3 mm).

^b Expected rate of core-collapse supernovae tabulated as $R_{CC} = k_{CC} \cdot \text{SFR}$; $k_{CC} = 0.0104 \, M_{\odot}^{-1}$ (e.g., Strolger et al. 2015). These are intrinsic SN rates; observed SN rates will be dilated by a factor of $(1+z)^{-1}$, but also increased for any SNe occurring in regions of the galaxy that are multiply imaged.

²⁷ https://github.com/spacetelescope/jwst

https://almascience.nrao.edu/aq/

 $[\]overline{^{29}}$ Imaging with robust =-1 (i.e., closer to uniform weighting) was tested in an attempt to improve angular resolution, but the S/N was insufficient to yield useful results.

used to deconvolve the image down to a 2σ threshold. As with the ALMA images, photometry was performed using BLOBCAT (Hales et al. 2012), also reported in Table 2. As discussed by Pascale et al. (2022), these data also reveal a number of point sources and narrow angle tails (e.g., Rudnick & Owen 1977; Venkatesan et al. 1994), which offer some insight into the intracluster medium and dynamical state of the galaxy cluster.

3. Methodology

3.1. Lens Modeling

We constructed a parametric lens model for the G165 cluster using LENSTOOL³⁰ (Kneib et al. 1993, 1996; Jullo et al. 2007; Jullo & Kneib 2009), which has been tested extensively for galaxy clusters (e.g., Johnson et al. 2014; Meneghetti et al. 2017). The model is constrained by 41 families of multiply imaged features—of which 14 have spectroscopic redshift information (Frye et al. 2019; Pascale et al. 2022; Frye et al. 2024), covering four distinct source planes. Some details of this model and the cluster members are presented in the appendix of Pascale et al. (2024), but we include additional information here. For this iteration of the model, we considered only the image-plane positions, which are reported in F24. To estimate the astrometric uncertainty in these positions, multiple team members independently marked the positions for the known image family members; they found a median offset of 0."03, which is consistent with the pixel scale used for identifying images. For the mass profiles, we used two cluster-halo-scale profiles for the merging cluster components, in addition to perturbations to this large-scale potential in the form of the 165 identified cluster member galaxies at $z \approx 0.35$. Each of these profiles was chosen to be a pseudo-isothermal elliptical mass distribution (PIEMD; Kassiola & Kovner 1993).

To reduce the number of free parameters, the position of each cluster member was held fixed to the centroids of their luminous components. Likewise, the ellipticities and orientations were held fixed to match their morphologies in the F200W filter. The masses of the cluster members were scaled all together in a power law, according to their F200W flux, per Limousin et al. (2005). The power law was normalized such that a characteristic L_{\star} galaxy at the redshift of the cluster $(m_{\rm F200W}=17.0~{\rm AB~mag})$ has a velocity dispersion of $\sigma_0^{\star}=120~{\rm km~s^{-1}}$, a core radius of $r_{\rm core}^{\star}=0.15~{\rm kpc}$, and a cut radius of $r_{\rm cut}^{\star}=30~{\rm kpc}$. All galaxies were scaled in mass based on their flux relative to L_{\star} . We settled on these choices after some trial and error, as it was determined that the current set of lensing evidence does not sufficiently constrain the masses of perturbing cluster galaxies, so they were instead held fixed. The choices of σ_0^{\star} , r_{core}^{\star} , and r_{cut}^{\star} match those used in several other works that use LENSTOOL, including Limousin et al. (2008) and Johnson et al. (2014). However, one foreground galaxy near Arc 3ab, located at $(\alpha, \delta) = (11^{\text{h}}27^{\text{m}}14.304, +42^{\text{d}}$ 28^m32^s32), was optimized independently from the other cluster members, given the large effect it has on the arc. Its velocity dispersion σ was kept as a free parameter, assuming a uniform prior of 0-250 km s⁻¹.

As for the two cluster-scale halos, their free parameters include centroid position, ellipticity, orientation, velocity dispersion, and core radius. As their cut/truncation radii are poorly constrained, these were fixed to values of 1000 kpc.

30 https://projets.lam.fr/projects/lenstool/wiki

Uniform priors were used for these parameters, including a wide range of $\pm 5''$ in x and y position from the approximate center of both cluster cores, a very wide range in ellipticity from 0 to 0.85, a maximum velocity dispersion of 800 km s⁻ and a maximum core radius of $20'' \approx 100$ kpc. We also left as free parameters the redshifts for 16 background lensed image families for which no spectroscopic information is currently available. However, to simplify the parameter space, we placed relatively tight priors on these, based on their photometric redshifts. This was done iteratively, where we widened or adjusted the redshift range if prior iterations of the model optimization resulted in any parameters clearly being overly limited by the prior boundaries. Still, the uncertainties in these "geometric" redshifts (often as small as $\Delta z = \pm 0.01$) are likely drastic underestimates. We present the full set of best-fit parameter values, and the corresponding convergence map, in Appendix A. In this work, we adopt the median of each parameter's posterior distribution, which is only appropriate if the posteriors are well-behaved and approximately normally distributed (and especially only if the distributions are not multimodal). We also provide the minimum- χ^2 solutions, which are nearly always in close agreement with the median solution.

To determine magnifications, we used slightly different approaches for JWST versus mm/radio images. For the ALMA and VLA images, which are not contaminated by nearby foreground sources, 31 we measured magnifications simply by taking the ratio of image-plane to source-plane area. For the JWST images, we measured representative magnifications using the F200W filter, and compute an average of the magnification map weighted by source-plane flux. In both cases, to include the relevant statistical uncertainties, we resampled 300 iterations uniformly from the MCMC-derived posterior distribution, resulting in an approximately Gaussian distribution of magnifications. The results for the Arc 1abc and Arc 3abc systems are summarized in Table 1. Any slight discrepancies beyond statistical uncertainty between the magnifications for rest-frame near-IR, far-IR, and radio continuum are likely due in part to very different observing parameters (e.g., PSFs), but also due to differences in sourceplane distribution (as seen in Figure 3).

3.1.1. Redshift of DSFG-3

Since DSFG-3 lacks a secure multiline spectroscopic redshift, we left this as a free parameter in our lens model and allowed the redshift to vary from z = 2.0 to 2.2 in the final model. This range was chosen based on previous iterations of the model with wider redshift priors. This is also in line with the photometric redshift of $z_{\rm phot} = 2.23 \pm 0.09$ and with previous iterations of the lens model using a wider prior range, which suggested a geometric redshift of $z_{\text{geom}} \approx 2.1$. The MCMC posterior distribution yields a quite precise value of $z_{\rm geom} = 2.11 \pm 0.01$ (although the uncertainty is likely underestimated). This narrow range is probably a result of the constraint offered by DSFG-1, which is lensed by a similar portion of the foreground cluster and has a known redshift from the LMT Redshift Search Receiver (RSR) and other single-dish submm observations (H16; Harrington et al. 2021) and from NIRSpec (F24).

³¹ While several of the cluster members are detected in 6 GHz continuum, they are sufficiently far from the lensed arcs of interest to have negligible impact.

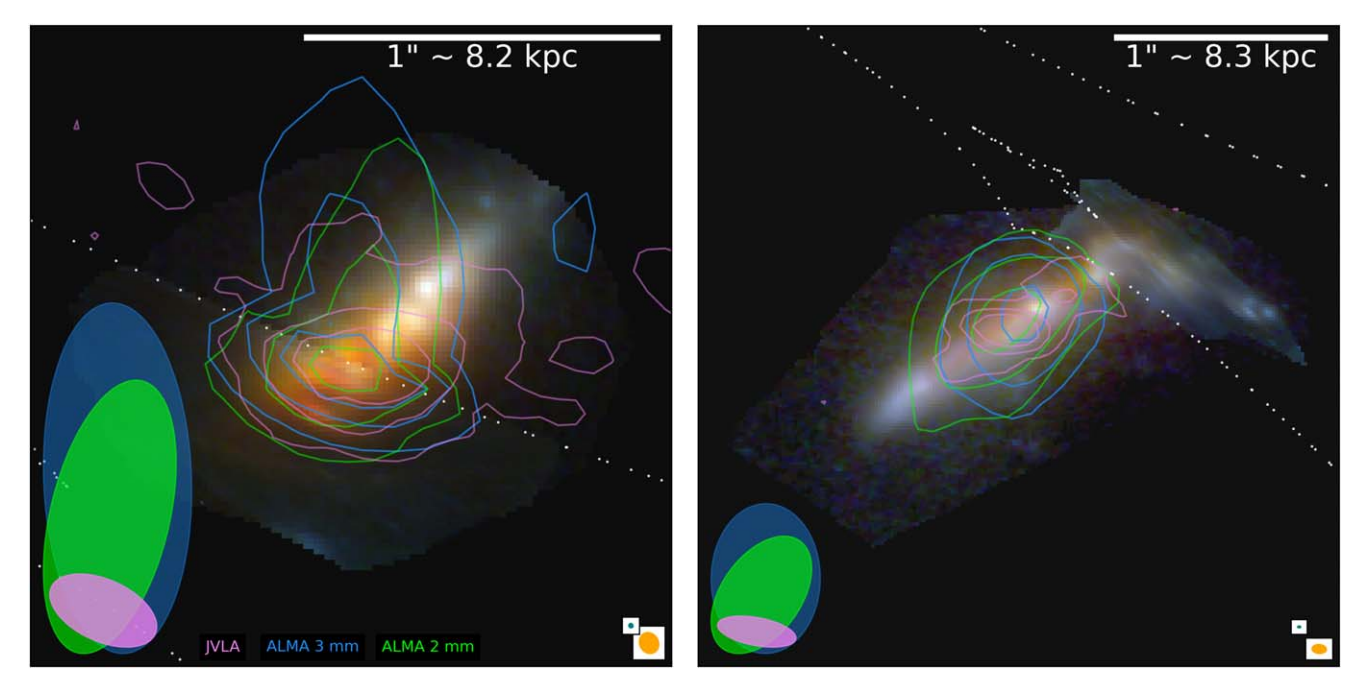


Figure 3. Source-plane reconstruction of Arcs 1abc at z=2.236 (left) and 3abc at the lens-model-preferred redshift of z=2.12 (right), with eight-filter RGB images scaled according to the Trilogy prescription. The locations of these reconstructions are indicated in Figure 1. The filters are assigned to the red/green/blue channels as (R,G,B) = (F356W + F410M + F444W, F200W + F277W, F090W + F115W + F150W). Caustics for their respective redshifts are shown as white dotted curves, while contours show the reconstruction of JVLA 6 GHz (violet), ALMA 3 mm (light blue), and ALMA 2 mm (lime green), as in Figure 1. Representative source-plane elliptical PSF beams (Section 3.1.2) for the radio/mm images are shown in the lower left, and for the finest/coarsest NIRCam filters in the lower right (teal = F090W, orange = F444W). Only the regions of the source inside the caustic curves (the southeastern end of G165-DSFG1 and the northwestern end of G165-DSFG3) are included in their respective highly magnified fold images, 1bc and 3ab (Figure 17). However, by reconstructing together with the much lower-magnification images 1a and 3c, they are effectively convolved to lower resolution.

There is no clear evidence of a second line detected in the LMT/RSR spectrum (H16), but the small velocity separation from DSFG-1 in the CO(4-3) profile (Cañameras et al. 2018) suggests that the CO(3-2) line for DSFG-3 would also be blended with that of DSFG-1 at z = 2.236. Indeed, this target has the widest linewidth $(\Delta V = 650 \pm 10 \,\mathrm{km \, s^{-1}})$ of the sample presented by H16, and a possible secondary component at $\sim -400 \text{ km s}^{-1}$, giving further weight to the hypothesis that the lines are blended. Since DSFG-3 is inferred to have a similar stellar mass, size, and star formation rate as DSFG-1 (as we discuss in Section 4), it is reasonable to expect comparable CO flux (or only ~4 times greater flux for DSFG-1, given its larger magnification; see Table 1). A nondetection by virtue of a faint line flux is thus unlikely. However, the pointing center of the LMT observations coincides with the peak of the submm flux, which is dominated by the high-magnification Arc 1bc. At an angular separation of <11", Arc 3c would be near the edge of the primary beam (~13."1 at 106.86 GHz), so it is also somewhat possible that any lines were simply missed by the observations.

We adopt the redshift of DSFG-3 to be z=2.23 in this work ($\Delta V \sim 600~{\rm km~s}^{-1}$ from DSFG-1), but we do not hold this redshift fixed in our lens model, given some lingering uncertainty. For the source-plane reconstructions shown in Figures 2 and 3, we ray trace back to the lens model preferred redshift z=2.12 for the highest-fidelity view of the source, but this has no impact on our interpretation of results.

3.1.2. Source-plane Reconstruction

The reconstruction of all images in this work in the source plane does not impose regularization or parameterization of the intrinsic structure of the source. Instead, the observed images

are ray-traced to the source plane pixel-by-pixel through the cleanlens function of LENSTOOL, with the image plane oversampled by a factor of 4 and the source plane by a factor of 2. Further details of our specific procedure can be found in Section 3.3 of Kamieneski et al. (2024). Figure 3 reconstructs the full structure of G165-DSFG-1 and G165-DSFG-3 by including both low- (1a and 3c) and high-magnification (1bc and 3ab) arcs. Effectively, this simple approach convolves the high-magnification arcs with the PSF of the low-magnification counterparts (e.g., Sharma et al. 2018). We use this version to estimate the source-plane size of the dust continuum, where we use the CASA IMFIT task to fit the emission with 2D Gaussian profiles (and adopt a minimum 10% fractional uncertainty). Despite the smaller beam size of the 3 mm observations, these dust sizes are also measured for the 2 mm images, owing to their higher S/N, as reported in Table 2. Additionally, the possible contamination from synchrotron radiation at 3 mm is expected to result in slightly larger sizes than from thermal dust alone. In Appendix C, we show the reconstructions from including only the high-magnification images, which are at essentially the finest achievable resolution. There is general agreement with the structure seen in Figure 3, adding confidence to this reconstruction.

Red, green, and blue (RGB) images of the eight NIRCam filters are constructed according to the Trilogy³² prescription (Coe et al. 2012). In all cases, we also show representative source-plane PSFs to illustrate the approximate resolution of the reconstructions. These are created by placing a simulated PSF or beam at a location in the image plane and ray-tracing it to the source plane in the same manner as the image itself (then

³² https://www.stsci.edu/~dcoe/trilogy

refitting with a two-dimensional Gaussian). The distorted source-plane PSFs arise because the image-plane PSFs are relatively circularly symmetric to first order, but this symmetry is lost through the ray-tracing process. However, as there is a gradient in magnification over each of the arcs (which is much more extreme for 1bc and 3ab), the source-plane PSF is finer in regions closer to the caustic curve than those further away. While the source-plane reconstructions assist in our interpretation of these objects, most of this work computes properties in the image plane and applies a magnification correction (or relies on magnification-invariant properties). This approach is less subject to any pitfalls of the intricacies of source-plane PSFs.

The approximate source-plane major axes of the ALMA 3 mm and 2 mm beams (roughly oriented along the major axis of the galaxies) are $1\rlap.{''}0\approx 8.2$ kpc and $0\rlap.{''}8\approx 6.6$ kpc for G165-DSFG-1, and $0\rlap.{''}7\approx 5.8$ kpc and $0\rlap.{''}6\approx 5.0$ kpc for G165-DSFG-3. For VLA 6 GHz, the source-plane beam minor axes are approximately oriented along the galaxies' major axes, which are $0\rlap.{''}2\approx 1.6$ kpc for G165-DSFG-1, and $0\rlap.{''}1\approx 0.83$ kpc for G165-DSFG-3. These are indicated in Figure 3.

3.2. Pixel-by-pixel SED Fitting with PIXEDFIT and BAGPIPES

As the cluster lensing provides an areal magnification and a flux amplification for the DSFGs, it becomes easier to ascertain the spatially resolved properties of their stellar populations through so-called pixel-by-pixel SED fitting. To accomplish this, we used the publicly available package PIXEDFIT³³ (Abdurro'uf et al. 2021; also Abdurro'uf et al. 2022a, 2022b, 2023) to bin pixels such that each satisfies an S/N condition in all filters, while preserving similarity in SED shape between pixels within each bin. In brief, all images are first convolved to the PSF of the lowest-resolution filter, F444W. Starting with the brightest unbinned pixel, each bin is required to be larger than the F444W PSF FWHM (0."14). If an S/N threshold for each filter is met (a conservative S/N = 20, in our case), the bin is established; otherwise, the radius of the bin is increased. Before adding the new pixels from the larger radius to the bin, their SED shape is confirmed to be consistent through a χ^2 calculation. This process then repeats, starting with the brightest pixel not already in a bin, and terminates once no additional bins can be constructed. Full details are provided in Section 3.3 of Abdurro'uf et al. (2021).

With the bin-wise photometry collected for the eight NIRCam bands $(0.9 - 4.4 \mu m)$, we fitted the SED of each bin with BAGPIPES (Bayesian Analysis of Galaxies for Physical Inference and Parameter Estimation; Carnall et al. 2018). The star formation history (SFH) was parameterized as an exponentially declining or "tau" model, where star formation promptly begins at time T_0 and decays relative to a timescale τ . The stellar population age for each bin could vary from 0.1 Gyr to the age of the Universe at the given redshift, and τ was allowed to vary from 0.3 to 10 Gyr. We opt for this simple (i.e., not bursty or nonparametric) treatment of the SFH given the small physical scale of each bin, especially as photometric uncertainties become more substantial compared to the galaxyintegrated measurements and overfitting becomes a concern. In using a wide prior in stellar population ages, modeling the SED of many (sub)kpc-scale regions independently can effectively reproduce a stochastic galaxy-wide SFH by deriving an ensemble of formation times. In other words, greater flexibility in spatial variation with a simple SFH will likewise yield a similar flexibility in temporal variation. This approach of a unimodal SFH is consistent with some other recent works employing spatially resolved SED modeling (e.g., Jafariyazani et al. 2019; Nagy et al. 2022; Giménez-Arteaga et al. 2023, 2024; Jain et al. 2024).

The total mass formed was allowed to vary widely, from $\log_{10}(M/M_{\odot})=1-15$, and metallicity could vary from 0 to 3.5 Z_{\odot} . The standard nebular component in the BAGPIPES fits was accounted for through the ionization parameter, $\log(\mathcal{U})$, which was allowed to vary from -4 to -2, precomputed from CLOUDY photoionization models (Ferland et al. 2017). While higher values (up to -1) can be found for individually resolved H II regions (e.g., Snijders et al. 2007), an upper limit of -2 is typically sufficient for starbursts resolved on kpc scales (e.g., for M82's inner 500 pc; Thornley et al. 2000; Förster Schreiber et al. 2001). A Calzetti et al. (2000) dust attenuation model was imposed, with attenuation allowed to vary from $A_V = 0$ -3, which we found to be a sufficient range. 34

4. Results

4.1. The Complex, Galaxy-wide Assembly of Stellar Mass in Two DSFGs at Cosmic Noon

One of the fundamental questions we have sought to address through our resolved pixel-by-pixel SED modeling of G165-DSFG-1 and G165-DSFG-3 is how their significant ongoing star formation is spatially distributed. If DSFGs are primarily powered by violent major mergers of massive galaxies, as for local ultraluminous infrared galaxies (ULIRGs; Armus et al. 1987; Soifer et al. 1987; Sanders et al. 1988; Sanders & Mirabel 1996; Lonsdale et al. 2006), is it reasonable to expect that their burst of star formation might be confined only to nuclear regions, with shocks and tidal forces driving gas inward (e.g., Hernquist 1989; Stockton 1990; Barnes & Hernquist 1991, 1992)? Or if other modes of extreme star formation are prevalent, such as gravitational instabilities within massive gas-rich disks—fueled continuously by cold gas streams (e.g., Kereš et al. 2005; Dekel et al. 2009; Davé et al. 2010)—would we expect to find a greater number of global star formation events, reaching well beyond the nucleus?

Numerous recent works have demonstrated that the effective radii of DSFGs at rest-frame far-IR are compact (\sim 1–2 kpc) and smaller than at rest-frame UV/optical (e.g., Ikarashi et al. 2015; Simpson et al. 2015; Barro et al. 2016; Hodge et al. 2016; Tadaki et al. 2017). On the other hand, some of the most luminous DSFGs—so-called hyperluminous infrared galaxies (HyLIRGs), which exceed $L_{\rm IR} > 10^{13} \, L_{\odot}$ —may be more extended, in part explaining their ability to sustain SFRs above $1000 \, M_{\odot} \, {\rm yr}^{-1}$ without significantly breaching the Eddington limit (e.g., Bussmann et al. 2013; Kamieneski et al. 2024). In a large sample of Herschel-selected candidate lensed DSFGs, Borsato et al. (2024) found rest-optical sizes to be \approx 3 times smaller than far-IR sizes, determined by Enia et al. (2018) to be \sim 2–3 kpc. However, these isophotal rest-optical sizes are S/N-dependent, and the far-IR sizes are derived from lower-

³³ https://pixedfit.readthedocs.io/en/latest/

 $^{^{\}overline{34}}$ To test this, we examined the 84th percentile of the derived A_V posteriors for the DSFG-1 and DSFG-3 bins. Only 12% and 8% (respectively) exceeded $A_V > 2.5$.

resolution Submillimeter Array imaging, both of which may bias results toward smaller optical-to-FIR size ratios.

In this work, we find 2 mm dust continuum effective radii of $R_{e,2\text{mm}}=1.6\pm0.2\,\text{kpc}$ and $2.1\pm0.2\,\text{kpc}$ for DSFG-1 and DSFG-3, respectively (Table 2). These values are quite consistent with other members of PASSAGES (Kamieneski et al. 2024) and other lensed DSFGs (e.g., Bussmann et al. 2013), and in line with what might be expected from the size–luminosity relation derived by Fujimoto et al. (2017) and their intrinsic luminosities of $\log[L_{\rm IR}/L_{\odot}]\approx12.5$. Given their apparent elongated morphology, suggestive of high-inclination disks (Figure 2), this seems to suggest a large region of ongoing obscured-mode star formation. However, higher-resolution dust continuum imaging is required in order to comment on this more robustly, as Arcs 1a and 3c are only marginally resolved at 2 mm.

The UV-NIR photometry captures primarily the unobscured mode of star formation, which is likely to be a small fraction of the total (obscured plus unobscured) SFR_{UV + IR} for such massive, highly star-forming galaxies (Whitaker et al. 2017). Regardless, it is still informative to investigate the spatial scales over which unobscured star formation is occurring, to gain insight into the driving mechanisms and present evolutionary stages of the galaxies. For example, galaxies with a higher central specific SFR (sSFR \equiv SFR/ M_{\star}) are likely undergoing inside-out growth, by which a spheroidal bulge component is built up in situ through gas compaction (e.g., Dekel & Burkert 2014; Zolotov et al. 2015; Tacchella et al. 2016a, 2018). In later stages, sSFR may be elevated in outer regions of the galaxy, pointing to inside-out quenching. This may be driven by morphological quenching (Martig et al. 2009; Genzel et al. 2014; Tacchella et al. 2015), where the central spheroidal component renders the disk stable against gravitational fragmentation of the molecular gas, even without requiring energetic feedback from a central starburst or active galactic nucleus (AGN).

Figures 4 and 5 show the spatially resolved bin-wise properties derived through SED fitting with PIXEDFIT and BAGPIPES, including corrections for magnification from our lens model. Given the variation in bin size, we primarily examine the surface densities of SFR and M_{\star} , or $\Sigma_{\rm SFR}$ and Σ_{\star} . As gravitational lensing conserves surface brightness, these properties do not need to be corrected for magnification. We also perform the same analysis for the high-magnification Arcs 1bc and 3ab, as a consistency check, in Appendix C. These arcs arise only from a portion of the galaxy that crosses inside the caustics (see Figure 2 and the red demarcation line in left panels of Figures 6 and 7). For that reason, we focus here primarily on Arcs 1a and 3 c.

For G165-DSFG-1 (Arc 1a), there appears to be a single central peak in $\Sigma_{\rm SFR} \approx 15\,M_{\odot}\,{\rm yr}^{-1}\,{\rm kpc}^{-2}$, and a roughly axially symmetric radial decrease (except for perhaps lower $\Sigma_{\rm SFR}$ in the northwest region). The stellar mass surface density Σ_{\star} also peaks in the center of the arc—log $[\Sigma_{\star}/(M_{\odot}\,{\rm kpc}^{-2})] \approx 9.5$ —although the peak is more consistent with an elongated ellipse parallel to the major axis of the arc. In fact, there appear to be two peaks in Σ_{\star} , with a slight dip between them corresponding to the peak in $\Sigma_{\rm SFR}$. Of possible relevance is the discovery by F24 that Arc 1a is actually composed of components at slightly different redshifts seen in

projection, as indicated in the source-plane reconstruction in Figure 2. The redder, southeasternmost portion (NIRSpec aperture NS 969) is found to be at $z = 2.2355 \pm 0.0003$, while the bluer region 0."2 (1.6 kpc in projection) more to the northwest (NS_46) is at $z = 2.2401 \pm 0.0002$ (i.e., a rest-frame redshift difference of $\approx 400 \,\mathrm{km \, s^{-1}}$ relative to the southeast clump). Cañameras et al. (2018) similarly found a secondary component in imaging of CO(4-3) in Arc 1bc, which they interpreted as evidence for a blueshifted molecular wind. This offset was only $-200 \,\mathrm{km \, s^{-1}}$ from the systemic redshift, but the lower value might be a consequence of only a portion of this component being lensed into Arc 1bc, as indicated in Figure 2. Nevertheless, the dust-obscured stellar component revealed in far greater detail by JWST might favor the scenario of interacting objects seen in projection, but follow-up interferometric observations of the molecular gas will offer more insight. Despite this, we still refer to the system as G165-DSFG-1, as it is not possible to segregate them with the current data, and as it seems likely that they will ultimately merge into one object.

There is uncertainty in the spectroscopic redshift of G165-DSFG-3, although it shares a color gradient similar to that of DSFG-1 (Figure 2), and an even clumpier distribution of Σ_{\star} (peaking at $\Sigma_{\star} \approx 10^{9.5}\,M_{\odot}\,\mathrm{kpc^{-2}}$), with as many as five distinct peaks along the major axis. This may be suggestive even of spiral arm structures within the plane of a disk, a history of recent minor mergers, or the result of gravitational fragmentation of molecular clouds throughout the galaxy. Without kinematic information, our interpretation is necessarily limited. The distribution of $\Sigma_{\rm SFR}$ (peaking at $\approx 8\,M_{\odot}\,\mathrm{yr^{-1}\,kpc^{-2}}$) here is elongated along the major axis and decreasing radially, not dissimilarly to that of G165-DSFG-1.

Combining the SFR and M_{\star} information yields a map of sSFR (or alternatively, the mass doubling time, sSFR⁻¹) on subkpc scales. This provides a direct measure of how and where the galaxies are actively growing (in tandem with the distribution of mass-weighted ages, also shown in Figures 4 and 5). In Section 4.3, we discuss the relation of these sSFR values to the resolved star-forming main sequence, but first we examine the relative values of sSFR as a function of projected galaxy radius. For G165-DSFG-1, there is a clear bimodality in sSFR, with more starbursting regions in the southeast versus the northwest (by nearly 1 dex). This may also support the picture of DSFG-1 comprising multiple orbiting clumps seen in projection, with one both forming stars more actively and containing greater dust content, based on the A_V map. The map of mass-weighted stellar ages also supports this picture, with the southeast component more or less entirely younger than \sim 100 Myr. Alternatively, if the orbiting clumps are not responsible for this effect, then there must be some other mechanism by which gas is driven preferentially to one side of the galaxy to form stars. While it remains to be confirmed that DSFG-3 lies at the same redshift, one might speculate that the asymmetry is driven by a recent gravitational interaction between the two DSFGs, with molecular gas driven toward the center of mass of the system to form stars.

If a similar morphology were seen in DSFG-3, this might support an interpretation of tidal interaction between DSFG-1 and DSFG-3. There is no such obvious asymmetry in DSFG-3, however. In fact, the scenario for DSFG-3 is rather different: here there is an extensive central starbursting region with sSFR>10 Gyr⁻¹, with patchy regions of more mild star

 $^{^{\}overline{35}}$ At 3 mm, we find $\sim 1.5 \times$ larger sizes of $R_{e,3\text{mm}} = 2.6 \pm 0.3$ for both DSFGs, consistent with contribution from synchrotron (Thomson et al. 2019).

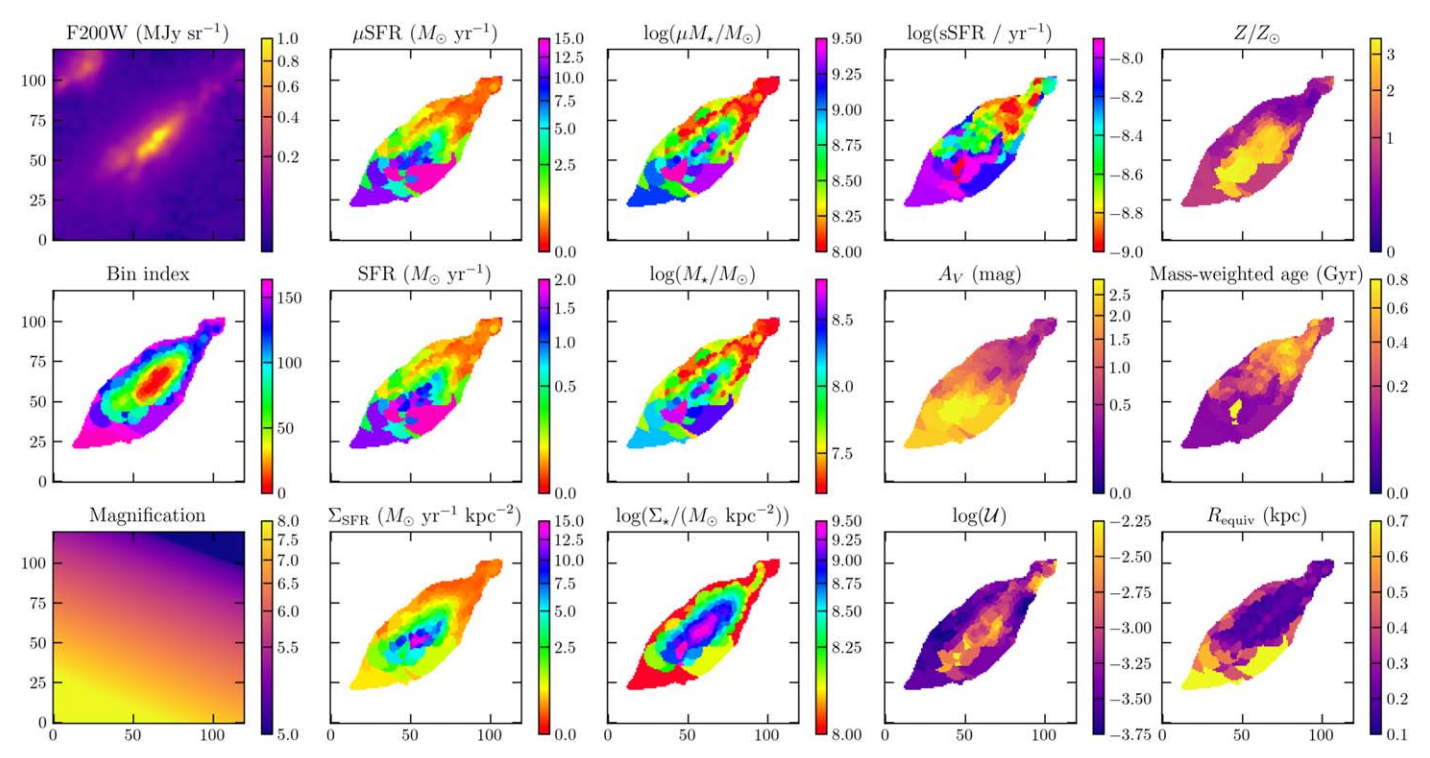


Figure 4. Spatially resolved properties of DSFG-1 (Arc 1a), including image-plane properties μ SFR and μ M_{*}, and their magnification-corrected intrinsic values, SFR and M_{*}. As bin size varies, these properties are best assessed through their respective surface densities, $\Sigma_{\rm SFR}$ and $\Sigma_{\rm *}$, which are also unaffected by magnification, as are the specific star formation rates, sSFR. Dust attenuation A_V , ionization parameter $\log(U)$, stellar metallicity Z, and mass-weighted ages are likewise assumed to not be affected by lensing magnification. These properties are inferred through SED fitting with BAGPIPES at a fixed redshift, z = 2.236. The bin index map shows the order in which the PIXEDFIT bins are allocated. The $R_{\rm equiv}$ panel shows the radius of a circle with equivalent area to each bin corrected for areal magnification factor μ , such that $R_{\rm equiv} \equiv (A\mu^{-1}/\pi)^{0.5}$. The field of view of each panel is 120×120 pix, or $3\rlap.{''}.6 \times 3\rlap.{''}.6$.

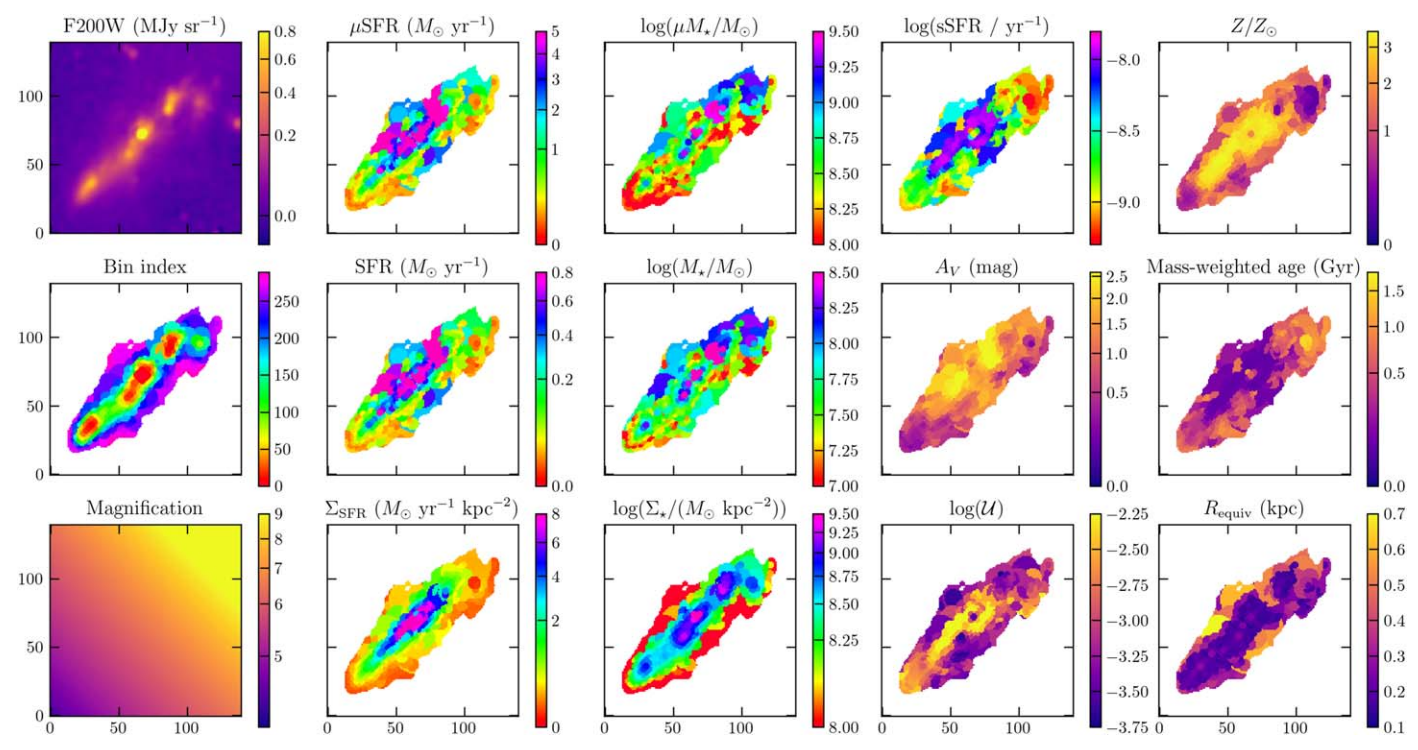


Figure 5. Spatially resolved image-plane properties for DSFG-3 (Arc 3c), as with Figure 4. Redshift is held fixed at an assumed z = 2.23. The field of view is 140×140 pix, or $4\rlap.{''}2 \times 4\rlap.{''}2$.

formation in the outskirts of the disk. However, the very central region (where Σ_{\star} peaks) has a slight depression in sSFR, which we speculate might reveal the very early stages of inside-out

quenching. In a similar resolved SED-fitting analysis, Giménez-Arteaga et al. (2023) suggested that dramatic spatial variations in sSFR could signal the important role of bursty star

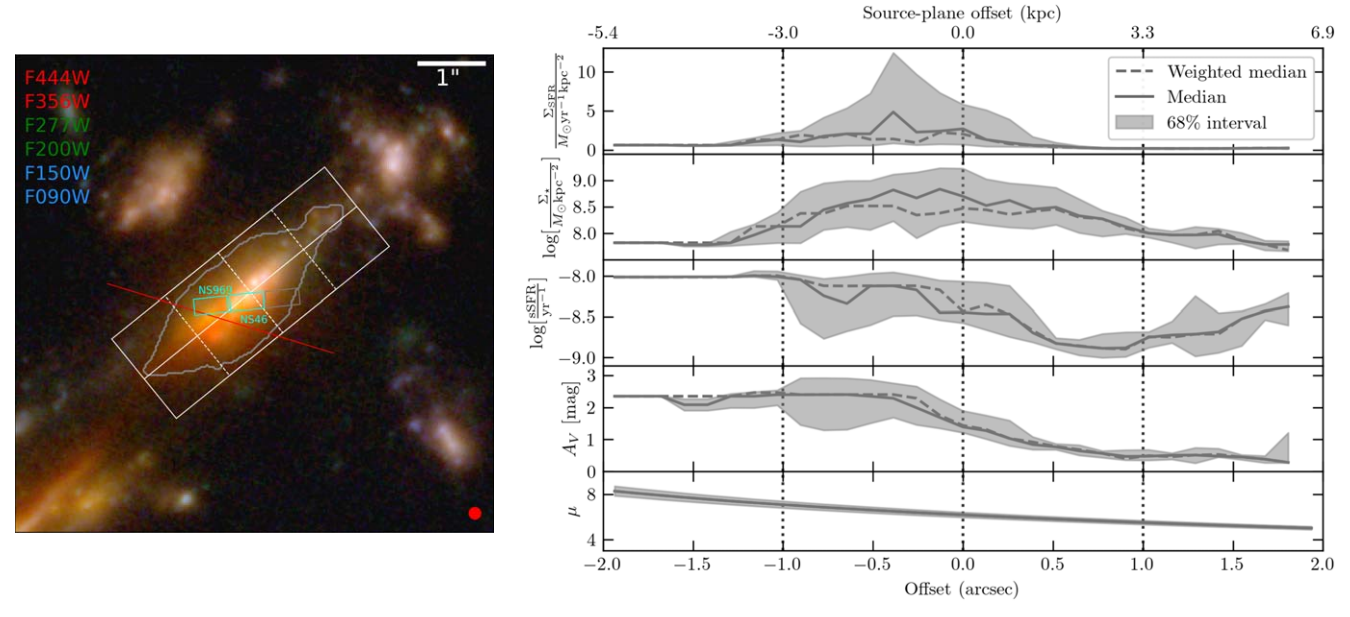


Figure 6. Linear profiles (right) of $\Sigma_{\rm SFR}$, log (Σ_{\star}), log(sSFR), A_V , and magnification μ created by taking bins along the major axis, shown over the RGB image-plane image of Arc 1a (left). Dashed white lines perpendicular to the major axis correspond to those in the right panel (for the center and at an offset of $\pm 1''$, where positive is northwest). The relative source-plane offsets in physical units (kpc), corresponding to the image-plane offsets of $\pm 1''$ and $\pm 2''$, are shown at the top; they are asymmetric due to the gradient in magnification. The F444W PSF is shown as a red beam in the left panel. The gray contour in the left panel shows the border of the bins used to make the profiles (as seen also in Figure 4). In each bin along the major axis, we show the weighted median (dashed curve) for each property, which does not account for overcounting pixels within each bin, so they are effectively weighted by the area of each SED fit bin within the major axis bin. The median (solid curve) counts each SED bin only once. The inner 68% interval is represented by shaded curves. A red line denotes where the source crosses the caustic curve according to our lens model; in this case, regions south of the line are triply imaged and those to the north are singly imaged. The locations of the NIRSpec MSA slits from F24 are shown in cyan and labeled for reference. As a caveat, properties at an offset > +1."0 are less reliable, given possible blending with a nearby object of unknown redshift.

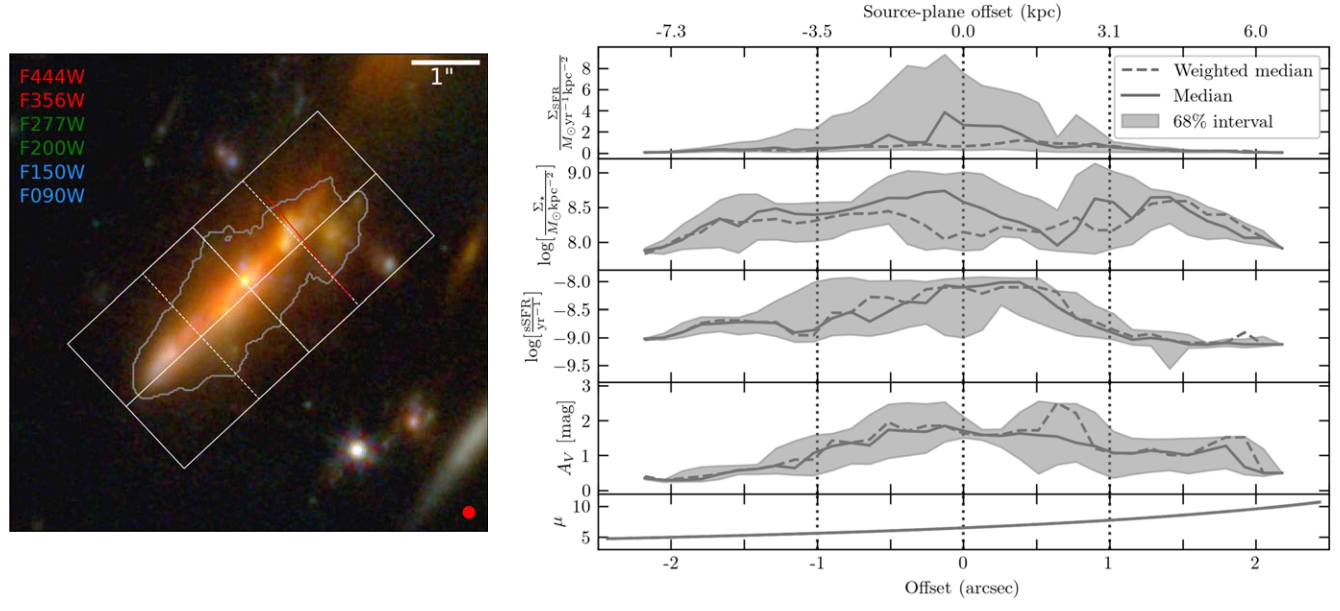


Figure 7. As with Figure 6, but for Arc 3c. In this case, the portion of the object northwest of the red line is triply imaged and the rest is singly imaged.

formation on small (kpc-sized) subgalactic scales. This stochastic star formation at fine spatial and temporal resolutions also makes it difficult to determine if lower sSFR is due to quenching or merely a period of inactivity between bursts.

To condense the overwhelming amount of information contained in Figures 4 and 5, we also extract profiles of $\Sigma_{\rm SFR}$, Σ_{\star} , sSFR, and A_V by taking linear profiles along the major axes of Arcs 1a and 3 c, which are shown in Figures 6 and 7. This approach is largely independent of inclination (Devour &

Bell 2017, 2019). In these plots, we take the PIXEDFIT bins from Figures 4 and 5 and compile these into binned slices of various properties along the major axis. We do this in two ways: for the "weighted median" curves, we do not account for overcounting pixels. That is, the PIXEDFIT-binned properties consist of regions of multiple pixels that are all assigned the same sSFR, A_V , etc. By not removing duplicate pixels, the result is effectively weighted by the area of each PIXEDFIT bin contained within the major axis slices. For the "median" curve,

these duplicates are removed, which gives all PIXEDFIT bins within the major axis slice equal weight. The inner 68% confidence intervals of pixel values are also shown as shaded curves.

Here, the skew in sSFR and A_V is even more readily observable for DSFG-1, with both transitioning between higher and lower values at a similar offset of $\approx +0.^{\circ}5$. It is also clear that the $\Sigma_{\rm SFR}$ peak is skewed relative to the broad Σ_{\star} plateau. For DSFG-3, the sSFR and A_V profiles are less pronounced, but are ultimately greater in the center than in the outskirts. They appear largely symmetric and thus more consistent with a simpler picture of a more centrally concentrated dusty starburst.

The ionization parameter is found to generally peak at $\log(\mathcal{U}) \approx -2.3$, consistent with the inner 500 pc core of the starburst M82 (Förster Schreiber et al. 2001; see also Engelbracht et al. 1998; Thornley et al. 2000). This is also slightly below the upper limit of $log(\mathcal{U}) = -2$ used for our SED fitting. For DSFG-1, the inner 68% confidence interval ranges from $log(\mathcal{U}) = -3.6$ to -2.7, while for DSFG-3 the range is log(U) = -3.3 to -2.3 (median uncertainty 0.3–0.4 dex), but these are likely poor estimates from SED fitting alone without spectroscopy. This is likewise the case for the estimation of stellar metallicity. While robust supersolar gasphase metallicity has been found in the nucleus of DSFGs even at $z \sim 4$ (e.g., Birkin et al. 2023; Peng et al. 2023), we do not place much confidence in the peak of $Z/Z_{\odot} \approx 3$ for G165-DSFG-1 and G165-DSFG-3 (apart from perhaps a believable radial decrease in both cases). However, we also find similar results of $Z/Z_{\odot} = 3.1 \pm 0.3$ for DSFG-1 and $Z/Z_{\odot} = 3.2 \pm 0.3$ from the global galaxy-wide SED fits described in Section 4.6, but we consider the unaccounted-for systematic uncertainties too great to further interpret these results.

4.2. A Favorable Dust Geometry for Detection of Supernovae?

We also remark that the widespread star formation and starbursting regions—along with some regions of decreased dust attenuation—have implications for the observable rate of supernovae, which we discuss in detail in Section 5.3. If the formation of massive stars (i.e., progenitors of core-collapse supernovae, or CCSNe) is not limited just to highly dust-obscured nuclear starbursts (Mattila & Meikle 2001), but is apportioned more evenly throughout the disk, then the turbulence in the ISM may result in a patchy, porous, and generally complex star versus dust geometry that would facilitate easier detection of supernovae (SNe) than a scenario of a uniform dust screen (Casey et al. 2014b; Narayanan et al. 2018). Likewise, star formation in the outskirts of the galaxy might also result in a "frosting" of unobscured UV-bright massive stars (e.g., Safarzadeh et al. 2017). This has not yet been tested in practice, but such DSFGs with evidence for galaxy-wide star formation events and inhomogeneous distributions of dust may thus be ideal candidates for continued monitoring for supernovae.

To get a sense of what supernova rates would be observed given different observing depths, we sum the resolved SFRs for only bins with attenuations below a certain value, as shown in Figure 8. For example, all bins of DSFG-1 are consistent with $A_V < 3$, so the summed (magnification-uncorrected)

 $\mu SFR_{A_V < 3} \approx 380 \, M_{\odot} \, yr^{-1}$ (see Table 3), while a value below $A_V < 2$ yields $\mu SFR_{A_V < 2} \approx 130 \, M_{\odot} \, yr^{-1}$, or 34% of the total. Likewise, for DSFG-3, the total SFR satisfies $\mu SFR_{A_V < 3} \approx 340 \, M_{\odot} \, yr^{-1}$ (Table 3), while $\mu SFR_{A_V < 2} \approx$ $190 \, M_{\odot} \, \text{yr}^{-1}$ (56% of total). Essentially, this implies that a shallower point-source sensitivity accounting for only up to 2 mag dust attenuation for supernovae would still detect them at a rate of 30% - 60% the intrinsic rate. This contrasts with the estimated \$20\% recovered rate of supernovae at optical wavelengths for some local ULIRGs (e.g., Arp 220 and Arp 299; Leaman et al. 2011; Mattila et al. 2012; see also Richmond et al. 1998). Mattila et al. (2012) and Dahlen et al. (2012) recognized that the increasing fraction of the cosmic star formation rate occurring within luminous infrared galaxies (LIRGs; $10^{11} < L_{\rm IR}/L_{\odot} < 10^{12}$) and ULIRGs (Magnelli et al. 2011) might result in dire, prohibitively large fractions of missed CCSNe at z > 1. However, the concrete differences in the distribution and driving mechanisms of star formation in distant versus local ULIRGs that have become apparent in recent years may work immensely in our favor, as we contend here.

Moreover, a more dispersed distribution of CCSNe is favorable for lensed objects like G165-DSFG-1 and G165-DSFG-3, as it improves the odds that any given supernova will occur within a multiply imaged region of the galaxy. If all SNe were confined to the galaxy nucleus, that would effectively require that this region falls by chance within the caustics in order for a multiply imaged supernova to ever be observed.

4.3. Resolved Star-forming Main Sequence in DSFG-1 and DSFG-3

Remarkably, most star-forming galaxies (SFGs) fall on a tight, nearly linear scaling relation in logarithmic scale (that evolves with redshift) between SFR and M_{\star} , known commonly as the star-forming main sequence, as has been borne out extensively (e.g., Brinchmann et al. 2004; Noeske et al. 2007a, 2007b; Daddi et al. 2007; Elbaz et al. 2007; Salim et al. 2007; Whitaker et al. 2012; Speagle et al. 2014; Renzini & Peng 2015). While the meaning behind this result is still somewhat subject to debate, it is commonly interpreted as an indication that most SFGs grow steadily when considered over >100 Myr timescales (although individual objects are likely to oscillate around the main sequence; e.g., Tacchella et al. 2016b). What remains highly uncertain is if and how this relation holds for ~kpc-scale regions within galaxies. In parallel with the integrated properties of SFR and M_{\star} , their respective surface densities $\Sigma_{\rm SFR}$ and Σ_{\star} are correlated through what is referred to as the spatially resolved star formation main sequence (rSFMS), first explored by Sánchez et al. (2013) and Cano-Díaz et al. (2016) locally and at higher redshift by Wuyts et al. (2013). A number of works since have supported the existence of the correlation, suggesting that it is physically motivated at subgalactic scales (Hemmati et al. 2014; González Delgado et al. 2016; Magdis et al. 2016; Abdurro'uf & Akiyama 2017; Hsieh et al. 2017; Maragkoudakis et al. 2017; Abdurro'uf & Akiyama 2018; Ellison et al. 2018, 2024; Hall et al. 2018; Liu et al. 2018; Medling et al. 2018; Cano-Díaz et al. 2019; Vulcani et al. 2019; Bluck et al. 2020a, 2020b; Enia et al. 2020; Morselli et al. 2020; Pessa et al. 2021, 2022).

In particular, Erroz-Ferrer et al. (2019) demonstrated that the relation between $\Sigma_{\rm SFR}$ and Σ_{\star} may be more fundamental; the global SFR- M_{\star} relation could be in part a consequence of the

 $^{^{36}}$ The eastern NIRSpec slit from F24 was consistent with a redshift of $z=2.2355\pm0.0003$, while the western slit yields $z=2.2401\pm0.0002$. This redshift difference is insufficient to affect the derived properties, but it is worth recalling that both components are contained within the offset range of $-1\rlap/.0$ to $0\rlap/.0$, and it is not clear yet how to visually separate them in these images.

Table 3
Properties of DSFG-1 and DSFG-3 from Rest-frame UV through Near-IR SED Fitting, and Corresponding SN Rates

Object	$\mu_{2\mu\mathrm{m}}$ SFR $(M_{\odot} \mathrm{yr}^{-1})$	SFR $(M_{\odot} \text{ yr}^{-1})$	$R_{\rm CC}^{}$ $({\rm yr}^{-1})$	$\log[\frac{\mu_{2\mu\mathrm{m}}M_{\star}}{M_{\odot}}]$	$\log[\frac{M_{\star}}{M_{\odot}}]$	$\log[\frac{\text{sSFR}}{\text{yr}^{-1}}]$	A_V (mag)
Arc 1a (SED) Arc 1a (H α) Arc 1a (bin-wise sum)	280 ± 130 320 ± 140^{b} 380 ± 10	50 ± 20 60 ± 30^{b} 69 ± 3	0.5 ± 0.2 0.6 ± 0.3 0.72 ± 0.03	10.9 ± 0.1 10.5 ± 0.1^{b} 10.91 ± 0.01	$10.2 \pm 0.1 \\ 9.7 \pm 0.1^{b} \\ 10.17 \pm 0.02$	-8.5 ± 0.3 -8.4 ± 0.3^{b} -8.34 ± 0.02	$ 1.5 \pm 0.3 1.5 \pm 0.4^{\circ} \approx 1.0 \pm 0.8^{\circ} $
Arc 3 c (SED) Arc 3 c (bin-wise sum)	260 ± 110 440 ± 10	40 ± 20 75 ± 3	0.4 ± 0.2 0.78 ± 0.03	$11.1 \pm 0.1 \\ 11.06 \pm 0.01$	$10.3 \pm 0.1 \\ 10.29 \pm 0.02$	-8.7 ± 0.3 -8.42 ± 0.02	1.2 ± 0.2 1.2 ± 0.7
Arcs 1abc+3abc (UV-FIR) ^d	5560 ± 280	350 ± 70	3.6 ± 0.7	11.68 ± 0.03	10.48 ± 0.09	-7.93 ± 0.03	2.54 ± 0.04

Notes. We compute the UV-NIR SED-derived SFRs for Arcs 1a and 3 c (see Figure 14), and correct these for respective magnifications at 2μ m. These values are lower than the SFR_{IR} estimates, but this is expected given their large dust attenuations. In Appendix E, we fit the summed SED of both DSFGs so that the unresolved far-IR photometry can be incorporated. The intrinsic, combined SFR_{UV-FIR} is \approx 4 times the sum of SFR_{UV-NIR} for the two DSFGs, while the summed stellar masses are more consistent with the integrated value. We also compare with the properties derived through the H α measurement by F24, incorporating the two NIRSpec apertures that covered this object (but applying our 2 μ m magnifications from Table 1). In all cases, we find quite close agreement with our independently derived values.

^d Here, we use the total flux-weighted magnification for both DSFG-1 and DSFG-3 combined, $\mu=16\pm3$, to derive intrinsic values.

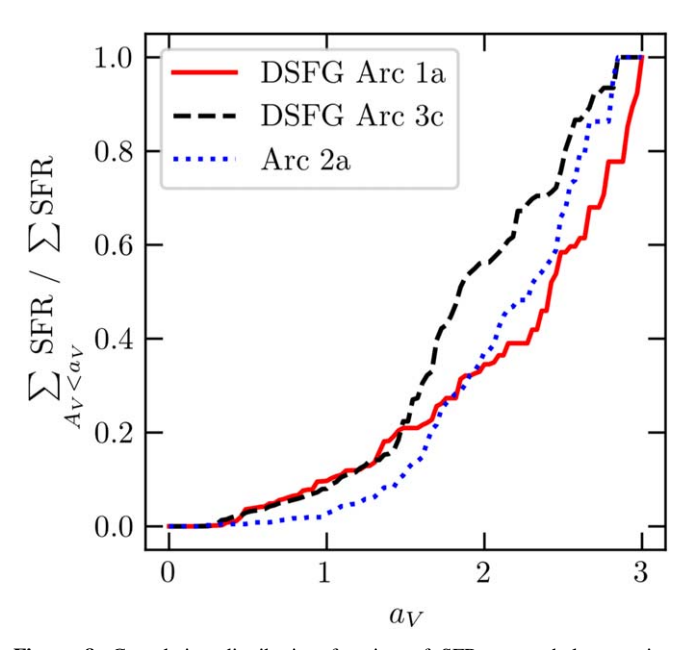


Figure 8. Cumulative distribution function of SFR_{UV-NIR} below a given threshold of dust attenuation, $A_V < a_V$, as determined through PIXEDFIT binning. For both the DSFGs and Arc 2a, 50% of the star formation is confined to regions with $A_V < 2$.

generally small variation for $\Sigma_{\rm SFR}$ and Σ_{\star} throughout a galaxy, combined with the size–mass relation (Shen et al. 2003; van der Wel et al. 2014) that scales both up and yields a linear relation between the integrated properties SFR and M_{\star} (Vulcani et al. 2019). The rSFMS has also been observed through simulations (e.g., Trayford & Schaye 2019; Hani et al. 2020; McDonough et al. 2023). However, we caution that the relation is likely nonuniversal, with nontrivial variations in the rSFMS from galaxy to galaxy (e.g., Vulcani et al. 2019; Ellison et al. 2021),

and the slope of the sequence may be influenced by the minimum size scales that are probed (e.g., Hani et al. 2020).

Figure 9 compares the distribution of individual PIXEDFIT bins in Arcs 1 and 3 in the $\Sigma_{\rm SFR} - \Sigma_{\star}$ plane. To facilitate comparison with work at lower z, we include only the bins with an area approximately equivalent to a radius of 150–1500 pc. Additionally, we expect that SED fitting at ≤ 100 pc physical scales (comparable to individual giant molecular clouds) becomes much less physically meaningful. As Vulcani et al. (2019) point out, it is highly possible for star clusters to migrate somewhat from the natal molecular cloud where they formed, which perturbs the one-to-one relationship between Σ_{SFR} and $\Sigma_{\rm gas}$ (and by extension, between $\Sigma_{\rm SFR}$ and Σ_{\star}). Since our method is applied to the magnified image-plane arcs, we first divide the bin areas by a fiducial magnification ($\mu = 6$ for Arcs 1 and 3, and $\mu = 8$ for Arc 2) before filtering to include only intrinsic sizes from ≈ 150 to 1500 pc. This size criterion excludes approximately 2% of bins in Arc 1, 23% in Arc 3, and 9% in Arc 2.

So far, there are rather few studies that have examined the rSFMS beyond the local Universe. Jafariyazani et al. (2019) used integral-field spectroscopy to place a sample covering 0.1 < z < 0.4 on the rSFMS, while Yao et al. (2022) likewise covered 0.2 < z < 0.4. Further afield, our comparison is primarily limited to Wuyts et al. (2013) at 0.7 < z < 1.5, Magdis et al. (2016) at 0.8 < z < 1.0, A18 at 0.8 < z < 1.8, and Nelson et al. (2021) at 0.8 < z < 1.5. Figure 9 shows the best-fit rSFMS relations from these works (over approximately the pertinent range in Σ_{\star} that each study dealt with), in addition to local relations from Cano-Díaz et al. (2016), Abdurro'uf & Akiyama (2017), and Ellison et al. (2024). Abdurro'uf & Akiyama (2017) and A18 first examined how the radial profiles of $\Sigma_{\rm SFR}(r)$, $\Sigma_{\star}(r)$, and sSFR(r) generally evolve with redshift, and by extension, how the rSFMS evolves. We can use this to predict where the pixels of the G165 DSFGs lie relative to the

^a Expected rate of core-collapse supernovae tabulated as in Table 2.

^b The H α -derived SFR and stellar masses from F24 are the summed values from NIRSpec apertures NS_46 and NS_969. The intrinsic (magnification-corrected) properties use the 2 μ m magnifications from Table 1. The sSFR is determined from this SFR_{H α} and the stellar mass, which is determined from an SED model that incorporated H α flux as a constraint.

^c As described in Section 4.6, the dust attenuation A_V is estimated from the Balmer-decrement-derived $E(B-V)_{\rm gas}=0.85\pm0.25$ for NS_969 F24 and a Calzetti et al. (2000) reddening law, $R_V=A_V/E(B-V)=4.05$. We finally impose a conversion to a stellar continuum color excess through $E(B-V)_{\rm stellar}=0.44E(B-V)_{\rm gas}$, per Calzetti (1997a). For the bin-wise dust attenuation, we provide the inner 68% interval for the bins' values.

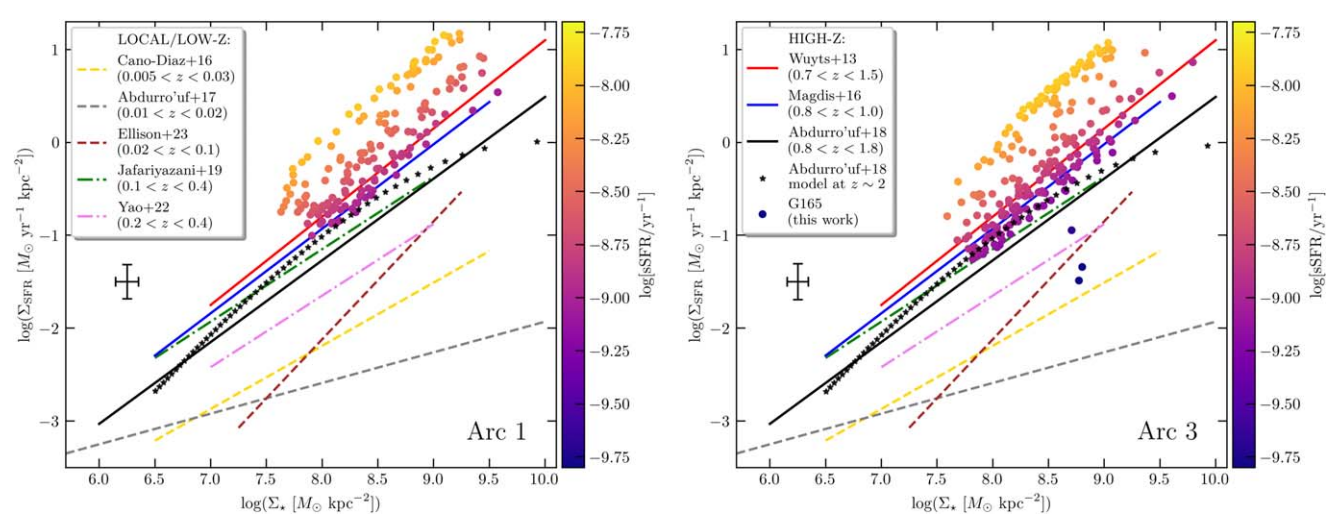


Figure 9. Individual PIXEDFIT bins of G165 DSFGs (Arc 1, left panel; Arc 3, right panel) placed on the resolved star formation main sequence, or $\Sigma_{\rm SFR}$ vs. Σ_{\star} . The color scale indicates sSFR. Median uncertainties are indicated in the center left. These properties are not corrected for lensing, as they are related to surface brightness and thus independent of magnification. However, we filter bins to only include those with areas equivalent to 0.15-1.5 kpc in radius, where we assume a fiducial magnification factor of $\mu=6$ for Arc 1 and $\mu=7$ for Arc 3 (i.e., image-plane areas are divided by this factor before filtering). A number of measurements of the rSFMS in the local Universe (Cano-Díaz et al. 2016; Abdurro'uf & Akiyama 2017; Ellison et al. 2024), at low z (Jafariyazani et al. 2019; Yao et al. 2022), and at $z\sim1$ (Wuyts et al. 2013; Magdis et al. 2016; A18) are shown as dashed, dashed-dotted, and solid lines, respectively. Legends in the two panels indicate the redshift tranges included for each. To make an approximate comparison at $z\sim2$, we extrapolate the redshift evolution model of $\Sigma_{\rm SFR}(r)$ and $\Sigma_{\star}(r)$ from A18 backward to z=2.24, as shown by black stars in the figure. The vast majority of pixels in each galaxy appear to be on or above the rSFMS, as 99% (89%) of the bins in Arc 1 (Arc 3) lie above this backward-evolved curve. In terms of areal fractions, these translate to $\sim100\%$ (Arc 1) and $\sim85\%$ (Arc 3).

rSFMS—with the caveat that the rSFMS is not universal from one galaxy to another.

For now, we employ the redshift evolutionary model of A18, which tracked progenitors from $z \approx 1.06$ ($t(z) \approx 5.5$ Gyr in our assumed cosmology) to $z \approx 0.02$ ($t(z) \approx 13.2$ Gyr), and extend it backward in time to z = 2.24 ($t(z) \approx 2.9$ Gyr). The result is shown as a dotted curve of black stars in Figure 9 (and see also Figure 15 of A18 for z = 0 to 1.1 in steps of $\Delta z = 0.11$). Relative to this curve, we find that the overwhelming majority $(99^{+1}_{-25}\%)$ of the bins in Arc 1 lie above the model rSFMS at $z \approx 2.2$ (accounting for $100^{+0}_{-17}\%$ of the total area), whereas $89^{+10}_{-29}\%$ of the bins in Arc 3 lie above (here accounting for $85^{+13}_{-27}\%$ of the area), (where the uncertainties are computed assuming 0.3 dex scatter in the rSFMS.). 37 This suggests that a clear majority of the bins shown in Figures 4 and 5 are actively star-forming (and some of them are starbursting). For these objects, at least, it appears to be the case that star formation is not confined purely to a central starburst region, but is widely distributed (often in clumps) throughout the plane of the disk. This has been demonstrated to be the case in recent years for a number of high-z DSFGs, especially in contrast with local ULIRGs (e.g., Chapman et al. 2004; Carilli et al. 2010; Ivison et al. 2010, 2011; Rujopakarn et al. 2011; Hodge et al. 2012, 2016, 2019; Hatsukade et al. 2015; Miettinen et al. 2015; Simpson et al. 2015; Swinbank et al. 2015; Sharda et al. 2018; Tadaki et al. 2018; Kamieneski et al. 2024). Here, we have demonstrated that the unobscured mode of star formation inferred from the UV-NIR SED is similarly widespread for DSFG-1 and DSFG-3, matching the widespread obscured star formation suggested by our finding of $R_e \sim 3$ kpc for the dust continuum. This is a result that we revisit in Section 4.5, using

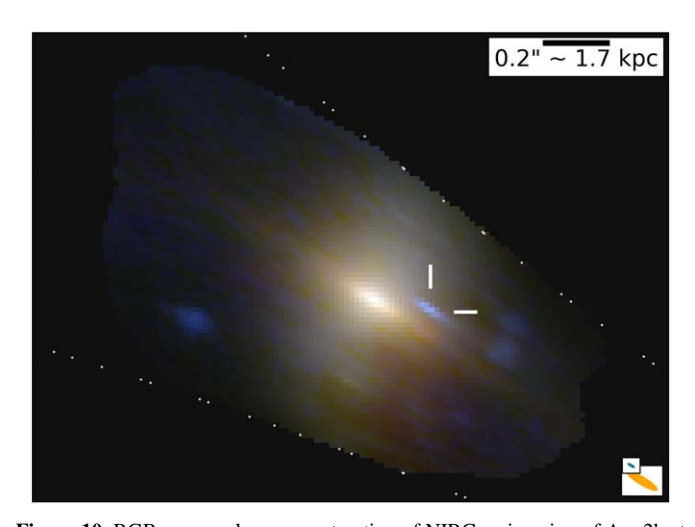


Figure 10. RGB source-plane reconstruction of NIRCam imaging of Arc 2b at z=1.78, as with Figure 3. Caustics are shown as sparse white dotted curves, and F090W/F444W source-plane PSFs are shown in the lower right as teal/orange beams, respectively. Only Arc 2b is shown in this reconstruction, as small but visually detectable offsets (\sim 0".05) in the source-plane location of Arcs 2a, 2b, and 2c are introduced from the lens model.

U-V and V-J colors alone for a largely independent and nonparametric characterization.

The evolutionary model we employ for the rSFMS was only designed for $z \sim 1$ to z = 0, and it is not clear how the evolution might extend to our objects at $z \approx 2.2$. However, the $z \sim 1$ sample from A18 includes objects up to $z \approx 1.8$, only 500–700 Myr after the G165 DSFGs. Their sample of highmass objects ($M_{\star} > 10^{10.5} \, M_{\odot}$, SFR $\lesssim 300 \, M_{\odot} \, \mathrm{yr}^{-1}$) is also selected to focus on face-on (low-ellipticity) disk-like objects, so it is subject to different systematic effects than our work. Nevertheless, properly quantifying the spatial extent of starbursting regions in G165 and other $z \sim 2$ galaxies will not be possible until a more detailed study of the rSFMS at higher

³⁷ While the main sequence has large intrinsic scatter, this binary calculation of the areal fraction "above" versus "below" the main sequence treats it as an exact discrete curve, in part to draw clear contrast with Arc 2 in Section 4.4. In this instance, "above the main sequence" does not equate to "starbursting."

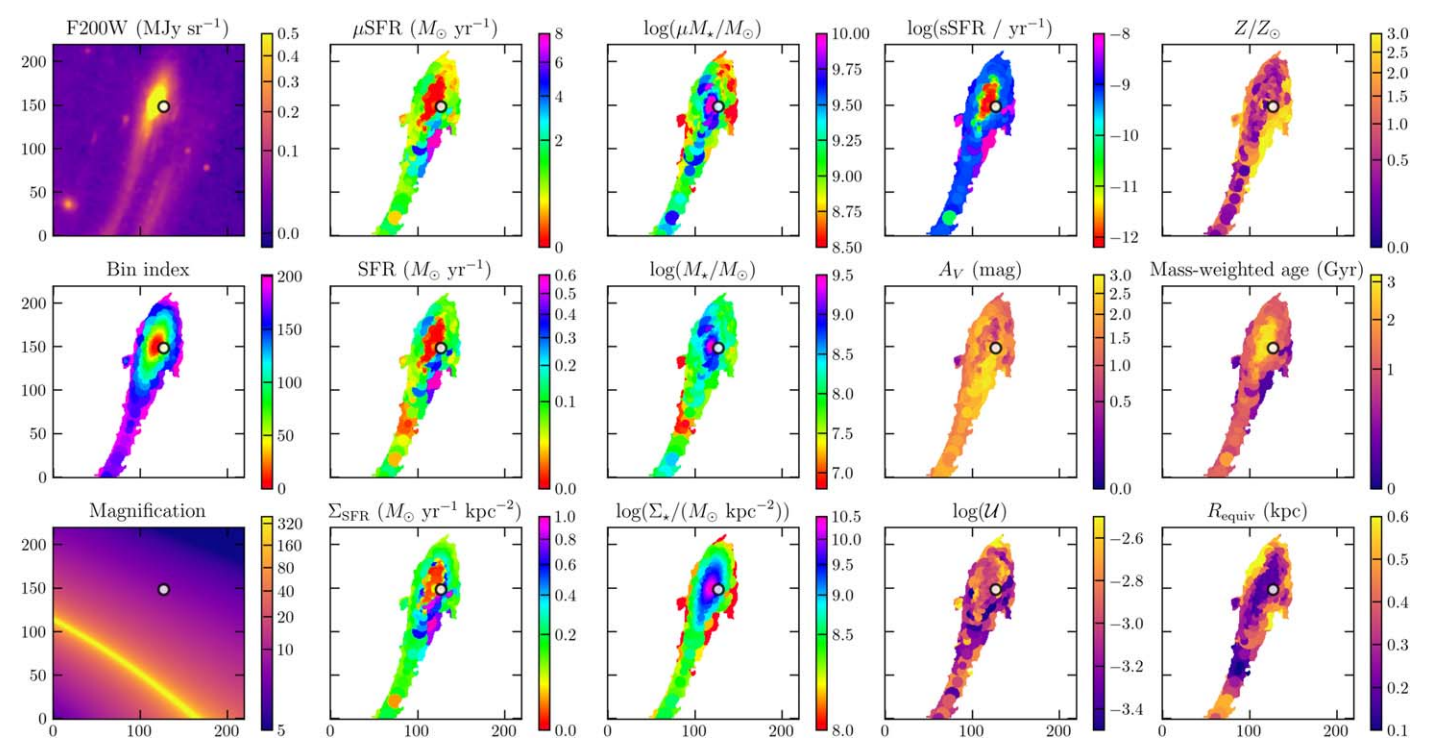


Figure 11. As with Figure 4, but for Arc 2a, which hosts SN H0pe, with a fixed redshift of z = 1.78. A small black circle indicates the location of the supernova. We choose this image for SED fitting rather than 2b or 2c, as it is the one in which the SN is faintest (and thus contaminates the least).

redshifts has been undertaken. With JWST covering an everincreasing number of strongly lensed objects, this is becoming more feasible, but beyond the scope of our current study.

4.3.1. A Mode of Elevated Star Formation Efficiency in the Resolved Star-forming Main Sequence

We also observe for the first time what appears to be a secondary "starburst" sequence ~ 1 dex above the "starforming" main sequence (Figure 9). This elevated mode of star formation is not dissimilar to the higher star formation efficiency (SFE) mode of the Schmidt-Kennicutt relation between molecular hydrogen mass $M_{\rm H_2}$ and SFR on resolved scales (Sharon et al. 2019). Recent works (e.g., Baker et al. 2023) have demonstrated that the (integrated) SFMS is not a fundamental correlation, but rather the result of two more fundamental scaling relations with less scatter: the Schmidt-Kennicutt relation, and the Molecular Gas Main Sequence (MGMS) between $M_{\rm H_2}$ and M_{\star} . Lin et al. (2019) likewise found (and have since been supported by Ellison et al. 2021 and Baker et al. 2022) that the correlation between Σ_{SFR} and Σ_{\star} is merely a byproduct of the correlations between Σ_{SFR} and Σ_{H_2} (which is the strongest correlation) and between Σ_{H_2} and Σ_{\star} . Together, this suggests a picture where the rate of star formation is generally driven (or regulated) by the availability of molecular gas fuel (although this is not necessarily a universal slope; see, e.g., Daddi et al. 2010), or neutral H I in the case of low-density environments at the outskirts of galaxies (Leroy et al. 2008). The correlation between $\Sigma_{\rm H_2}$ versus Σ_{\star} is suggestive of gas being preferentially accreted in regions of deeper gravitational potential, as traced by the distribution of stellar mass (Lin et al. 2019).

The bimodalities in the rSFMS and the Schmidt-Kennicutt relation may in fact be directly related if, for example, the MGMS that is hypothesized to link the two is not itself

bimodal. In other words, regions of elevated SFE could also be detected merely through $\Sigma_{\rm SFR}$ versus Σ_{\star} , under the assumption that each galaxy satisfies a unimodal $\Sigma_{\rm H_2}{-}\Sigma_{\star}$ relation (without large scatter). Without information on the molecular gas (or dust) distribution of the G165 DSFGs on similar spatial scales, or the gas excitation conditions through multiple spectral lines to accurately infer gas mass (e.g., Harrington et al. 2021), we are missing part of the picture in characterizing what drives stellar mass assembly across the galaxy. However, the rSFMS is still helpful in characterizing the widespread distribution of star formation and the rapid consumption of molecular gas.

4.4. Resolved Properties of the Massive Host Galaxy of SN H0pe

As discussed by Polletta et al. (2023) and F24, the rest-frame optical spectrum of Arc system 2abc, host to SN H0pe, shows evidence for a mostly intermediate-age stellar population at $\sim\!2$ Gyr (e.g., a strong NaD line and larger D(4000) value). The discovery of a Type Ia supernova itself helps support this, as these require delay times for white dwarf progenitors ($\sim\!3-8\,M_\odot$) to evolve off of the main sequence and reach the end of their lifetimes. This delay time distribution appears to peak at $\sim\!1-3$ Gyr (see Maoz & Mannucci 2012 and references therein). While the galaxy has evidence of some ongoing star formation, $10^{10.9}\,M_\odot$ of stellar mass has already been assembled by the time it is observed at z=1.78 (F24). We fit its UV-NIR SED with BAGPIPES in Appendix D, and remark on possible degeneracies with this narrow wavelength range that affect our interpretations. A source-plane reconstruction of the galaxy (using only Arc 2b) is shown in Figure 10.

Figure 11 shows the results of spatially resolved SED fitting for Arc 2a, which is host to SN H0pe. As this image is understood to arrive first (followed by 2c then 2b), the supernova is faintest in this image, having already faded

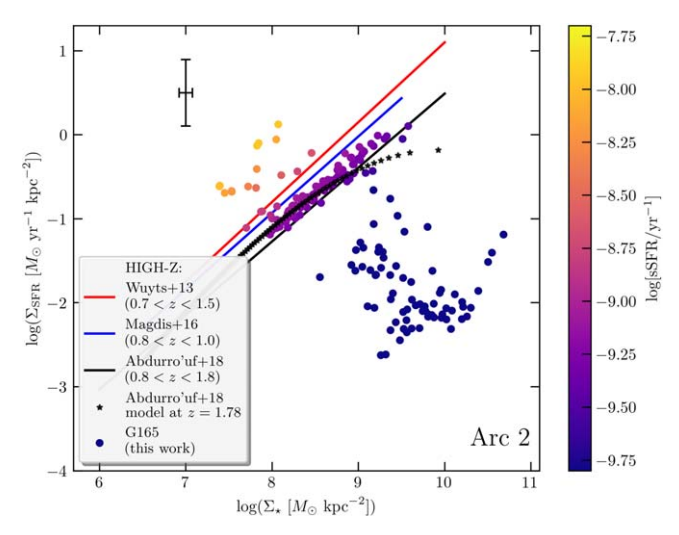


Figure 12. The $\Sigma_{\rm SFR}-\Sigma_{\star}$ plane for Arc 2, as with Figure 9. A fiducial magnification of $\mu=8$ is chosen to filter intrinsic bin sizes. Note that, given the larger stellar mass for this object, we shift the horizontal axis by 1 dex relative to Figure 9. Here, for a fiducial magnification of $\mu=8$ and filtering to only include bins with intrinsic equivalent radii of 0.15–1.5 kpc, we find that \approx 44% of bins lie above the redshift-evolved rSFMS to z=1.78 (accounting for \approx 57% of the galaxy area).

substantially in its light curve. We thus choose this arc for SED fitting, as it is subject to the least contamination from the SN. Moreover, it is also less contaminated by intracluster light than image 2b (which coincides with the axis of the merging cluster), and it is more isolated than 2c (which is near another very red arc, of currently unknown redshift). While the properties of this massive, mildly star-forming galaxy are naturally of interest in relation to SN H0pe, it also serves as a useful control for comparison with the more extreme DSFGs in this work.

Figure 12 shows the relation of Arc 2a to the rSFMS, which shows clear contrasts with Figure 9. While \approx 99% and \approx 89% of bins in Arcs 1a and 3c (respectively) lie above the center of the rSFMS evolved to their respective redshifts (or areal fractions of $\approx 100\%$ and $\approx 85\%$), merely $44^{+17}_{-36}\%$ of bins in Arc 2a are above the rSFMS at z=1.78 (or $57^{+29}_{-41}\%$ in terms of galaxy area). This is strongly influenced by the presence of a low- $\Sigma_{\rm SFR}$ (and low-sSFR) sequence at the center of the galaxy-with high stellar mass surface density, $\log (\sum_{\star} [M_{\odot} \text{ yr}^{-1}]) > 9$. This locus is entirely absent for the DSFGs, although the sSFRs are still above the nominal "green valley" transition at log(sSFR) $< -10.8 \text{ yr}^{-1}$ (Salim 2014). It also appears to be the case that many bins are clustered around the main sequence, adding some further confidence in the validity of backward-evolving the rSFMS model from A18, although it is true that this arc actually falls within the redshift range used for the model. There are a select number of regions that appear to be starbursting, perhaps in line with the conclusion by F24 that the galaxy is still star-forming (despite its very large stellar mass), as evidenced by the detection of $H\alpha$ emission (alongside spectral features that confirm the presence of a much older stellar population).

The large stellar mass and non-negligible ongoing star formation may in part help explain the favorable conditions leading to the discovery of SN H0pe, as the SN Ia rate is hypothesized to depend on an instantaneous term proportional to the SFR and on an extended term proportional to the stellar mass (e.g., Scannapieco & Bildsten 2005; Smith et al. 2012).

Similarly, the Type Ia SN Requiem (Rodney et al. 2021) was discovered in a low-sSFR host, classified as a Massive/Magnified Red Galaxy (MRG; Newman et al. 2018; Akhshik et al. 2020). Since then, an additional SN Ia ("Encore") has recently been found in the same host galaxy (Pierel et al. 2024a). In Section 5.3, we discuss the prospects for discovering core-collapse SNe behind G165, given the high rate of star formation. However, given the large stellar mass of the host of SN H0pe (Polletta et al. 2023; Frye et al. 2024), we also consider that the G165 field may be a source for the discovery of additional Type Ia SNe, as well (e.g., Shu et al. 2018; Holwerda et al. 2021).

4.5. Resolved UVJ Diagrams

The plane of U-V and V-J colors (or the well-known UVJ diagram) is an efficient method to discern between stellar populations that are red due to age versus those that are reddened by dust (e.g., Labbé et al. 2005; Wuyts et al. 2007; Williams et al. 2009; Brammer et al. 2011; Whitaker et al. 2011). For objects at $z \approx 2$, it was not practically feasible before JWST to reach the same resolution for rest-frame *J*-band (near-IR) imaging as for rest-frame (optical) U and V. With the advent of NIRCam, an essentially direct conversion from F115W, F200W, and F356W photometry to rest-frame U, V, and J (respectively) at $z \approx 2$ is now possible. For the range of 1.7 < z < 2.3, Miller et al. (2022) calibrated a linear relation for rest-frame U - V and V - J colors as a function of redshift and photometry in the NIRCam filters. While the classification of stellar populations with the UVJ diagram is imperfect, and made more uncertain by the assumptions of the conversion to rest-frame colors, it benefits from a reliance on very few pieces of information. No SED templates are imposed directly, and only three photometric measurements are employed (with which a robust SED fit would hardly be practical). Fortunately, the objects of interest in this work are all understood to lie within the redshift range for which the Miller et al. (2022) calibration is valid, so we use this semi-independent method alongside the measurement of sSFR from the SED fits (Sections 4.1 and 4.4).

The left panels of Figure 13 plot the rest-frame U - V and V-J colors of the bins in the DSFG-1 and DSFG-3 alongside arc 2a, all still shown in the image plane. As differential magnification is negligible within the small bin size (i.e., U, V, and J are all magnified equally in each bin), there is no need to correct the UVJ colors. The marker colors indicate sSFR as derived from the SED. Before introducing the selection criteria, we first remark on the approximate similarity in the locus for Arcs 1a and 3c. Arc 2a occupies a clearly different region, in particular toward redder U-V colors. These reddest U-Vbins include substantially lower sSFRs, about 3 orders of magnitude lower than the lowest-sSFR bins in DSFG-1 and DSFG-3. Referring to Figure 11, we find unsurprisingly that these are concentrated at the nucleus (central kpc) of the galaxy. Given the high stellar mass density here, $\Sigma_{\star} > 10^{10.5} \, M_{\odot} \, \mathrm{kpc}^{-2}$, it seems likely that this galaxy has an early formation redshift (Estrada-Carpenter et al. 2020) and has already built up a dense stellar bulge and started quenching inside-out (e.g., Fang et al. 2013; Ji & Giavalisco 2022, 2023; Ji et al. 2023). This is consistent with (but not necessarily implicitly due to) the gravitational stabilization of gas by an increasing dominance of a spheroidal bulge component, known as morphological quenching (Martig et al. 2009).

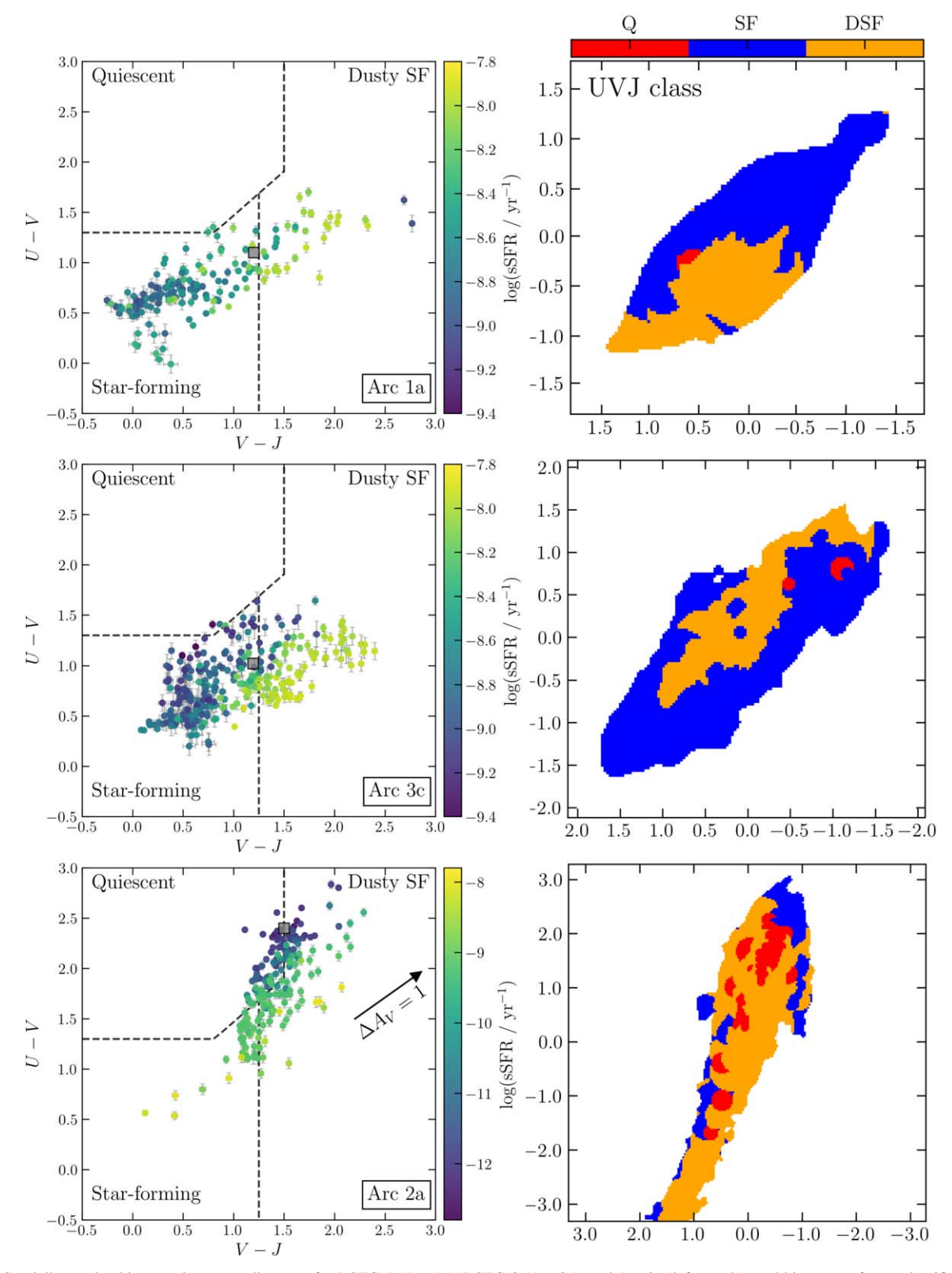


Figure 13. Spatially resolved image-plane UVJ diagrams for DSFG-1 (Arc 1a), DSFG-3 (Arc 3c), and Arc 2a (left panels), and bin maps of UVJ classifications (right panels); these are Quiescent (Q), Star-forming (SF), and Dusty Star-forming (DSF). The fields of view match those in Figures 4, 5, and 11; axes are shown in arcsec. The selection of quiescent galaxies is from Muzzin et al. (2013), while the distinction of SF vs. DSF is from Miller et al. (2022). Colors of points in the UVJ diagrams show sSFRs derived from the full observed-frame near-IR SED fit, with a different scale for Arc 2a given the wider range. A transparent gray square shows the location of the global UVJ colors for each arc. The black vector in the bottom panel indicates the effect of increasing A_V by 1 mag, per the Calzetti et al. (2000) attenuation curve.

We use the higher-redshift selection box for quiescent galaxies defined by Muzzin et al. (2013). While the distinction between star-forming versus dusty star-forming populations is

more arbitrary and less pronounced, we also show the $V-J>1.25\,$ cut from Miller et al. (2022). Differential magnification may indeed impact the global colors for each

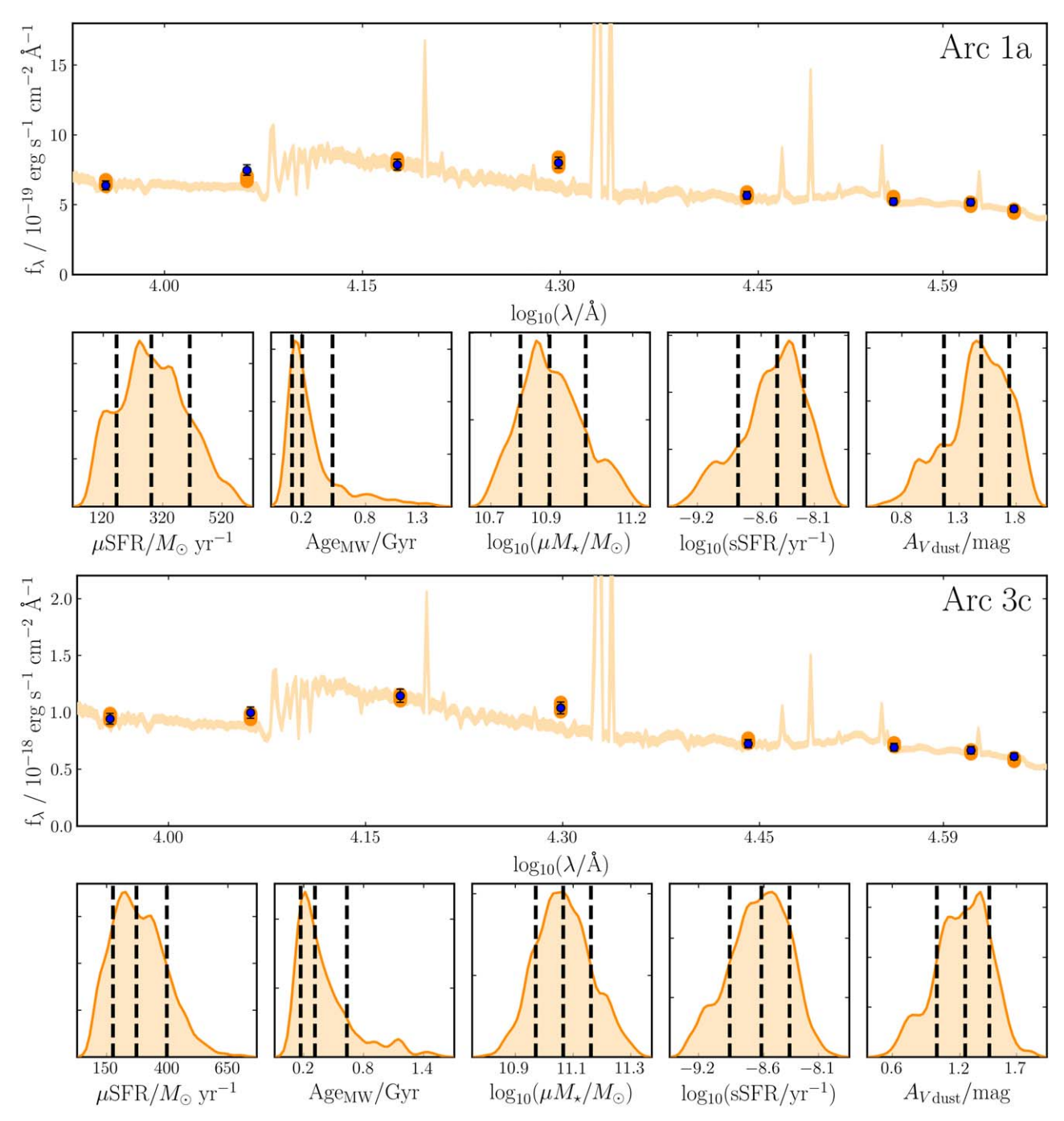


Figure 14. Best-fit near-IR SED and properties from BAGPIPES for Arc 1a (top) and Arc 3c (bottom). The top subpanels show the measured photometry as blue data points, with the best-fit SED as an orange curve. The expected photometry from the SED is shown by orange points. The bottom subpanels of each show the posterior distribution for apparent SFR (before correction for magnification), the mass-weighted age, the apparent (pre-lensing correction) stellar mass, the sSFR, and the dust attenuation A_V . Dashed vertical lines show the 16th, 50th, and 84th percentiles. These are distinct objects (not multiple images) but are very similar in these given properties.

of the three arcs (shown as gray squares in Figure 13; see discussion of global properties in Section 4.6). We find that DSFG-1 and DSFG-3 lie in very similar locations, safely in the star-forming/dusty star-forming region, but essentially close to the dividing line between the two. Arc 2a, on the other hand, lies on the cusp of the division between quiescent and dusty star-forming. The right-column panels of Figure 13 show the classification of bins from the *UVJ* diagram as quiescent (Q), star-forming (SF), and dusty star-forming (DSF). Curiously, while there is a greater presence of quiescent regions in the

massive galaxy seen in Arc 2a (relative to the DSFG arcs 1a and 3c), a clear majority of the galaxy's area consists of stellar populations consistent with the dusty star-forming region of the UVJ diagram, with only its outskirts being classified as less-obscured star-forming. Extending the quiescent selection box slightly to redder V-J colors would change the classification of a large number of bins from dusty star-forming to quiescent. Yet, the overall classification of this object as quiescent would likely be erroneous, despite its low sSFR (\sim 0.08 Gyr⁻¹; F24). Less-obscured star formation is found in the outskirts of the

galaxy, and the galaxy center (with peak Σ_{\star}) is coincident with the quiescent bins, perhaps signifying inside-out quenching. In Section 4.4 and Figure 12, we found that $57^{+29}_{-41}\%$ of the galaxy's area was consistent with being above the center of the rSFMS evolved to z=1.78. In other words, $43^{+41}_{-29}\%$ was quiescent based on sSFR, or at least on the lower end of the resolved main sequence; now, using the independent UVJ selection, we find that $\sim\!20\%$ of the area is classified as quiescent.

For the DSFGs, Arcs 1a and 3c, there are remarkably few regions that fall into the quiescent selection. For Arc 1a, there is a clear separation, with the southeast portion dominated by dusty star-forming populations and a northwest portion of regular star-forming populations. This could further support the orbiting clumps hypothesis (Section 4.1), with both components actively forming stars, but one hosting greater dust content (or at least, somehow more obscured due to projection effects, although this region is actually at a lower redshift). As for Arc 3c, the inner regions of the galaxy are DSF with outskirts that are classified as SF, with isolated embedded quiescent regions. These seem consistent with the observation of multiple peaks in Σ_{+} , perhaps as a result of a late-stage merger or the large-scale fragmentation of gas within the disk. In both DSFG-1 and DSFG-3, the most active star formation (highest sSFR) is clearly concentrated in the DSF box, which is to be expected given the connection between starbursts and dust obscuration (e.g., Whitaker et al. 2017).

4.6. A Comparison of Integrated versus Resolved Properties

In addition to the spatially resolved SED fitting, we also use BAGPIPES to measure global properties of G165-DSFG-1 and G165-DSFG-3 (Figure 14). For simplicity, we measure the photometry of the counterimage arcs 1a and 3c, as these contain the entire object (in contrast with the high-magnification arcs 1bc and 3ab, which arise from only a small fraction of their respective sources). Moreover, the magnification gradient for these counterimages, while not entirely negligible, is much smaller. After convolving all filters with a kernel to match the PSF of the coarsest-resolution filter (F444W), we use PHOTU-TILS (Bradley et al. 2022) to capture Kron aperture fluxes (Kron 1980).

We fit the eight-filter photometry with BAGPIPES in an identical manner as for the pixel-by-pixel fluxes, described in Section 3.2, using the same set of priors. While we measure photometry at 2 mm, 3 mm, and 6 GHz (Table 1), these are only included in a combined SED fit for the sum of Arc 1a, 1bc, 3ab, and 3c. The resolution of these long-wavelength observations (\sim 1."1, \sim 1."3, and \sim 0."5, respectively) are much coarser than what is enabled by JWST (see Figure 3). Moreover, the synthesized beam of the ALMA observations is highly elongated, owing to this being a high-decl. (+42°) target for ALMA's southern latitude. Unfortunately, this elongation is essentially aligned with the orientation of greatest magnification, so lensing does not offer an easy remedy. With these parameters for the currently available data, it is therefore not worthwhile to attempt spatially resolved SED fitting with both ALMA and JWST, as only a few resolving elements cover the extent of the arcs.

However, we can make a comparison of SED fitting with versus without the inclusion of far-IR rest-frame photometry for the unresolved, combined SED of both DSFG-1 and DSFG-3 together. Flux measurements that better constrain the peak of

the dust SED at rest-frame 100 μ m are available (Cañameras et al. 2015; H16), but these all have resolutions of 8"5—in the case of the LMT AzTEC—or much larger. In Appendix E, we sum the NIR photometry of the four arcs to revisit the SED fit of Harrington et al. (2016). As shown by Battisti et al. (2019), the stellar mass of DSFGs can be underestimated by 0.3 dex with only UV to near-IR coverage (a discrepancy that is greatest for objects with $M_{\star} > 10^{10} M_{\odot}$). More broadly, for galaxies simulated with the Evolution and Assembly of GaLaxies and their Environments (EAGLE; Schaye et al. 2015) project and the SKIRT dust radiative transfer code (Baes et al. 2011), Dudzevičiūtė et al. (2020) found that even with UV-to-radio coverage, SED modeling resulted in a systematic underprediction of stellar mass by 0.5 ± 0.1 dex. It also appears to be the case that inclusion of far-IR photometry in an SED fit tends to reduce the inferred SFR (Pacifici et al. 2023), although Wise et al. (2022) found that SFR can be under- or overestimated (up to 1 dex) from UV to near-IR alone. For galaxies with lower $SFR_{UV-NIR} \lesssim 300 \, M_{\odot} \, yr^{-1}$, they found that adding FIR data boosted the estimated SFR; for high SFR_{UV-NIR} galaxies, FIR data lowered the estimated SFR. Indeed, in our case, DSFG-1 and DSFG-3 have a combined $SFR_{UV-NIR} \approx 90 M_{\odot} \text{ yr}^{-1}$, but the unresolved UV-FIR SED yields $SFR_{UV-FIR} = 350 \pm 70 \, M_{\odot} \, \text{yr}^{-1}$, a $\sim 0.6 \, \text{dex}$ increase (Table 3). As is also emphasized by Smail et al. (2023), spatially resolved "pixel-by-pixel" SED modeling is made significantly more robust by the inclusion of long-wavelength photometry at similar angular resolution, highlighting the particular need for submillimeter interferometry in this analysis.

Zibetti et al. (2009) first presented an important bias to consider when inferring the stellar mass of a galaxy: mass estimates based on global (galaxy-integrated) fluxes were 40% (0.2 dex) lower than those determined by summing over the map of stellar mass derived from spatially resolved SED fitting. This effect is the direct result of the stellar mass contribution from dust-obscured regions being underestimated through the unresolved photometry (although Sorba & Sawicki (2015, 2018) point out that an "outshining" bias from the youngest stellar populations may be responsible, as well). Song et al. (2023) found recently that, without coverage of rest-frame near-IR in SED fitting, M_{\star} can be overestimated by 0.2 dex, owing directly to an overestimate of both dust attenuation and stellar ages from only rest-frame UV and optical photometry. As shown in Table 3, there is excellent agreement in the stellar masses determined through integrated photometry versus a sum of stellar masses derived through resolved bin-wise SED fitting with PIXEDFIT, which may indeed be the result of photometric coverage out to rest-frame 1.4 μ m.

Table 3 also shows comparisons with the H α -inferred SFR and dust attenuation properties presented by F24 for G165-DSFG-1. These are the result of combining measurements from NIRSpec slits NS_46 and NS_969, the latter of which is labeled "Arc 1a" in their Table 4. We find strong agreement for SFR, especially within uncertainties: global μ SFR_{NIR} = 280 \pm 130 M_{\odot} yr⁻¹ versus spatially integrated μ SFR_{NIR} = 380 \pm 10 M_{\odot} yr⁻¹ versus μ SFR_{H α} = 320 \pm 140 M_{\odot} yr⁻¹. The stellar mass derived by F24 is not completely independent of our result, as they used a joint photometric and spectroscopic SED fit with FAST++ (Kriek et al. 2009; Schreiber et al. 2018). Whether due to the different SED fitting algorithms or to the exclusion of spectroscopic information, the stellar mass we

estimate— $\log[\mu M_{\star}/M_{\odot}]=10.9\pm0.1$ —is 0.4 dex larger than the value quoted in F24. Our assumption of a "single" SFH in the form of an exponentially declining "tau" model may underestimate the stellar mass by 0.1–0.3 dex relative to a multicomponent SFH (Michałowski et al. 2014; Carnall et al. 2019; Jain et al. 2024). Given the typical uncertainty of 0.1 dex in stellar mass for SED modeling at z>1 (e.g., Pacifici et al. 2023), or even slightly elevated uncertainty of \sim 0.3 dex for DSFGs (Michałowski et al. 2014), it is perhaps most likely that the statistically significant discrepancy is explained by the information provided by the near-IR spectroscopy (or perhaps the extrapolation from limited slit coverage of the source).

Finally, we compare the estimate of dust attenuation that we find from modeling the UV-NIR SED against that derived from the Balmer decrement in H α versus H β from F24. They measured $E(B-V) = 0.85 \pm 0.25$ for NS 969 (with which we choose to compare here, given its larger uncertainty). For a Calzetti et al. (2000) reddening law, or $R_V = A_V/E(B-V) =$ 4.05, this yields $A_V = 3.0 \pm 1.0$. However, this discrepancy with our smaller value of $A_V = 1.5 \pm 0.3$ can be explained by the typically larger color excess for ionized gas relative to stellar continuum. Calzetti (1997b) quantify this as $E(B-V)_{\text{stellar}} = 0.44 \times E(B-V)_{\text{gas}}$ (see Shivaei et al. 2015). Applying this correction to the value from F24, we recover $A_V = 1.5 \pm 0.4$, in superb agreement with our finding. For the diffuse ISM in the outskirts of galaxies, the ratio of $E(B-V)_{\text{stars}}/E(B-V)_{\text{Hii}}$ is larger than for stellar birth clouds in star-forming regions, and even approaches unity (e.g., Robertson et al. 2024). Our finding that a ratio of 0.44 is appropriate for DSFG-1 may actually be in line with our interpretation of widespread star-forming regions, but this claim is limited for now by the current spectroscopic coverage of just a narrow region of the arc.

5. Discussion

5.1. How UVJ Selection Breaks Down on Resolved Scales, and Possible Evidence for Radial Dust Transport within the Disk

There are at least a dozen bins for Arc 2a in Figure 13 with very low sSFRs $(\log[sSFR/yr^{-1}] < -11.5)$ that are still safely outside of the classical quiescent selection region and would instead be classified as dusty star-forming populations. The quiescent sequence has been found to evolve with age-Belli et al. (2019) found a best-fit relation for the median stellar age of $\log(t_{50} \text{ [yr]}) = 7.03 + 0.84(V - J) + 0.74(U - V)$. These redder colors in resolved U-V and V-J can thus partly be the result of older stellar populations (\sim 3 Gyr), but this model still severely underpredicts the finding of $V-J\approx 1.7$ and $U-V\approx 2.3$. Ultimately, the most likely explanation seems to be that these quiescent regions are more dust-attenuated than typically expected. The reddening vector of ΔA_V shown in Figure 13 implies that several of these low-sSFR bins have at least $A_V > 0.5$ mag. This may also be borne out by the finding of $A_V \gtrsim 1$ for nearly the entirety of Arc 2a in Figure 11. As some added confirmation, SN H0pe is located nearby this dusty quiescent region and estimated via light-curve fitting to be attenuated by $A_V = 1.21 \pm 0.05$ (Pierel et al. 2024b). While dust in quiescent galaxies is still very much an area of active research, owing to the difficulty this presents for observations (e.g., Gomez et al. 2010; Rowlands et al. 2012; Magdis et al. 2021; Donevski et al. 2023; and references therein), they are often assumed to be quite dust-poor. Revisions to the original

UVJ selection frequently exclude the V-J < 1.5 cut to accommodate older and dustier quiescent galaxies (van der Wel et al. 2014; Whitaker et al. 2015; Belli et al. 2019). For Arc 2a, this correction would appropriately enclose the low-sSFR bins within the quiescent regime, but it would also erroneously include regions with sSFRs that are over 2 dex larger (sSFR $\geq 0.5 \, {\rm Gyr}^{-1}$).

This might indicate a shortcoming of our interpretation of the classical UVJ selection when applied to resolved scales. In a way similar to how the resolved star formation main sequence breaks down at ~ 100 pc and smaller, owing to stars migrating from their parent star-forming clouds, the UVJ diagram presumably also breaks down when significant amounts of dust and metals formed in regions of active star formation are transported to adjacent, more quiescent regions. This can occur over short distances within the plane of the disk through turbulent motions in the ISM (Cho et al. 2003), but Vorobyov & Shchekinov (2006) showed that spiral stellar density waves could help shepherd dust several kpc in the radial direction over the course of ~ 1 Gyr (see also Mishurov et al. 2014).

The extra reddening seen may also be due to extraplanar dust that has been transported a few kpc into the circumgalactic medium by the likes of galactic-scale winds driven by supernovae and winds from massive stars (Mac Low et al. 1989; Norman & Ikeuchi 1989; Heckman et al. 1990; Heckman & Thompson 2017; Richie et al. 2024) or simply through momentum injection by radiation pressure (e.g., Ferrara et al. 1991; Murray et al. 2005; Thompson et al. 2015; Barnes et al. 2020; Kannan et al. 2021). However, it is not clear if extraplanar dust (or even a thick disk of dust) can constitute a large enough fraction of the total dust mass, as it is estimated to be <5% (Howk & Savage 2000; Popescu et al. 2000; Bianchi & Xilouris 2011; Seon et al. 2014). The vertical stability of the disk also plays a role, as diffuse distributions of dust appear to be more predominant in low-mass, slow-rotating disks (Dalcanton et al. 2004; Holwerda et al. 2012). This extraplanar dust is also typically thought to be highly filamentary in nature, associated with chimney vents and extending a few kpc from the midplane (Wang et al. 2001; Stein et al. 2020; Mosenkov et al. 2022; see also review by Veilleux et al. 2020). It is unlikely to provide the necessary column densities to reproduce the observed A_V over large scales (Thompson et al. 2004), especially when considering the effect of grain destruction by sputtering (e.g., Spitzer 1978). Admittedly, widespread large attenuations do not necessitate uniform, thick screens of dust; they merely need large quantities of dust to be spatially correlated with regions of visible starlight. We thus consider it most likely that the bulk of the dust responsible for the attenuation is still largely contained (and well mixed) within the disk.

Over larger, galaxy-wide scales, this effect is likely to be less of a concern, as *UVJ* colors will be biased in favor of the unobscured sightlines. For globally quiescent objects, this means that the more dust-free regions with older stellar populations will dominate. This appears to be the case for the global colors of Arc 2a, as the object just barely falls within the *UVJ*-quiescent regime. Relatively few studies so far have examined spatially resolved *UVJ* diagrams in the era of JWST (including Miller et al. 2022; Kokorev et al. 2023; Suess et al. 2023), so our speculation on the effect of dust transport is necessarily limited. Yet, we can expect a better understanding

of these systematics (and in what other circumstances the selection criteria break down; e.g., Leja et al. 2019) with time.

5.2. Starbursts or Not? The Proximity of DSFG-1 and DSFG-3 to the Star-forming Main Sequence

In Section 4.3, we considered the location of spatially resolved regions relative to the resolved star formation main sequence, but now we examine the position of DSFG-1 and DSFG-3 as a whole. For both DSFG-1 at z = 2.236 $(t = 2.88 \,\text{Gyr})$ and DSFG-3 at $z = 2.1 \,(t = 3.07 \,\text{Gyr})$, the Speagle et al. (2014) model for the evolution of the main sequence³⁸ yields $\log[SFR(M_{\star}, t)] \approx 0.8 \log M_{\star} - 6.2$. Using our derived stellar mass of DSFG-1 of $\log M_{\star} = 10.2$, we find $SFR_{MS} \approx 90 M_{\odot} \text{ yr}^{-1}$. The IR-inferred $SFR_{IR} \approx 320 M_{\odot} \text{ yr}^{-1}$ is therefore approximately 3.6 times that of the main sequence at this redshift. As for DSFG-3, with stellar mass $\log M_{\star} = 10.3$, $SFR_{MS} \approx 110 \, M_{\odot} \, \text{yr}^{-1}$, and the inferred $SFR_{IR} \approx 400 \, M_{\odot} \, \text{yr}^{-1}$ is likewise approximately 3.6 times that of the main sequence at this redshift. With distance to the main sequence defined as $\Delta_{\rm MS} \equiv \log_{10}({\rm SFR/SFR_{MS}})$, both cases yield $\Delta_{\rm MS} \approx 0.6 \, {\rm dex.}$ Adopting a $\Delta_{MS} \geqslant 0.6$ dex threshold (e.g., Rodighiero et al. 2011) for starbursts above the main sequence—chosen to be a factor of 2 above the typical scatter of ≈0.3 dex (Brinchmann et al. 2004; Noeske et al. 2007a; Daddi et al. 2007; Elbaz et al. 2007; Salim et al. 2007; Whitaker et al. 2012; Speagle et al. 2014; Tacchella et al. 2016b)—this means that DSFG-1 and DSFG-3 are only just marginally classified as starbursts.

While DSFGs with such high SFRs are often incorrectly presumed to lie universally within the starburst regime, Rodighiero et al. (2011) found that only $20\pm4\%$ of galaxies with SFR > $100 M_{\odot} \text{ yr}^{-1}$ satisfied the +0.6 dex criterion. Similarly, Barrufet et al. (2020) found that approximately 60% of DSFGs (in a sample of 185) have SFRs consistent with the star-forming main sequence. Indeed, many claims have been made that DSFGs simply occupy the high- M_{\star} end of the SFMS (e.g., Finlator et al. 2006; Dunlop 2011; Magnelli et al. 2012; Michałowski et al. 2012; Sargent et al. 2012; Targett et al. 2013; Koprowski et al. 2016; Dunlop et al. 2017; Elbaz et al. 2018; Drew et al. 2020; Pantoni et al. 2021; but contrast with Hainline et al. 2011, for example). Furthermore, for a set of 15 other lensed DSFGs in the PASSAGES sample (not including G165), Kamieneski et al. (2024) found that proxies for Δ_{MS} (namely, molecular gas depletion time and Σ_{SFR}) predicted broad consistency with the upper end of the starforming main sequence, but that they were not necessarily classified as starbursts. In this work, we have also found that the radial profiles of sSFR (Figures 6 and 7) are broadly consistent with those expected for starbursts from Nelson et al. (2021).

The finding that the DSFGs in the G165 field can be classified as starbursts may have some connection to the finding that they reside within a highly active star-forming environment (and possible galaxy overdensity) by F24—although Drew et al. (2020) contend that distance to the SFMS may be a poor indicator of recent merger activity. Regardless, the locus of high-z DSFGs on the SFR- M_{\star} plane helps to quantify the role of gas-supply-dependent, secular evolution (Davé et al. 2012). A more systematic examination of the

stellar masses of DSFGs—especially now, with JWST helping to circumvent their prohibitive degree of dust obscuration—will ultimately shed more light on their connection to the star-forming main sequence. For now, the inconsistency of DSFGs and SMGs lying on or above the main sequence (Hodge & da Cunha 2020) may ultimately arise from the apparent heterogeneity of the overall population (e.g., Hayward et al. 2011, 2012; Magnelli et al. 2012; Hayward et al. 2013).

5.3. Prediction of Observer-frame Supernova Rates from G165-DSFG-1 and G165-DSFG-3, and Prospects for Future Discovery

The connection of core-collapse supernova rates to SFRs is straightforward, as CCSN progenitors are short-lived massive stars, believed to range in mass from 8 to $50\,M_\odot$ (Nomoto 1984; Tsujimoto et al. 1997). The supernova rate can thus be tabulated as $R_{\rm CC} = k_{\rm CC} \cdot {\rm SFR}$, where the scale factor is derived from the IMF $\phi(M)$ as

$$k_{\rm CC} = \frac{\int_{8\,M_{\odot}}^{50\,M_{\odot}} \phi(M)dM}{\int_{0.1\,M_{\odot}}^{125\,M_{\odot}} M\phi(M)dM} \tag{1}$$

and essentially represents the fraction of the forming stellar populations that consists of CCSN progenitors. These lower and upper mass limits and a Kroupa (2001) IMF yield $k_{\rm CC}=0.0104\,M_\odot^{-1}$ (e.g., Strolger et al. 2015), which we adopt for this work to remain consistent with the SED fitting. A Salpeter (1955) IMF for the same 8–50 M_\odot progenitor range would yield $k_{\rm CC}=0.0070\,M_\odot^{-1}$ (e.g., Mattila & Meikle 2001; Young et al. 2008), but this difference is essentially canceled out by the corresponding effect on the SFR (e.g., Madau & Dickinson 2014; Ziegler et al. 2022).

With this in mind, the predicted rest-frame supernova rate for G165-DSFG-1 is $3.3 \pm 0.7~{\rm yr}^{-1}$ using the FIR-derived SFR, or $0.5 \pm 0.2~{\rm yr}^{-1}$ using the lower, UV-NIR SED-derived SFR (see Tables 2 and 3). For G165-DSFG-3, these rates are comparable: $4.2 \pm 0.8~{\rm yr}^{-1}$ (FIR) and $0.4 \pm 0.2~{\rm yr}^{-1}$ (UV-NIR SED). Before taking into account the multiplexing provided by multiple images of any SNe, these rates translate to observer-frame values for G165-DSFG-1 of $R_{\rm CC,obs} \approx 0.2~{\rm yr}^{-1}$ (SED) to $\approx 1.0~{\rm yr}^{-1}$ (FIR), and for G165-DSFG-3 of $R_{\rm CC,obs} \approx 0.1~{\rm yr}^{-1}$ (SED) to $\approx 1.3~{\rm yr}^{-1}$ (FIR).

However, for the most reliable rate estimate, we use the SFR from the best-fit UV-through-FIR SED for DSFG-1 and DSFG-3 combined, SFR_{UV-FIR} = $350 \pm 70 \, M_{\odot} \, \mathrm{yr}^{-1}$. This results in a total expected rest-frame rate of $R_{\rm CC} = 3.6 \pm 0.7 \, \mathrm{yr}^{-1}$, or a remarkable observer-frame rate of $1.1 \pm 0.2 \, \mathrm{yr}^{-1}$. This very high rate is derived only from the pair of DSFGs; however, as discussed by F24, the H α -derived SFR for the objects associated with Arcs 1abc and 2abc groups surpasses $500 \, M_{\odot} \, \mathrm{yr}^{-1}$, which comes from only the unobscured mode of star formation. Given that these groups appear to signal galaxy overdensities at $z \sim 2$, it may well be the case that $\gtrsim 1-2$ CCSNe yr⁻¹ may be observable for the G165 cluster. This makes the G165 field an extremely attractive target for follow-up monitoring campaigns with JWST, as even the six Frontier Field clusters (Lotz et al. 2017) all together would provide only

 $[\]overline{^{38}}$ The main sequence follows $\log[SFR(M_{\star}, t)] = (0.84 \pm 0.02 - 0.026 \pm 0.003 \times t) \log M_{\star} - (6.51 \pm 0.24 - 0.11 \pm 0.03 \times t)$, for the age of the Universe t in Gyr. This model uses a Kroupa (2001) IMF, consistent with our SFRs.

 $[\]overline{^{39}}$ Cosmological time dilation decreases the apparent rate of occurrence for SNe, $R_{\rm CC,\ obs}=R_{\rm CC}\cdot(1+z)^{-1}$, but it also stretches out the time for which a given supernova's light curve is detectable.

0.9 CCSNe per year, with a cadence of four 1 hr visits with F150W within a year (Petrushevska et al. 2018). Given the best-fit $A_V \approx 2.5$ from the UV-FIR SED, it is entirely feasible to detect the descendant supernovae with only modest integration with JWST. An appropriate cadence would be designed to span a baseline of at least several months, so that enough time elapses for a clearly observable light-curve evolution of any SNe (which is subject to a factor of 1+z in cosmological time dilation).

This last point is crucial, and it helps to answer the inevitable question of why no CCSNe have yet been discovered in G165, given that two follow-up visits were undertaken with JWST on 2023 April 22 and 2023 May 9 after the discovery of the Type Ia SN H0pe in imaging on 2023 March 30. At only +23 days and +40 days from Earth's perspective, this is a mere +8 days and +13 days in the rest-frame at $z \sim 2$, which is hardly sufficient to guarantee a CCSN detection. The cadence of observations for SN H0pe was designed for monitoring of a discovered event; a cadence for discovering new SNe will simply need to extend over a longer period of time.

6. Summary and Conclusions

With this work, we have examined in detail the magnified, massive galaxies at $z \sim 2.2$ behind the G165 galaxy cluster, including two luminous dusty star-forming galaxies (log $(M_{\star}/M_{\odot}) \approx 10.2$; SFR_{IR} $\approx 300-400 M_{\odot} \text{ yr}^{-1})$ and a massive galaxy that appears to be exiting a phase of dusty star formation $(\log (M_{\star}/M_{\odot}) \approx 10.8-11.0 \text{ and } SFR_{H\alpha} \approx 5-10 M_{\odot} \text{ yr}^{-1}; F24).$ This latter object has been the subject of intense interest as the host of a recently discovered triply lensed Type Ia supernova, SN H0pe. Yet, the lensed DSFGs are responsible for the intense submillimeter flux by which the cluster was first discovered (Cañameras et al. 2015; Harrington et al. 2016; Frye et al. 2019; Pascale et al. 2022), and we have sought to further elucidate their properties through recent imaging in the near-IR with JWST and in the millimeter-wave through ALMA. We also present a new parametric lens model for the G165 cluster, developed with LENSTOOL. This model was constructed predominantly for the purpose of predicting lensing time delays for SN H0pe, in order to compare with values measured independently through the photometric and spectroscopic light curve, and thus infer the Hubble constant H_0 . However, this model is also invaluable for reconstructing the intrinsic (i.e., magnification-corrected) properties of the lensed DSFGs.

Coincidentally, what was initially discovered as a single compact submillimeter source with Planck has turned out to be two DSFGs with a peculiar (almost uncanny) similarity, both strongly lensed by the foreground merging galaxy cluster. The source of a detection of CO(3-2) at z = 2.236 (H16; also Harrington et al. 2021) was identified as a merging image pair Arc 1bc, and the counterimage Arc 1a (Cañameras et al. 2018; Frye et al. 2019; Pascale et al. 2022). With new NIRCam and ALMA continuum imaging, it has become clear that the object identified as Arc 3ab (merging pair) and Arc 3c (counterimage) on the same side of the lensing cluster also harbors considerable dust and star formation. In fact, while the Arc 1abc system (which we denote G165-DSFG-1) is considerably brighter in dust continuum (primarily due to the contribution from the high-magnification Arc 1bc) and likewise presumably CO emission, the intrinsic properties are very similar to the Arc 3abc system (G165-DSFG-3), which may even have a larger SFR_{IR} $(400 \pm 80 \, M_{\odot} \, \text{yr}^{-1} \text{ versus } 320 \pm 70 \, M_{\odot} \, \text{yr}^{-1}).$

It is most likely that DSFG-3 also lies at $z \approx 2.24$ with DSFG-1, so that their CO(3-2) lines are blended at the 100 km s⁻¹ spectral resolution of LMT/RSR. This proximity ($\approx 1''$, <10 kpc) would certainly imply that the objects are in the early stages of a spectacular gas-rich major merger (with a nearly 1:1 mass ratio, each with log $(M_{\star}/M_{\odot}) \approx 10.2$). The color gradients that are clearly apparent in Figure 2 may even be the result of tidal disruption of molecular gas after a first passage, driving an asymmetry of dust-obscured star formation toward the center of mass of the system (which is most readily observable in DSFG-1; Figure 6). Moreover, the fainter Arc 3, 4, and 6 clumps that lie in between DSFG-1 and DSFG-3 (and predicted by the lens model to lie at the same redshift) could be additional evidence for such a significant gravitational interaction. Future spectroscopic follow-up and kinematic information for the molecular gas will ultimately be necessary to help resolve this open question.

Regardless of their distances along the line of sight, the presence of two strongly star-forming DSFGs only 1" apart in the sky is a remarkable finding. In fact, one could perhaps even make the case that this conjunction would be more impressive in the sky without the magnification and distortion contributed by the lensing galaxy cluster! More quantitatively, they share similar IR-inferred SFRs, as well as UV-NIR SED-derived SFRs ($50 \pm 20\,M_\odot\,\mathrm{yr}^{-1}$ for DSFG-1, $40 \pm 20\,M_\odot\,\mathrm{yr}^{-1}$ for DSFG-3), stellar masses $(\log(M_{\star}/M_{\odot}) = 10.2 \pm 0.1 \text{ versus}$ 10.3 ± 0.1 , respectively), and dust attenuation ($A_V = 1.5 \pm 0.3$ versus $A_V = 1.2 \pm 0.2$). Their intrinsic (source-plane) dust continuum sizes are $1.6 \pm 0.2 \,\mathrm{kpc}$ and $2.1 \pm 0.2 \,\mathrm{kpc}$. Unsurprisingly, given the well-known correlation of radio with the far-IR (e.g., van der Kruit 1971; de Jong et al. 1985; Helou et al. 1985; Condon 1992; Lisenfeld et al. 1996; Yun et al. 2001; Bell 2003; Murphy et al. 2006a, 2006b), they also have similar radio continuum fluxes ($S_{\rm 6GHz}/\mu \approx 30~\mu \rm Jy$ for Arc 1a and $\approx 20 \,\mu Jy$ for Arc 3c). Their position in the UVJ diagram is functionally identical $(U - V \approx 1.1, V - J \approx 1.2)$, so their similarities cannot be attributed to limited flexibility in SED fitting.

Given the diversity and heterogeneity of DSFGs as a population—see Smail et al. (2023) for another recent example of two DSFGs near each other behind a lensing cluster, but with markedly different properties—this chance ultra-close alignment of two remarkably similar DSFGs is very peculiar. While we do not wish to fully speculate on whether or not this is purely coincidence, it is maybe not entirely outside the realm of possibility that these objects could be associated with filamentary nodes of large-scale structure in the Universe. As discussed in our introduction, DSFGs are widely believed to be associated with galaxy overdensities and protoclusters (see the theoretical work by Chiang et al. (2013), and recent review by Alberts & Noble (2022) and references therein). This is similar to the association of protoclusters with high-redshift radio galaxies (HzRGs; e.g., Venemans et al. 2007; Miley & De Breuck 2008) or Ly α emitters (e.g., Keel et al. 1999; Umehata et al. 2015; Harikane et al. 2019) and extended Ly α nebulae, also known as Lyman Alpha Blobs (e.g., Steidel et al. 2000; Hennawi et al. 2015; Arrigoni Battaia et al. 2018; Ramakrishnan et al. 2023; review by Overzier 2016). These signposts, and their connections to each other, are still very much an active area of research. And indeed, Frye et al. (2024) found evidence of a substantial overdensity of $z \approx 2$ galaxies behind G165 through photometric redshifts (rivaling even the number of identified members of the foreground cluster at z=0.35, with >150 candidates). The authors also identified several groups of objects found serendipitously to lie at the same redshift (one association of six objects at z=1.8 and another of several galaxies at z=2.2) with the JWST NIRSpec Micro-Shutter Array (MSA). Given the limitations of how MSA slits could be arranged, there are almost certainly other members of these associations that are not yet uncovered. With this rich set of background objects, all strongly lensed by a massive merging galaxy cluster, the G165 field is sure to be the source of a wealth of future astrophysical discoveries.

We summarize the primary scientific findings of our work:

- 1. Through resolved SED fitting of DSFG-1 and DSFG-3, we find complex distributions of $\Sigma_{\rm SFR}$, Σ_{\star} , and A_V (which are of primary concern for this work). For DSFG-1, there is a noticeable asymmetry, with star formation and dust attenuation skewed higher toward the southeast, with the peak in Σ_{\star} essentially occupying a highly elliptical central region rather than a single peak. These likely are related to the presence of multiple orbiting components at slightly different redshifts in this arc (z=2.2355 versus z=2.2401).
- 2. In the case of DSFG-3, there is not clear asymmetry. Here, $\Sigma_{\rm SFR}$ is centrally peaked but again in a rather elliptical nuclear region. Stellar mass density Σ_{\star} , on the other hand, shows multiple distinct peaks throughout the disk plane, possibly signaling a history of (major or minor) merger activity. Dust attenuation A_V is patchy throughout the object, with two distinct peaks, neither of which seem to be at the galaxy center.
- 3. We examine the position of the spatially resolved regions (on scales of 150–1500 pc) on the resolved star formation main sequence, which extends the global relation down to subgalactic scales. There is a clear distinction between DSFG-1 and DSFG-3 versus the more quiescent (or at least inside-out quenching) host of SN H0pe, examined through Arc 2a. For the DSFGs, we even observe a possible sequence at an elevated mode of star formation efficiency.
- 4. By extrapolating the model from Abdurro'uf & Akiyama (2018) for the evolution of the rSFMS between $z \approx 1.8$ and 0 backward to $z \approx 2$, we gain an initial sense of what areal fractions of the two DSFGs and Arc 2a are consistent with being above the rSFMS. For the DSFGs, these star-forming/starburst regions account for an overwhelming portion of the area (80%–100%), in contrast with only $\sim 60\%$ for Arc 2a. This supports the picture of many luminous DSFGs sustaining large-scale star-forming events, which are difficult to fully explain through major mergers.
- 5. The two DSFGs occupy similar locations in the *UVJ* plane, as do the loci of their resolved, pixel-by-pixel colors. While not all regions are classified as dusty starforming, only a small minority would be classified as *UVJ*-quiescent, further indicating the presence of large-scale galaxy-wide star formation events in tandem with the rSFMS results.
- 6. For the more quiescent galaxy seen in Arc 2a (according to its global *UVJ* color), which is possibly undergoing inside-out quenching, we find a higher fraction of regions within the quiescent regime. Curiously, this object falls primarily within the dusty star-forming region of the

- *UVJ*-plane, with only a small area in the outskirts of the disk falling within the unobscured star-forming regime.
- 7. Comparing *UVJ* colors and SED-derived sSFRs indicates a possible breakdown of the classical *UVJ* selection on resolved scales. Moreover, we find evidence for a substantial degree of dust attenuation for the low-sSFR regions, including the region where SN H0pe is located. We suggest that this could be the result of efficient radial dust transport within the galaxy.
- 8. In comparing the properties we derive for DSFG-1 and DSFG-3 by using global galaxy-wide photometry versus SED fitting the spatially resolved photometry and summing the relevant properties, we find approximate agreement for both SFRs and M_{\star} . As Arc 1a also has an H α detection reported by F24, we also compare SFR_{H α} with SFR_{SED}, finding very close agreement. Comparing the attenuation A_V found through SED fitting versus through the Balmer decrement, we reach excellent agreement for $A_V = 1.5$, if we make the assumption that $E(B-V)_{\rm stellar} = 0.44 \cdot E(B-V)_{\rm gas}$ (Calzetti 1997b; Calzetti et al. 2000).
- 9. Using the global properties of DSFG-1 and DSFG-3, we find that they lie directly on the $\Delta_{\rm MS} = +0.6$ dex threshold above the star-forming main sequence to be classified as starbursts. The location of DSFGs on the SFMS is still subject to debate, but it is obvious that they cannot simply be uniformly considered starbursts or high- M_{\star} end main-sequence galaxies. In this case, we consider it perhaps notable that these DSFGs are starbursting despite being largely disk-like and without particularly obvious signs of merger activity, which is often responsible for a temporary elevation in sSFR.
- 10. Employing our lens model for the purpose of estimating the magnifications and time delays of the three images of SN H0pe, we find $\mu_a = 6.7 \pm 0.1$, $\mu_b = 9.8 \pm 0.3$, and $\mu_c = 8.9 \pm 0.3$, which are in reasonable agreement with the values estimated from the light-curve photometry. For relative time delays, our model predicts arrival time after image SN2a to be $\Delta t_{c,a} = 53 \pm 3$ days and $\Delta t_{b,a} = 106 \pm 2$ days. These are used in the inference of H_0 by Pascale et al. (2024).
- 11. Using the combined SFR inferred from the rest-frame UV to FIR SED, along with the information obtained through our lens model, we estimate the combined rate of corecollapse supernovae in DSFG-1 and DSFG-3 to be $3.6 \pm 0.7 \, \mathrm{yr}^{-1}$. With cosmological time dilation, this reduces to $1.1 \pm 0.2 \, \mathrm{yr}^{-1}$.

In reality, the rate at which we can detect SNe depends also on the control time, or the amount of time that a survey is capable of detecting a given SN (Zwicky 1938). The often patchy dust geometry of DSFGs also makes the prediction of how attenuated supernovae will be quite difficult. For this reason, the near-IR sensitivity of JWST may provide the safest observing strategy, but detections with the Vera C. Rubin Observatory's Legacy Survey of Space and Time (LSST) or the Nancy Grace Roman Space Telescope certainly cannot be ruled out (e.g., Hounsell et al. 2018; Petrushevska 2020). Moreover, the large-scale nature of the star formation events in these DSFGs lends itself well to increasing the chances of multiplexing the observed SN rate through multiple imaging by lensing, as this makes it more likely that a CCSN will occur in a region of the galaxy inside the caustics.

To this last point, we re-emphasize that these estimates come only from the two galaxies DSFG-1 and DSFG-3 alone; based on the $\gtrsim 100\,M_\odot\,\mathrm{yr}^{-1}$ integrated (obscured and unobscured) SFR for the $z\sim2$ group, F24 still estimate a rate of $\gtrsim1$ SNe yr⁻¹ from the observer's perspective, making a compelling case for a continued monitoring campaign of G165.

Acknowledgments

We wish to dedicate this paper to the memory of our colleague at the School of Earth and Space Exploration, Susan Selkirk.

P.S.K. would like to thank Ian Smail, Evan Scannapieco, and Philip Mauskopf for helpful discussions to improve this paper. This work was also improved meaningfully as a result of discussions P.S.K. had with colleagues while at the Aspen Center for Physics, which is supported by National Science Foundation grant PHY-2210452.

This work is based on observations made with the NASA/ ESA/CSA James Webb Space Telescope. The data were obtained from the Mikulski Archive for Space Telescopes at the Space Telescope Science Institute, which is operated by the Association of Universities for Research in Astronomy, Inc., under NASA contract NAS 5-03127 for JWST. These observations are associated with JWST program #1176 (PEARLS; PI: R. Windhorst). The JWST data used can be accessed via doi:10.17909/225y-k062. R.A.W., S.H.C., and R. A.J. acknowledge support from NASA JWST Interdisciplinary NAG5-12460, NNX14AN10G Scientist grants 80NSSC18K0200 from GSFC. C.N.A.W. acknowledges support from the NIRCam Development Contract NAS5-02105 from NASA Goddard Space Flight Center to the University of Arizona. E.F.-J.A. acknowledges support from UNAM-PAPIIT project IA102023, and from CONAHCyT Ciencia de Frontera project ID: CF-2023-I-506. C.C. is supported by the National Natural Science Foundation of China, No. 11803044, 11933003, 12173045. This work is sponsored (in part) by the Chinese Academy of Sciences (CAS), through a grant to the CAS South America Center for Astronomy (CASSACA).

This paper makes use of the following ALMA data: ADS/JAO.ALMA # 2021.1.00607.S. ALMA is a partnership of ESO (representing its member states), NSF (USA) and NINS (Japan), together with NRC (Canada), MOST and ASIAA (Taiwan), and KASI (Republic of Korea), in cooperation with the Republic of Chile. The Joint ALMA Observatory is operated by ESO, AUI/NRAO and NAOJ. The National Radio Astronomy Observatory is a facility of the National Science Foundation operated under cooperative agreement by Associated Universities, Inc. This research has made extensive use of NASA's Astrophysics Data System.

We also acknowledge the indigenous peoples of Arizona, including the Akimel O'odham (Pima) and Pee Posh (Maricopa) Indian Communities, whose care and keeping of the land has enabled us to be at ASU's Tempe campus in the Salt River Valley, where much of our work was conducted.

Facilities: JWST (NIRCam), ALMA, VLA

Software: APLPY (Robitaille & Bressert 2012; Robitaille 2019), ASTROPY (Astropy Collaboration et al. 2013, 2018, 2022), BAGPIPES (Carnall et al. 2018), BLOBCAT (Hales et al. 2012), CASA (McMullin et al. 2007), GLUE (Beaumont et al. 2015; Robitaille et al. 2017), LENSTOOL (Kneib et al. 1993, 1996; Jullo et al. 2007; Jullo & Kneib 2009), Ned Wright's Cosmology Calculator (Wright 2006), PIXEDFIT

(Abdurro'uf et al. 2021, 2022a, 2022b, 2022c), PHOTUTILS (Bradley et al. 2022).

Appendix A Lens Model Parameters

In Table 4, we provide the full set of best-fit gravitational lens model parameters for our characterization of the G165 cluster with LENSTOOL, in accordance with our strategy described in Section 3.1. Additionally, we supply the range in priors for each parameter, which is distributed uniformly in all cases. For priors on the image system redshifts, these are chosen iteratively based on photometric redshift information, where we widen the prior range for parameters where previous model iterations led to their posterior distribution pushing up against the boundary conditions. For selecting a single best-fit version of our current model, we opt for the median value of

 Table 4

 Best-fit Gravitational Lens Model Parameters for the G165 Cluster

				Highest-like-
		Prior	Median and 1σ	lihood
Parameter	Units	Range	Uncertainty	Solution
$\overline{x_1}$	[arcsec]	[-16.8, -6.8]	-13.4 ± 0.1	-13.6
y_1	[arcsec]	[3.2, 13.2]	$+9.08 \pm 0.07$	+9.18
e_1	•••	[0.0, 0.85]	0.40 ± 0.03	0.44
θ_1	[deg]	[-90, 90]	-24.0 ± 0.2	-23.9
r_{c1}	[kpc]	[0, 98.4]	17.8 ± 0.6	16.9
σ_1	[km s ⁻¹]	[0, 800]	476 ± 3	473
x_2	[arcsec]	[11.3, 21.3]	$+14.39 \pm 0.03$	+14.37
<i>y</i> ₂	[arcsec]	[-13.7, -3.7]	-8.73 ± 0.01	-8.75
e_2	•••	[0, 0.85]	0.11 ± 0.00	0.11
θ_2	[deg]	[-90, 90]	-18.8 ± 0.3	-19.1
r_{c2}	[kpc]	[0, 98.4]	43.7 ± 0.4	43.5
σ_2	$[\text{km s}^{-1}]$	[0, 800]	689 ± 3	688
σ_3	$[\mathrm{km}\ \mathrm{s}^{-1}]$	[0, 250]	87.4 ± 0.9	86.3
mag_0	[mag]	[17.0] ^a	17.0 ^a	
σ_0	$[\mathrm{km \ s}^{-1}]$	[120] ^a	120 ^a	•••
$r_{\rm core,0}$	[kpc]	[0.15] ^a	0.15 ^a	•••
$r_{\text{cut},0}$	[kpc]	[30] ^a	30 ^a	•••
<i>Z</i> ₃		[2.0, 2.2]	$2.11^{+0.01}_{-0.01}$	2.11
Z4	•••	[2.0, 2.2]	$2.12^{+0.01}_{-0.01}$	2.11
<i>z</i> ₆	•••	[2.0, 2.2]	$2.10^{+0.01}_{-0.01}$	2.11
z ₇ & z ₁₈		[1.4, 3.0]	$1.73^{+0.01}_{-0.01}$	1.74
z_{10}	•••	[1.5, 1.9]	$1.76^{+0.01}_{-0.01}$	1.73
z ₁₁	•••	[4.0, 4.6]	$4.60^{+0.00}_{-0.00}$	4.60
Z ₁₂	•••	[2.7, 3.2]	$2.72^{+0.03}_{-0.02}$	2.71
z_{13}		[3.2, 3.8]	$3.60^{+0.02}_{-0.02}$	3.64
Z ₁₄	•••	[2.0, 3.0]	$2.58^{+0.01}_{-0.01}$	2.57
z ₁₅		[2.0, 2.5]	$2.11^{+0.02}_{-0.01}$	2.11
z ₁₆		[1.4, 1.8]	$1.79^{+0.01}_{-0.01}$	1.80
Z ₁₇	•••	[5.5, 6.5]	$5.65^{+0.05}_{-0.06}$	5.62
Z ₁₉		[3.0, 4.0]	$3.91^{+0.06}_{-0.08}$	4.00
Z ₂₀	•••	[3.0, 4.0]	$3.96^{+0.03}_{-0.05}$	3.90
Z ₂₁		[1.0, 4.0]	$1.74^{+0.04}_{-0.03}$	1.74

Notes. Priors for all parameters are taken to be distributed uniformly within the provided range.

^a Parameter held fixed.

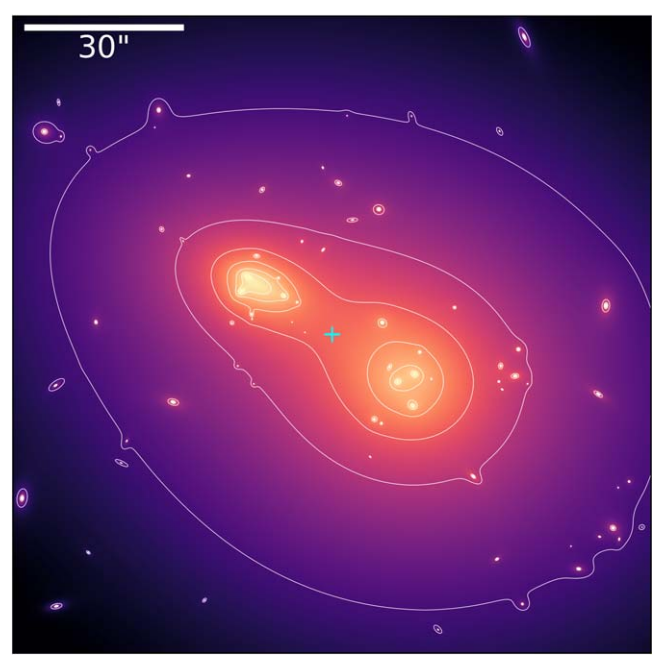


Figure 15. Convergence (κ) map of the G165 field from the median best-fit lens model, which is the dimensionless surface mass density (i.e., relative to the critical surface density). A cyan cross marks the center of this map, which is at (α , δ) = (11^h27^m15.156, +42^d28^m30.06). White contours indicate κ = [0.2, 0.4, 0.6, 0.8, 1.0, 1.2].

the posterior for each parameter, with the uncertainties described by the inner 68% confidence interval. This statistical measure is very likely an underestimate of the true systematic uncertainty in these parameters. Finally, we also provide the highest-likelihood (minimum χ^2) solution. For virtually all parameters, these highest-likelihood values are contained within the 68% confidence interval from the median solution, adding some assurance to the robustness of the model. Pascale et al. (2024) examine the impact of each parameter and unknown (i.e., image system redshifts) on the measurement of magnifications and time delays, in the context of inferring H_0 from SN H0pe.

Finally, Figure 15 shows the convergence map κ (or dimensionless surface mass density) of the full G165 field from our best-fit lens model.

Appendix B Calculating Time Delays for SN H0pe

SN H0pe and its host galaxy appear consistent with a "naked cusp" lensing morphology, with three images on the same side of the lens. This results from the source lying interior to the tangential caustic but exterior to the radial caustic in the source plane (e.g., Maller et al. 1997; Bartelmann & Loeb 1998; Keeton & Kochanek 1998; Lewis et al. 2002). If this interpretation is correct, then it is lensed into only the three images of SN H0pe and its host galaxy (Arcs 2a, 2b, 2c) that have already been identified.

With our best-fit lens model for G165, we computed the light travel-time surface as

$$\tau(\boldsymbol{\theta}) = \frac{D_{\Delta t}}{c} \cdot \phi(\boldsymbol{\theta}, \boldsymbol{\beta}), \tag{B1}$$

where

$$\phi(\boldsymbol{\theta}, \boldsymbol{\beta}) = \frac{1}{2} (\boldsymbol{\theta} - \boldsymbol{\beta})^2 - \psi(\boldsymbol{\theta})^2,$$
 (B2)

following the notation of Treu & Marshall (2016) and Treu et al. (2022). Here, θ is the set of apparent image-plane sky positions, β is the set of corresponding true (unlensed) source-plane positions, $\phi(\theta, \beta)$ is the (scalar) Fermat potential, and ψ (θ) is the scaled plane-projected gravitational potential. $D_{\Delta t}$ is the time-delay distance, defined as

$$D_{\Delta t} \equiv (1 + z_d) \frac{D_d D_s}{D_{ds}} \tag{B3}$$

for lens plane redshift z_d and the angular diameter distances D_d , D_s , and D_{ds} between observer and lens plane, between observer and source plane, and between lens and source planes, respectively. The Hubble constant H_0 is connected through $D_{\Delta t} \propto H_0^{-1}$ (Suyu et al. 2010). For this reason, with a model for the lensing potential $\psi(\theta)$, and an observation of the actual time delay between images through detection of a transient or variable source, one may infer H_0 .

To propagate the uncertainty in the lens model forward to the time delay predictions, we again randomly selected 300 realizations from the MCMC sampling, and calculated the light travel times at the position of SN H0pe in images 2a, 2b, and 2c. We then calculated the delays after the first image to arrive (2a), Δt_{ac} and Δt_{ab} . The results are shown in Figure 16. As a caveat, the uncertainties on time delays may be closely dependent on the positional uncertainty assumed for the model (here, taken to be 0."03). These values, along with the convergence κ and shear γ , are reported in Table 5. We also include our model-derived magnifications for the locations of SN H0pe, alongside the respective values derived from the photometric light-curve information from Pierel et al. (2024b). These absolute measurements of magnification are possible only because SN H0pe is a standard candle Type Ia supernova. We find general agreement within uncertainties. As discussed by Pascale et al. (2024), the fidelity of a lens model in reproducing the SN Ia-derived magnifications can be used to

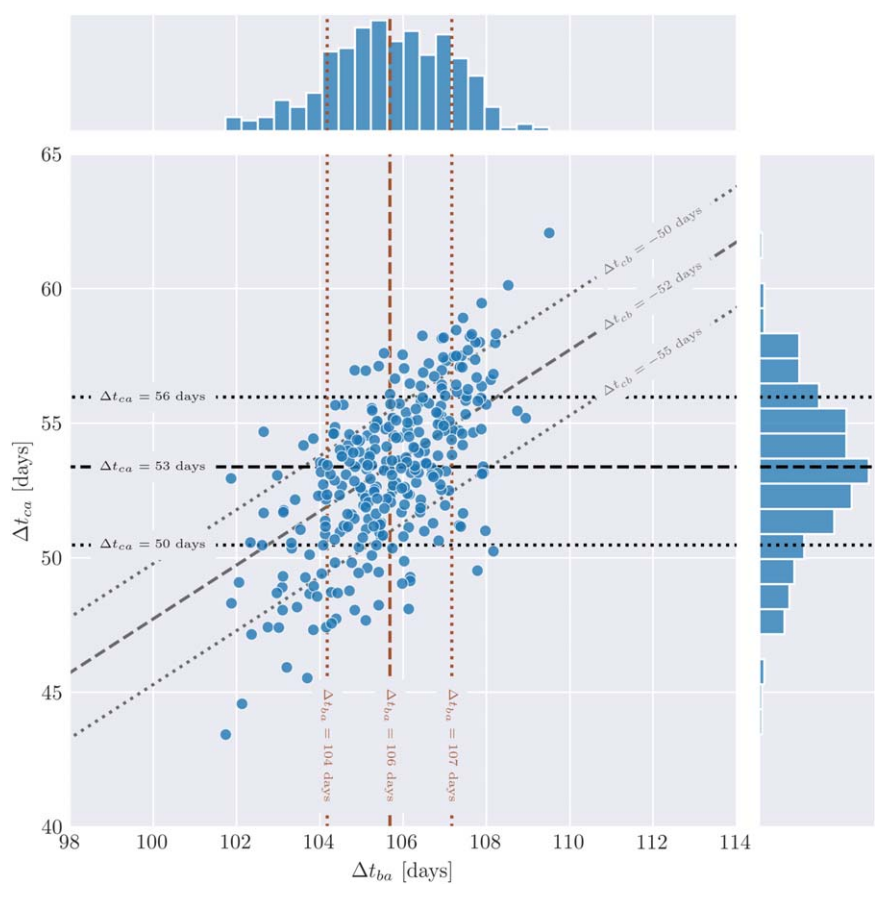


Figure 16. The time delay covariance plot for SN H0pe, showing 300 resampled iterations of the lens model posterior distribution, each yielding a different value of Δt_{ca} and Δt_{ba} (i.e., the delay in arrival time for images 2c and 2b following image 2a, respectively). Maroon vertical lines mark the median and 68% confidence interval for Δt_{ba} , black horizontal lines mark the same for Δt_{ca} , and gray diagonal lines for Δt_{cb} . Histograms on the top and right of the covariance plot show the one-dimensional distributions of Δt_{ca} and Δt_{ba} .

Table 5
Model-derived Time Delay Properties for SN H0pe

Image	Model Time Delay $\Delta t_{x,a}^{b}$ (days)	SN Ia $\Delta t_{x,a}^{a}$ (days)	$\mu_{ ext{model}}^{ ext{ b}}$	$\mu_{ m SNIa}^{a}$	κ^{b}	γ^{b}
SN 2a		•••	6.7 ± 0.1	$5.1^{+1.5}_{-1.7}$	0.571 ± 0.004	0.186 ± 0.002
SN 2b	106 ± 2	117 ± 10	9.8 ± 0.3	$9.2^{+3.5}_{-2.5}$	0.705 ± 0.003	0.434 ± 0.004
SN 2 c	53 ± 3	68 ± 11	8.9 ± 0.3	$7.4^{+1.4}_{-1.4}$	0.588 ± 0.005	0.243 ± 0.002

Notes

weight the various lens models involved in the inference of H_0 . We also find consistency with the predictions from many of the other lens models compiled by Pascale et al. (see their Figure 3), where the model from this work is referred to as Model 3.

Appendix C Source-plane Reconstruction and Resolved SED Fitting of High-magnification Arcs as a Consistency Check

Figure 17 shows the source-plane reconstructions of Arcs 1bc and 3ab, which are the highly magnified fold-configuration images. While these reconstructions are subject to very different effective source-plane PSFs compared to the lower-

magnification counterparts in Figure 3, they reveal broad agreement and instill some confidence in the lens model as applied to these objects.

Figures 18 and 19 show the same properties as Figures 4 and 5, but for their high-magnification counterparts, Arcs 1bc and 3ab. As both DSFGs barely cross over the caustic curves at their respective redshifts (Figure 2), only the southeasternmost portion of DSFG-1 and northwesternmost portion of DSFG-3 are triply imaged into 1bc and 3ab, and the remaining structure is singly imaged into the lower-magnification arcs 1a and 3c. In the image plane, we indicate the portion of each object that gets triply imaged using red dividing lines in Figures 6 and 7. This includes roughly one third of the area of

^a Magnifications and time delays derived from the SN Ia light curve determined by Pierel et al. (2024b)

^b The uncertainties in these values are purely statistical and likely underestimate the true systematic uncertainties. All are based on a fiducial $H_0 = 70 \text{ km s}^{-1} \text{ Mpc}^{-1}$. A more in-depth discussion, along with an investigation into the error budget of these values, is provided by Pascale et al. (2024).

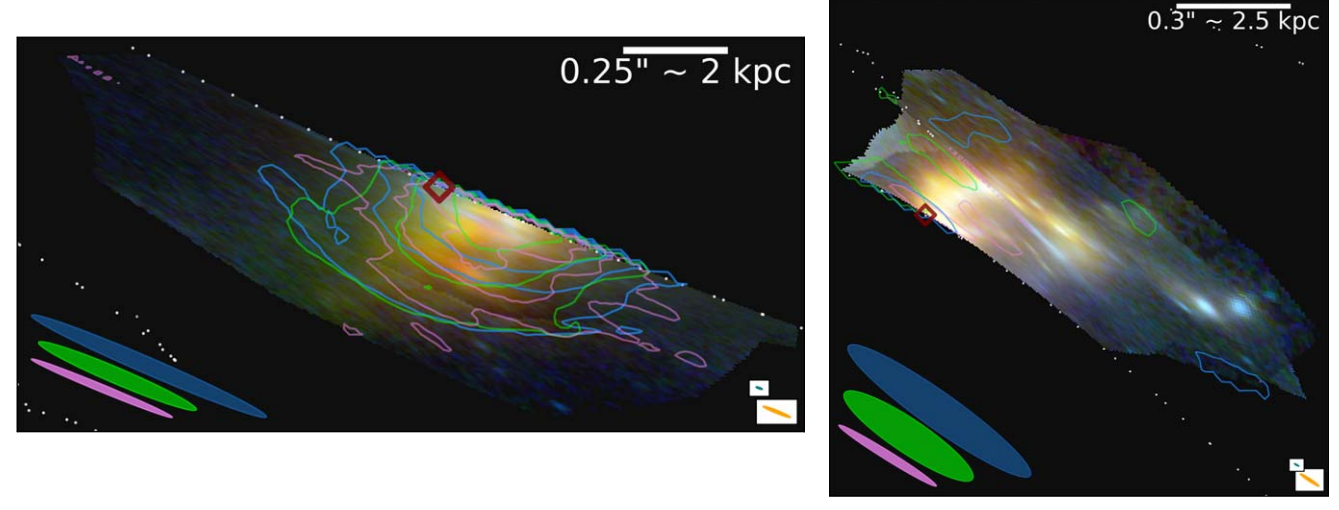


Figure 17. Source-plane reconstruction of only the highly distorted images 1bc (top) and 3ab (bottom), as with Figure 3, zoomed in to show greater detail. As the PSF varies much more severely across the extent of the arc, owing to the large magnification gradient, the beams shown are purely representative, and correspond to the position marked with a maroon diamond. This position near to the line of symmetry marks a bluer clump within the galaxy, which is denoted in the image plane as Arcs 1.2b and 1.2c by F24.

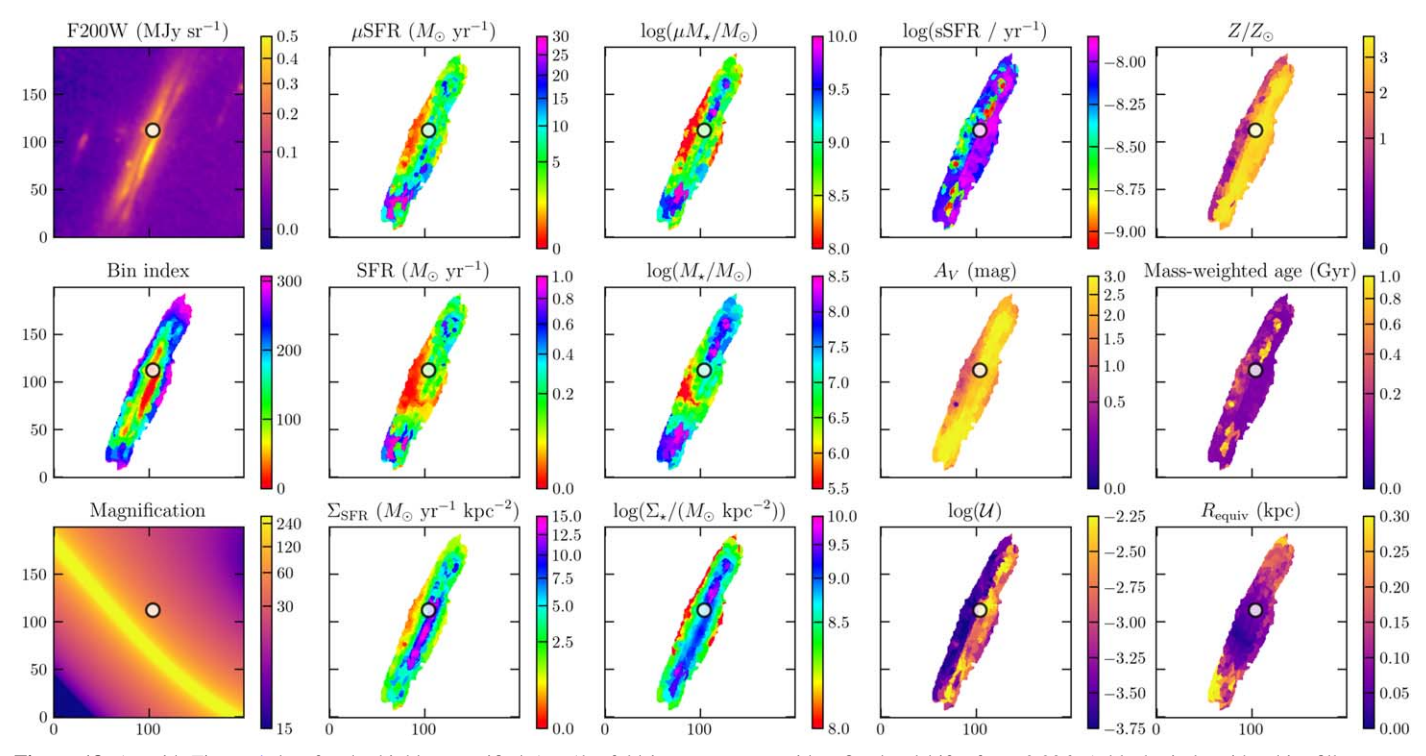


Figure 18. As with Figure 4, but for the highly magnified Arc 1bc fold image system, with a fixed redshift of z = 2.236. A black circle with white fill covers a foreground perturber (possibly within the galaxy cluster), for which the derived properties are not accurate (as the background redshift is held fixed). The field of view of each panel is 200×200 pix, or $6 \times 6''$.

DSFG-1 studied with resolved SED fitting, and closer to one fourth of DSFG-3.

At such small intrinsic scales (below 100 pc), it is not unreasonable to consider that the utility of SED fitting may begin to break down, especially when criteria requiring energy balance between UV/optical and far-IR are imposed (Smith & Hayward 2018). Even without this assumption, the individual bins exhibit lower S/N, resulting in greater uncertainties and degeneracies in derived physical properties. It is also rather difficult to interpret spatial variations in the image plane, as the

arcs are the result of a \sim kpc-scale source-plane region being magnified and highly distorted after lensing. Nonetheless, there is rough agreement in the key properties of $\Sigma_{\rm SFR}$, Σ_{\star} , and A_V , as we find in the corresponding regions of Arcs 1a and 3 c. Based on what we recover from this SED fitting, we identify a patchy distribution in dust attenuation A_V , but there is not significant variation here (although this is not a particularly robust characterization of the subkpc dust geometry). Moreover, it is difficult to determine if the clumpy structure of $\Sigma_{\rm SFR}$ and Σ_{\star} reveals the actual distribution of small-scale star-

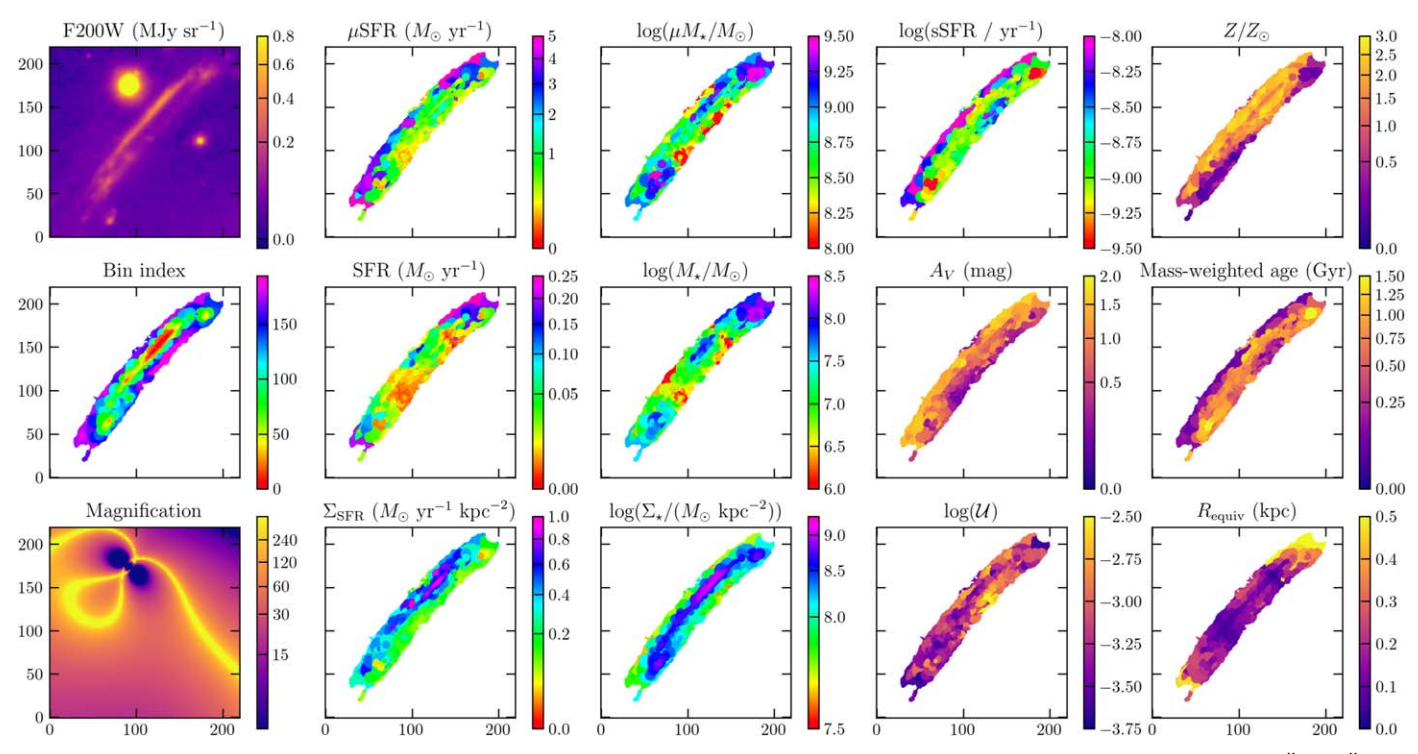


Figure 19. As with Figure 18, but for Arc 3ab at an assumed fixed redshift of z = 2.1. The field of view of each panel is 220×220 pix, or $6\rlap.{''}6 \times 6\rlap.{''}6$.

forming complexes, or if the variation is just the result of stochasticity in the SED fitting or inhomogeneous dust geometries (even below 100 pc scales).

Appendix D Integrated Properties of SN H0pe Host, Arc 2a

For ease of comparison, we also use the same choice of priors to fit the SED of Arc 2a, the host galaxy of SN H0pe, shown in Figure 20. We find that several parameters have wide posterior distributions or bimodalities, which limit our interpretations. This may be due to different stellar

populations contributing comparably to the integrated galaxy light (as revealed through the resolved SED fitting), or to degeneracies (e.g., between age and dust) that are poorly broken by the UV-NIR photometry given the shape of the SED. Intriguingly, F24 found $A_V = 0.9 \pm 0.2$ for Arc 2a from the Balmer decrement, which is in line with the lower- A_V peak of our posterior. Given these bimodalities, for integrated properties, we instead assume the quantities determined by F24, who incorporate the NIRSpec spectrum into the SED fit. This approach has a better chance at breaking these degeneracies and is thus more reliable.

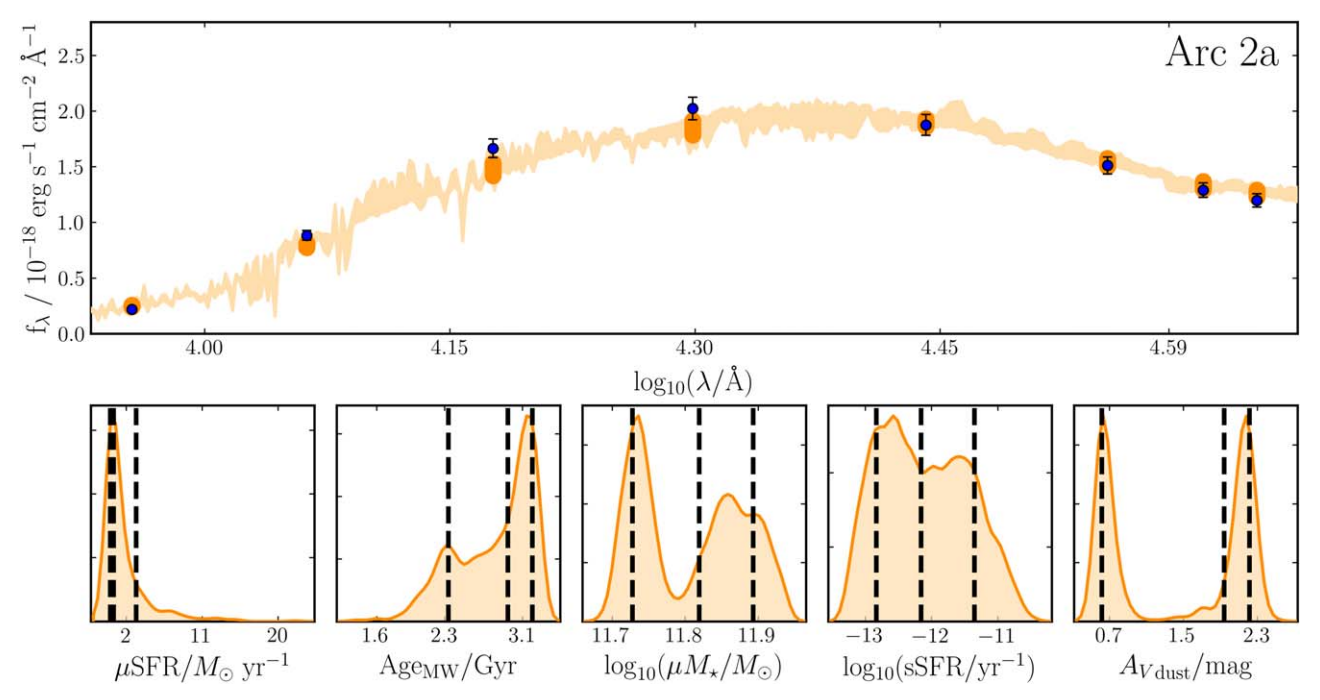


Figure 20. Best-fit near-IR SED and properties from BAGPIPES for Arc 2a at z = 1.78, as with Figure 14.

Appendix E Simultaneous UV-FIR Fitting of the Spatially Integrated SED

Inclusion of the 2 mm and 3 mm photometry presented in this work is desirable for constraining the dust SED, but their location at the tail end of the Rayleigh–Jeans regime renders them largely inconsequential for the fit. Instead, we fold them into a combined SED fit for Arcs 1a, 1bc, 3ab, and 3 c, so that we can take advantage of unresolved photometry measured by Harrington et al. (2016) from the Wide-field Infrared Survey Explorer (WISE) at $12/22~\mu m$ (Wright et al. 2010), Herschel Spectral Photometric Imaging Receiver (SPIRE) at $250/350/500~\mu m$ (Griffin et al. 2010), and LMT/AzTEC at 1.1 mm (Wilson et al. 2008). Planck photometry is excluded from the fit because of its high confusion noise. Then, NIRCam photometry is summed together for all four arcs to match.

Given the increased number of constraints on the SED, we include additional parameters for our BAGPIPES optimization, which pertain to the dust emission model (e.g., Draine & Li 2007.) These include the PAH mass fraction ($q_{PAH} \in [0.5, 4.0]$), the lower cutoff of the incident starlight intensity on the dust ($U_{min} \in [1, 25]$, effectively describing the dust

temperature distribution), and the fraction of dust heated by $U > U_{\min}$ ($\gamma \in [0.01,\ 0.99]$); these priors are all uniformly distributed and consistent with those used by Williams et al. (2019). As the far-IR coverage captures regions of higher attenuation than just UV-NIR alone, we also expand the upper limit on the prior on dust attenuation to $A_V < 8$. Redshift is held fixed at z = 2.236. The best-fit dust emission parameters are $q_{\rm PAH} = 3.9 \pm 0.2$, $U_{\rm min} = 22 \pm 2$, and $\gamma = 0.09 \pm 0.06$. The derived magnification-corrected SFR is SFR_{UV-FIR} = $350 \pm 70 \, M_{\odot} \, {\rm yr}^{-1}$. The results are shown in Figure 21 and Table 3.

The failure to fully reproduce the Herschel/SPIRE photometry may be due to the upper bound of U_{\min} (and by extension, dust temperature) being insufficiently large, as BAGPIPES can accommodate only $U_{\min} \leq 25$. Another possibility is that the 3mm photometry is contaminated nontrivially by synchrotron emission, as the radio SED is not included in the model. We also test different choices in SFH (a single burst model and an exponential+burst model), but find no significant improvement over the single exponential model. With the exponential+burst model, SFR is reduced by $\lesssim 5\%$ (within statistical uncertainties).

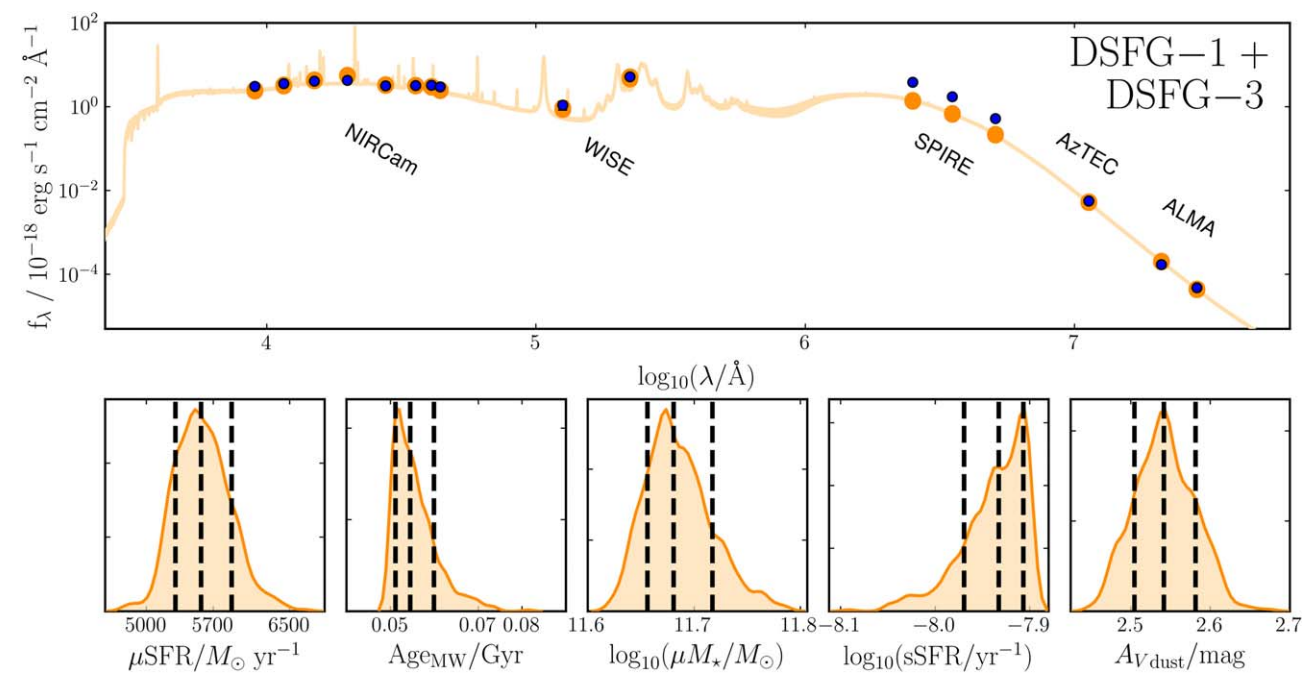


Figure 21. Top panel: combined SED fit for DSFG-1 and DSFG-3 at z=2.236, incorporating unresolved photometry to better constrain the dust SED. Bottom panels: posterior distributions of SFR, mass-weighted age, stellar mass, sSFR, and A_V . SFR and M_{\star} are amplified by lensing magnification; corrected intrinsic values are given in Table 3.

ORCID iDs

Patrick S. Kamieneski https://orcid.org/0000-0001-9394-6732

Brenda L. Frye https://orcid.org/0000-0003-1625-8009 Rogier A. Windhorst https://orcid.org/0000-0001-8156-6281

Kevin C. Harrington https://orcid.org/0000-0001-5429-5762

Min S. Yun https://orcid.org/0000-0001-7095-7543
Allison Noble https://orcid.org/0000-0003-1832-4137
Massimo Pascale https://orcid.org/0000-0002-2282-8795
Nicholas Foo https://orcid.org/0000-0002-7460-8460
Seth H. Cohen https://orcid.org/0000-0003-3329-1337
Rolf A. Jansen https://orcid.org/0000-0003-1268-5230
Timothy Carleton https://orcid.org/0000-0001-6650-2853
Anton M. Koekemoer https://orcid.org/0000-0002-6610-2048

Christopher N. A. Willmer https://orcid.org/0000-0001-9262-9997

Jake S. Summers https://orcid.org/0000-0002-7265-7920
Nikhil Garuda https://orcid.org/0000-0003-3418-2482
Reagen Leimbach https://orcid.org/0009-0001-7446-2350
Benne W. Holwerda https://orcid.org/0000-0002-4884-6756

Justin D. R. Pierel https://orcid.org/0000-0002-2361-7201 Eric F. Jiménez-Andrade https://orcid.org/0000-0002-2640-5917

S. P. Willner https://orcid.org/0000-0002-9895-5758 Belén Alcalde Pampliega https://orcid.org/0000-0002-4140-0428

Amit Vishwas https://orcid.org/0000-0002-4444-8929 William C. Keel https://orcid.org/0000-0002-6131-9539 Q. Daniel Wang https://orcid.org/0000-0002-9279-4041 Cheng Cheng https://orcid.org/0000-0003-0202-0534 Dan Coe https://orcid.org/0000-0001-7410-7669

Christopher J. Conselice https://orcid.org/0000-0003-1949-7638

Jordan C. J. D'Silva https://orcid.org/0000-0002-9816-1931

Simon P. Driver https://orcid.org/0000-0001-9491-7327
Norman A. Grogin https://orcid.org/0000-0001-9440-8872
Tyler Hinrichs https://orcid.org/0009-0008-0376-3771
James D. Lowenthal https://orcid.org/0000-0001-9969-3115

Madeline A. Marshall https://orcid.org/0000-0001-6434-7845

Mario Nonino https://orcid.org/0000-0001-6342-9662
Rafael Ortiz, III https://orcid.org/0000-0002-6150-833X
Alex Pigarelli https://orcid.org/0000-0001-9369-6921
Nor Pirzkal https://orcid.org/0000-0003-3382-5941
Maria del Carmen Polletta https://orcid.org/0000-0001-7411-5386

Aaron S. G. Robotham https://orcid.org/0000-0003-0429-3579

Russell E. Ryan, Jr. https://orcid.org/0000-0003-0894-1588 Haojing Yan https://orcid.org/0000-0001-7592-7714

References

Abdurro'uf, & Akiyama, M. 2017, MNRAS, 469, 2806
Abdurro'uf, & Akiyama, M. 2018, MNRAS, 479, 5083
Abdurro'uf, Coe, D., & Jung, I. 2023, ApJ, 945, 117
Abdurro'uf, Lin, Y.-T., Hirashita, H., et al. 2022a, ApJ, 926, 81
Abdurro'uf, Lin, Y.-T., Hirashita, H., et al. 2022b, ApJ, 935, 98
Abdurro'uf, Lin, Y.-T., Wu, P.-F., & Akiyama, M. 2021, ApJS, 254, 15
Abdurro'uf, Lin, Y.-T., Wu, P.-F., & Akiyama, M., 2022c, piXedfit: Analyze spatially resolved SEDs of galaxies, Astrophysics Source Code Library,

Akhshik, M., Whitaker, K. E., Brammer, G., et al. 2020, ApJ, 900, 184 Alberts, S., & Noble, A. 2022, Univ, 8, 554

Algera, H. S. B., Inami, H., Sommovigo, L., et al. 2024, MNRAS, 527, 6867 Amvrosiadis, A., Lange, S., Nightingale, J., et al. 2024, arXiv:2404.01918 Armus, L., Heckman, T., & Miley, G. 1987, AJ, 94, 831

```
Arrigoni Battaia, F., Chen, C.-C., Fumagalli, M., et al. 2018, A&A, 620, A202
Astropy Collaboration, Price-Whelan, A. M., Lim, P. L., et al. 2022, ApJ,
   935, 167
Astropy Collaboration, Price-Whelan, A. M., Sipőcz, B. M., et al. 2018, AJ,
   156, 123
Astropy Collaboration, Robitaille, T. P., Tollerud, E. J., et al. 2013, A&A,
   558, A33
Baes, M., Verstappen, J., De Looze, I., et al. 2011, ApJS, 196, 22
Baker, W. M., Maiolino, R., Belfiore, F., et al. 2023, MNRAS, 518, 4767
Baker, W. M., Maiolino, R., Bluck, A. F. L., et al. 2022, MNRAS, 510, 3622
Barnes, D. J., Kannan, R., Vogelsberger, M., & Marinacci, F. 2020, MNRAS,
  494, 1143
Barnes, J. E., & Hernquist, L. 1992, ARA&A, 30, 705
Barnes, J. E., & Hernquist, L. E. 1991, ApJL, 370, L65
Barro, G., Kriek, M., Pérez-González, P. G., et al. 2016, ApJL, 827, L32
Barrufet, L., Pearson, C., Serjeant, S., et al. 2020, A&A, 641, A129
Bartelmann, M., & Loeb, A. 1998, ApJ, 503, 48
Battisti, A. J., da Cunha, E., Grasha, K., et al. 2019, ApJ, 882, 61
Beaumont, C., Goodman, A., & Greenfield, P. 2015, in ASP Conf. Ser. 495,
   Astronomical Data Analysis Software an Systems XXIV (ADASS XXIV),
   ed. A. R. Taylor & E. Rosolowsky (San Francisco, CA: ASP), 101
Bell, E. F. 2003, ApJ, 586, 794
Belli, S., Newman, A. B., & Ellis, R. S. 2019, ApJ, 874, 17
Bianchi, S., & Xilouris, E. M. 2011, A&A, 531, L11
Birkin, J. E., Hutchison, T. A., Welch, B., et al. 2023, ApJ, 958, 64
Blain, A. W., Smail, I., Ivison, R. J., Kneib, J.-P., & Frayer, D. T. 2002, PhR,
   369, 111
Bluck, A. F. L., Maiolino, R., Piotrowska, J. M., et al. 2020b, MNRAS,
Bluck, A. F. L., Maiolino, R., Sánchez, S. F., et al. 2020a, MNRAS, 492, 96
Borsato, E., Marchetti, L., Negrello, M., et al. 2024, MNRAS, 528, 6222
Bournaud, F., Daddi, E., Elmegreen, B. G., et al. 2008, A&A, 486, 741
Bournaud, F., Elmegreen, B. G., & Elmegreen, D. M. 2007, ApJ, 670, 237
Bourne, N., Dunlop, J. S., Merlin, E., et al. 2017, MNRAS, 467, 1360
Bouwens, R., González-López, J., Aravena, M., et al. 2020, ApJ, 902, 112
Bradley, L., Sipőcz, B., Robitaille, T., et al. 2022, astropy/photutils: 1.6.0,
   Zenodo, doi:10.5281/zenodo.7419741
Brammer, G. B., Whitaker, K. E., van Dokkum, P. G., et al. 2011, ApJ, 739, 24
Briggs, D. S. 1995, PhD thesis, New Mexico Institute of Mining and
   Technology
Brinchmann, J., Charlot, S., White, S. D. M., et al. 2004, MNRAS, 351, 1151
Bushouse, H., Eisenhamer, J., Dencheva, N., et al. 2023, JWST Calibration
  Pipeline, 1.11.2, Zenodo, doi:10.5281/zenodo.8140011
Bussmann, R. S., Pérez-Fournon, I., Amber, S., et al. 2013, ApJ, 779, 25
Byun, Y. I., Freeman, K. C., & Kylafis, N. D. 1994, ApJ, 432, 114
Calvi, R., Castignani, G., & Dannerbauer, H. 2023, A&A, 678, A15
Calzetti, D. 1997a, in AIP Conf. Ser. 408, The ultraviolet universe at low and
   High redshift, ed. W. H. Waller (Melville, NY: AIP), 403
Calzetti, D. 1997b, AJ, 113, 162
Calzetti, D., Armus, L., Bohlin, R. C., et al. 2000, ApJ, 533, 682
Cañameras, R., Nesvadba, N. P. H., Guery, D., et al. 2015, A&A, 581, A105
Cañameras, R., Nesvadba, N. P. H., Limousin, M., et al. 2018, A&A, 620, A60
Cano-Díaz, M., Ávila-Reese, V., Sánchez, S. F., et al. 2019, MNRAS,
   488, 3929
Cano-Díaz, M., Sánchez, S. F., Zibetti, S., et al. 2016, ApJL, 821, L26
Caputi, K. I., Caminha, G. B., Fujimoto, S., et al. 2021, ApJ, 908, 146
Carilli, C. L., Daddi, E., Riechers, D., et al. 2010, ApJ, 714, 1407
Carnall, A. C., Leja, J., Johnson, B. D., et al. 2019, ApJ, 873, 44
Carnall, A. C., McLure, R. J., Dunlop, J. S., & Davé, R. 2018, MNRAS,
Carrasco, E. R., Conselice, C. J., & Trujillo, I. 2010, MNRAS, 405, 2253
Carrera, R., Gallart, C., Aparicio, A., et al. 2008, AJ, 136, 1039
Casey, C. M. 2016, ApJ, 824, 36
Casey, C. M., Cooray, A., Capak, P., et al. 2015, ApJL, 808, L33
Casey, C. M., Narayanan, D., & Cooray, A. 2014a, PhR, 541, 45
Casey, C. M., Scoville, N. Z., Sanders, D. B., et al. 2014b, ApJ, 796, 95
Ceverino, D., Dekel, A., & Bournaud, F. 2010, MNRAS, 404, 2151
Chapman, S. C., Blain, A., Ibata, R., et al. 2009, ApJ, 691, 560
Chapman, S. C., Smail, I., Windhorst, R., Muxlow, T., & Ivison, R. J. 2004,
   ApJ, 611, 732
Chen, C.-C., Gao, Z.-K., Hsu, Q.-N., et al. 2022, ApJL, 939, L7
Cheng, C., Huang, J.-S., Smail, I., et al. 2023, ApJL, 942, L19
Cheng, C., Yan, H., Huang, J.-S., et al. 2022, ApJL, 936, L19
Chiang, Y.-K., Overzier, R., & Gebhardt, K. 2013, ApJ, 779, 127
Cho, J., Lazarian, A., Honein, A., et al. 2003, ApJL, 589, L77
Clements, D. L., Braglia, F., Petitpas, G., et al. 2016, MNRAS, 461, 1719
```

```
Clements, D. L., Braglia, F. G., Hyde, A. K., et al. 2014, MNRAS, 439, 1193
Coe, D., Umetsu, K., Zitrin, A., et al. 2012, ApJ, 757, 22
Colina, L., Crespo Gómez, A., Álvarez-Márquez, J., et al. 2023, A&A, 673, L6
Condon, J. J. 1992, ARA&A, 30, 575
Cresci, G., Mannucci, F., Maiolino, R., et al. 2010, Natur, 467, 811
Daddi, E., Dickinson, M., Morrison, G., et al. 2007, ApJ, 670, 156
Daddi, E., Elbaz, D., Walter, F., et al. 2010, ApJL, 714, L118
Dahlen, T., Strolger, L.-G., Riess, A. G., et al. 2012, ApJ, 757, 70
Dalcanton, J. J., Yoachim, P., & Bernstein, R. A. 2004, ApJ, 608, 189
Dannerbauer, H., Kurk, J. D., De Breuck, C., et al. 2014, A&A, 570, A55
Davé, R., Finlator, K., & Oppenheimer, B. D. 2012, MNRAS, 421, 98
Davé, R., Finlator, K., Oppenheimer, B. D., et al. 2010, MNRAS, 404, 1355
de Jong, T., Klein, U., Wielebinski, R., & Wunderlich, E. 1985, A&A, 147, L6
Dekel, A., Birnboim, Y., Engel, G., et al. 2009, Natur, 457, 451
Dekel, A., & Burkert, A. 2014, MNRAS, 438, 1870
Devour, B. M., & Bell, E. F. 2017, MNRAS, 468, L31
Devour, B. M., & Bell, E. F. 2019, ApJS, 244, 3
Donevski, D., Damjanov, I., Nanni, A., et al. 2023, A&A, 678, A35
Draine, B. T., & Li, A. 2007, ApJ, 657, 810
Drew, P. M., Casey, C. M., Cooray, A., & Whitaker, K. E. 2020, ApJ, 892, 104
Dudzevičiūtė, U., Smail, I., Swinbank, A. M., et al. 2020, MNRAS, 494, 3828
Dunlop, J. S. 2011, in ASP Conf. Ser. 446, Galaxy Evolution: Infrared to
  Millimeter Wavelength Perspective, ed. W. Wang et al. (San Francisco,
Dunlop, J. S., McLure, R. J., Biggs, A. D., et al. 2017, MNRAS, 466, 861
Elbaz, D., Daddi, E., Le Borgne, D., et al. 2007, A&A, 468, 33
Elbaz, D., Leiton, R., Nagar, N., et al. 2018, A&A, 616, A110
Ellison, S. L., Lin, L., Thorp, M. D., et al. 2021, MNRAS, 501, 4777
Ellison, S. L., Pan, H.-A., Bluck, A. F. L., et al. 2024, MNRAS, 527, 10201
Ellison, S. L., Sánchez, S. F., Ibarra-Medel, H., et al. 2018, MNRAS,
  474, 2039
Elmegreen, B. G. 2011, ApJ, 737, 10
Elmegreen, B. G., Bournaud, F., & Elmegreen, D. M. 2008, ApJ, 688, 67
Engelbracht, C. W., Rieke, M. J., Rieke, G. H., Kelly, D. M., &
  Achtermann, J. M. 1998, ApJ, 505, 639
Enia, A., Negrello, M., Gurwell, M., et al. 2018, MNRAS, 475, 3467
Enia, A., Rodighiero, G., Morselli, L., et al. 2020, MNRAS, 493, 4107
Erroz-Ferrer, S., Carollo, C. M., den Brok, M., et al. 2019, MNRAS, 484, 5009
Estrada-Carpenter, V., Papovich, C., Momcheva, I., et al. 2020, ApJ, 898, 171
Fang, J. J., Faber, S. M., Koo, D. C., & Dekel, A. 2013, ApJ, 776, 63
Farrah, D., Lonsdale, C. J., Borys, C., et al. 2006, ApJL, 641, L17
Ferland, G. J., Chatzikos, M., Guzmán, F., et al. 2017, RMxAA, 53, 385
Ferrara, A., Ferrini, F., Franco, J., & Barsella, B. 1991, ApJ, 381, 137
Finlator, K., Davé, R., Papovich, C., & Hernquist, L. 2006, ApJ, 639, 672
Förster Schreiber, N. M., Genzel, R., Lutz, D., Kunze, D., & Sternberg, A.
  2001, ApJ, 552, 544
Franx, M., & Illingworth, G. 1990, ApJL, 359, L41
Frye, B., Pascale, M., Cohen, S., et al. 2023, TNSAN, 96
Frye, B. L., Pascale, M., Pierel, J., et al. 2024, ApJ, 961, 171
Frye, B. L., Pascale, M., Qin, Y., et al. 2019, ApJ, 871, 51
Fujimoto, S., Ouchi, M., Shibuya, T., & Nagai, H. 2017, ApJ, 850, 83
Geach, J. E., Smail, I., Ellis, R. S., et al. 2006, ApJ, 649, 661
Genzel, R., Förster Schreiber, N. M., Lang, P., et al. 2014, ApJ, 785, 75
Giménez-Arteaga, C., Fujimoto, S., Valentino, F., et al. 2024, A&A, 686, A63
Giménez-Arteaga, C., Oesch, P. A., Brammer, G. B., et al. 2023, ApJ, 948, 126
Gomez, H. L., Baes, M., Cortese, L., et al. 2010, A&A, 518, L45
González Delgado, R. M., Cid Fernandes, R., Pérez, E., et al. 2016, A&A,
  590, A44
Griffin, M. J., Abergel, A., Abreu, A., et al. 2010, A&A, 518, L3
Gullberg, B., Smail, I., Swinbank, A. M., et al. 2019, MNRAS, 490, 4956
Hainline, L. J., Blain, A. W., Smail, I., et al. 2011, ApJ, 740, 96
Hales, C. A., Murphy, T., Curran, J. R., et al. 2012, MNRAS, 425, 979
Hall, C., Courteau, S., Jarrett, T., et al. 2018, ApJ, 865, 154
Hani, M. H., Hayward, C. C., Orr, M. E., et al. 2020, MNRAS, 493, L87
Harikane, Y., Ouchi, M., Ono, Y., et al. 2019, ApJ, 883, 142
Harrington, K. C., Weiss, A., Yun, M. S., et al. 2021, ApJ, 908, 95
Harrington, K. C., Yun, M. S., Cybulski, R., et al. 2016, MNRAS, 458, 4383
Hatsukade, B., Tamura, Y., Iono, D., et al. 2015, PASJ, 67, 93
Hayward, C. C., Jonsson, P., Kereš, D., et al. 2012, MNRAS, 424, 951
Hayward, C. C., Kereš, D., Jonsson, P., et al. 2011, ApJ, 743, 159
Hayward, C. C., Narayanan, D., Kereš, D., et al. 2013, MNRAS, 428, 2529
Heckman, T. M., Armus, L., & Miley, G. K. 1990, ApJS, 74, 833
Heckman, T. M., & Thompson, T. A. 2017, in Handbook of Supernovae, ed.
   A. W. Alsabti & P. Murdin (Berlin: Springer), 2431
Helou, G., Soifer, B. T., & Rowan-Robinson, M. 1985, ApJL, 298, L7
Hemmati, S., Miller, S. H., Mobasher, B., et al. 2014, ApJ, 797, 108
```

```
Hennawi, J. F., Prochaska, J. X., Cantalupo, S., & Arrigoni-Battaia, F. 2015,
   Sci, 348, 779
Hernquist, L. 1989, Natur, 340, 687
Hodge, J. A., Carilli, C. L., Walter, F., et al. 2012, ApJ, 760, 11
Hodge, J. A., & da Cunha, E. 2020, RSOS, 7, 200556
Hodge, J. A., Smail, I., Walter, F., et al. 2019, ApJ, 876, 130
Hodge, J. A., Swinbank, A. M., Simpson, J. M., et al. 2016, ApJ, 833, 103
Högbom, J. A. 1974, A&AS, 15, 417
Holwerda, B. W., Dalcanton, J. J., Radburn-Smith, D., et al. 2012, ApJ, 753, 25
Holwerda, B. W., Knabel, S., Steele, R. C., et al. 2021, MNRAS, 505, 1316
Hopkins, P. F., Hernquist, L., Cox, T. J., & Kereš, D. 2008, ApJS, 175, 356
Hounsell, R., Scolnic, D., Foley, R. J., et al. 2018, ApJ, 867, 23
Howk, J. C., & Savage, B. D. 2000, AJ, 119, 644
Hsieh, B. C., Lin, L., Lin, J. H., et al. 2017, ApJL, 851, L24
Hung, C.-L., Casey, C. M., Chiang, Y.-K., et al. 2016, ApJ, 826, 130
Ikarashi, S., Ivison, R. J., Caputi, K. I., et al. 2015, ApJ, 810, 133
Ivison, R. J., Papadopoulos, P. P., Smail, I., et al. 2011, MNRAS, 412, 1913
Ivison, R. J., Smail, I., Papadopoulos, P. P., et al. 2010, MNRAS, 404, 198
Jafariyazani, M., Mobasher, B., Hemmati, S., et al. 2019, ApJ, 887, 204 Jain, S., Tacchella, S., & Mosleh, M. 2024, MNRAS, 527, 3291
Jansen, R. A., Knapen, J. H., Beckman, J. E., Peletier, R. F., & Hes, R. 1994,
   MNRAS, 270, 373
Ji, Z., & Giavalisco, M. 2022, ApJ, 935, 120
Ji, Z., & Giavalisco, M. 2023, ApJ, 943, 54
Ji, Z., Williams, C. C., Tacchella, S., et al. 2023, arXiv:2305.18518
Johnson, T. L., Sharon, K., Bayliss, M. B., et al. 2014, ApJ, 797, 48
Jullo, E., & Kneib, J.-P. 2009, MNRAS, 395, 1319
Jullo, E., Kneib, J.-P., Limousin, M., et al. 2007, NJPh, 9, 447
Kalita, B. S., Silverman, J. D., Daddi, E., et al. 2024, ApJ, 960, 25
Kamieneski, P. S., Frye, B. L., Pascale, M., et al. 2023, ApJ, 955, 91
Kamieneski, P. S., Yun, M. S., Harrington, K. C., et al. 2024, ApJ, 961, 2
Kannan, R., Vogelsberger, M., Marinacci, F., et al. 2021, MNRAS, 503, 336
Kassiola, A., & Kovner, I. 1993, ApJ, 417, 450
Keel, W. C., Cohen, S. H., Windhorst, R. A., & Waddington, I. 1999, AJ,
   118, 2547
Keel, W. C., & White, R. R. I. 2001, AJ, 122, 1369
Keeton, C. R., & Kochanek, C. S. 1998, ApJ, 495, 157
Kereš, D., Katz, N., Weinberg, D. H., & Davé, R. 2005, MNRAS, 363, 2
Kewley, L. J., Rupke, D., Zahid, H. J., Geller, M. J., & Barton, E. J. 2010,
     p.II., 721, I.48
Kneib, J.-P., Ellis, R. S., Smail, I., Couch, W. J., & Sharples, R. M. 1996, ApJ,
   471, 643
Kneib, J. P., Mellier, Y., Fort, B., & Mathez, G. 1993, A&A, 273, 367
Kokorev, V., Jin, S., Magdis, G. E., et al. 2023, ApJL, 945, L25
Koprowski, M. P., Dunlop, J. S., Michałowski, M. J., et al. 2016, MNRAS,
   458, 4321
Kriek, M., van Dokkum, P. G., Labbé, I., et al. 2009, ApJ, 700, 221
Kron, R. G. 1980, ApJS, 43, 305
Kroupa, P. 2001, MNRAS, 322, 231
Labbé, I., Huang, J., Franx, M., et al. 2005, ApJL, 624, L81
Lang, P., Schinnerer, E., Smail, I., et al. 2019, ApJ, 879, 54
Le Bail, A., Daddi, E., Elbaz, D., et al. 2024, A&A, 688, A53
Leaman, J., Li, W., Chornock, R., & Filippenko, A. V. 2011, MNRAS,
   412, 1419
Leja, J., Tacchella, S., & Conroy, C. 2019, ApJL, 880, L9
Leroy, A. K., Walter, F., Brinks, E., et al. 2008, AJ, 136, 2782
Lewis, G. F., Carilli, C., Papadopoulos, P., & Ivison, R. J. 2002, MNRAS,
   330, L15
Lilly, S. J., Eales, S. A., Gear, W. K. P., et al. 1999, ApJ, 518, 641
Limousin, M., Kneib, J.-P., & Natarajan, P. 2005, MNRAS, 356, 309
Limousin, M., Richard, J., Kneib, J. P., et al. 2008, A&A, 489, 23
Lin, L., Pan, H.-A., Ellison, S. L., et al. 2019, ApJL, 884, L33
Lisenfeld, U., Voelk, H. J., & Xu, C. 1996, A&A, 314, 745
Liu, Q., Wang, E., Lin, Z., et al. 2018, ApJ, 857, 17
Liu, Z., Silverman, J. D., Daddi, E., et al. 2024, ApJ, 968, 15
Long, A. S., Casey, C. M., Lagos, C. D. P., et al. 2023, ApJ, 953, 11
Long, A. S., Cooray, A., Ma, J., et al. 2020, ApJ, 898, 133
Lonsdale, C. J., Farrah, D., & Smith, H. E. 2006, in Astrophysics Update 2, ed.
   J. Mason (Berlin: Springer), 285
Lotz, J. M., Koekemoer, A., Coe, D., et al. 2017, ApJ, 837, 97
Mac Low, M.-M., McCray, R., & Norman, M. L. 1989, ApJ, 337, 141
Madau, P., & Dickinson, M. 2014, ARA&A, 52, 415
Magdis, G. E., Bureau, M., Stott, J. P., et al. 2016, MNRAS, 456, 4533
Magdis, G. E., Gobat, R., Valentino, F., et al. 2021, A&A, 647, A33
Magnelli, B., Elbaz, D., Chary, R. R., et al. 2011, A&A, 528, A35
Magnelli, B., Lutz, D., Santini, P., et al. 2012, A&A, 539, A155
```

```
Maoz, D., & Mannucci, F. 2012, PASA, 29, 447
Maragkoudakis, A., Zezas, A., Ashby, M. L. N., & Willner, S. P. 2017,
         S, 466, 1192
Martig, M., Bournaud, F., Teyssier, R., & Dekel, A. 2009, ApJ, 707, 250
Mattila, S., Dahlen, T., Efstathiou, A., et al. 2012, ApJ, 756, 111
Mattila, S., & Meikle, W. P. S. 2001, MNRAS, 324, 325
McDonough, B., Curtis, O., & Brainerd, T. G. 2023, ApJ, 958, 19
McLure, R. J., Dunlop, J. S., Cullen, F., et al. 2018, MNRAS, 476, 3991
McMullin, J. P., Waters, B., Schiebel, D., Young, W., & Golap, K. 2007, in
   ASP Conf. Ser. 376, Astronomical Data Analysis Software and Systems
  XVI, ed. R. A. Shaw, F. Hill, & D. J. Bell (San Francisco, CA: ASP), 127
Medling, A. M., Cortese, L., Croom, S. M., et al. 2018, MNRAS, 475, 5194
Meneghetti, M., Natarajan, P., Coe, D., et al. 2017, MNRAS, 472, 3177
Michałowski, M. J., Dunlop, J. S., Cirasuolo, M., et al. 2012, A&A, 541, A85
Michałowski, M. J., Hayward, C. C., Dunlop, J. S., et al. 2014, A&A, 571, A75
Miettinen, O., Novak, M., Smolčić, V., et al. 2015, A&A, 584, A32
Miley, G., & De Breuck, C. 2008, A&ARv, 15, 67
Miller, T. B., Chapman, S. C., Aravena, M., et al. 2018, Natur, 556, 469
Miller, T. B., Whitaker, K. E., Nelson, E. J., et al. 2022, ApJL, 941, L37
Mishurov, Y. N., Acharova, I. A., Shevchenko, M. G., & Tyshlangov, D. A.
  2014, AstBu, 69, 21
Mollá, M., Ferrini, F., & Díaz, A. I. 1997, ApJ, 475, 519
Möllenhoff, C., Popescu, C. C., & Tuffs, R. J. 2006, A&A, 456, 941
Morselli, L., Rodighiero, G., Enia, A., et al. 2020, MNRAS, 496, 4606
Mosenkov, A. V., Usachev, P. A., Shakespear, Z., et al. 2022, MNRAS,
Murphy, E. J., Braun, R., Helou, G., et al. 2006a, ApJ, 638, 157
Murphy, E. J., Helou, G., Braun, R., et al. 2006b, ApJL, 651, L111
Murray, N., Quataert, E., & Thompson, T. A. 2005, ApJ, 618, 569
Muzzin, A., Marchesini, D., Stefanon, M., et al. 2013, ApJ, 777, 18
Nagy, D., Dessauges-Zavadsky, M., Richard, J., et al. 2022, A&A, 657, A25
Narayanan, D., Davé, R., Johnson, B. D., et al. 2018, MNRAS, 474, 1718
Nelson, E. J., Tacchella, S., Diemer, B., et al. 2021, MNRAS, 508, 219
Nelson, E. J., Tadaki, K.-i., Tacconi, L. J., et al. 2019, ApJ, 870, 130
Newman, A. B., Belli, S., Ellis, R. S., & Patel, S. G. 2018, ApJ, 862, 125
Noeske, K. G., Faber, S. M., Weiner, B. J., et al. 2007b, ApJL, 660, L47
Noeske, K. G., Weiner, B. J., Faber, S. M., et al. 2007a, ApJL, 660, L43
Nomoto, K. 1984, ApJ, 277, 791
Norman, C. A., & Ikeuchi, S. 1989, ApJ, 345, 372
Overzier, R. A. 2016, A&ARv, 24, 14
Pacifici, C., Iyer, K. G., Mobasher, B., et al. 2023, ApJ, 944, 141
Pantoni, L., Massardi, M., Lapi, A., et al. 2021, MNRAS, 507, 3998
Pascale, M., Frye, B. L., Dai, L., et al. 2022, ApJ, 932, 85
Pascale, M., Frye, B. L., Pierel, J. D. R., et al. 2024, arXiv:2403.18902
Pastrav, B. A., Popescu, C. C., Tuffs, R. J., & Sansom, A. E. 2013, A&A,
Peng, B., Vishwas, A., Stacey, G., et al. 2023, ApJL, 944, L36
Pessa, I., Schinnerer, E., Belfiore, F., et al. 2021, A&A, 650, A134
Pessa, I., Schinnerer, E., Leroy, A., et al. 2022, A&A, 663, A61
Petrushevska, T. 2020, Symm, 12, 1966
Petrushevska, T., Okamura, T., Kawamata, R., et al. 2018, ARep, 62, 917
Pierel, J. D. R., Frye, B. L., Pascale, M., et al. 2024b, ApJ, 967, 50
Pierel, J. D. R., Newman, A. B., Dhawan, S., et al. 2024a, ApJL, 967, L37
Pilkington, K., Few, C. G., Gibson, B. K., et al. 2012, A&A, 540, A56
Polletta, M., Nonino, M., Frye, B., et al. 2023, A&A, 675, L4
Popescu, C. C., Misiriotis, A., Kylafis, N. D., Tuffs, R. J., & Fischera, J. 2000,
  A&A, 362, 138
Popping, G., Pillepich, A., Calistro Rivera, G., et al. 2022, MNRAS, 510, 3321
Ramakrishnan, V., Moon, B., Im, S. H., et al. 2023, ApJ, 951, 119
Renzini, A., & Peng, Y.-j. 2015, ApJL, 801, L29
Richie, H. M., Schneider, E. E., Abruzzo, M. W., & Torrey, P. 2024,
  arXiv:2403.03711
Richmond, M. W., Filippenko, A. V., & Galisky, J. 1998, PASP, 110, 553
Robertson, C., Holwerda, B., Young, J., et al. 2024, AJ, 167, 263
Robitaille, T. 2019, APLpy v2.0: The Astronomical Plotting Library in Python
   v2.0, Zenodo, doi:10.5281/zenodo.2567476
Robitaille, T., Beaumont, C., Qian, P., Borkin, M., & Goodman, A. 2017,
   glueviz v0.13.1: multidimensional data exploration v0.13.1, Zenodo, doi:10.
   5281/zenodo.1237692
Robitaille, T., & Bressert, E., 2012 APLpy: Astronomical Plotting Library in
  Python, Astrophysics Source Code Library, ascl:1208.017
Robotham, A. S. G., D'Silva, J. C. J., Windhorst, R. A., et al. 2023, PASP,
   135, 085003
Rodighiero, G., Daddi, E., Baronchelli, I., et al. 2011, ApJL, 739, L40
Rodney, S. A., Brammer, G. B., Pierel, J. D. R., et al. 2021, NatAs, 5, 1118
```

Maller, A. H., Flores, R. A., & Primack, J. R. 1997, ApJ, 486, 681

```
Rowlands, K., Dunne, L., Maddox, S., et al. 2012, MNRAS, 419, 2545
Rudnick, L., & Owen, F. N. 1977, AJ, 82, 1
Rujopakarn, W., Rieke, G. H., Eisenstein, D. J., & Juneau, S. 2011, ApJ,
Rujopakarn, W., Williams, C. C., Daddi, E., et al. 2023, ApJL, 948, L8
Safarzadeh, M., Hayward, C. C., & Ferguson, H. C. 2017, ApJ, 840, 15
Salim, S. 2014, SerAJ, 189, 1
Salim, S., Rich, R. M., Charlot, S., et al. 2007, ApJS, 173, 267
Salpeter, E. E. 1955, ApJ, 121, 161
Sánchez, S. F., Rosales-Ortega, F. F., Jungwiert, B., et al. 2013, A&A,
Sanders, D. B., & Mirabel, I. F. 1996, ARA&A, 34, 749
Sanders, D. B., Soifer, B. T., Elias, J. H., et al. 1988, ApJ, 325, 74
Sargent, M. T., Béthermin, M., Daddi, E., & Elbaz, D. 2012, ApJL, 747, L31
Scannapieco, E., & Bildsten, L. 2005, ApJL, 629, L85
Schaye, J., Crain, R. A., Bower, R. G., et al. 2015, MNRAS, 446, 521
Schreiber, C., Glazebrook, K., Nanayakkara, T., et al. 2018, A&A, 618, A85
Seon, K.-i., Witt, A. N., Shinn, J.-h., & Kim, I.-j. 2014, ApJL, 785, L18
Sharda, P., Federrath, C., da Cunha, E., Swinbank, A. M., & Dye, S. 2018,
   MNRAS, 477, 4380
Sharma, S., Richard, J., Yuan, T., et al. 2018, MNRAS, 481, 1427
Sharon, C. E., Tagore, A. S., Baker, A. J., et al. 2019, ApJ, 879, 52
Shen, S., Mo, H. J., White, S. D. M., et al. 2003, MNRAS, 343, 978
Shivaei, I., Reddy, N. A., Steidel, C. C., & Shapley, A. E. 2015, ApJ, 804, 149
Shu, Y., Bolton, A. S., Mao, S., et al. 2018, ApJ, 864, 91
Simpson, J. M., Smail, I., Swinbank, A. M., et al. 2015, ApJ, 799, 81
Smail, I., Dudzevičiūtė, U., Gurwell, M., et al. 2023, ApJ, 958, 36
Smith, D. J. B., & Hayward, C. C. 2018, MNRAS, 476, 1705
Smith, M., Nichol, R. C., Dilday, B., et al. 2012, ApJ, 755, 61
Snijders, L., Kewley, L. J., & van der Werf, P. P. 2007, ApJ, 669, 269
Soifer, B. T., Neugebauer, G., & Houck, J. R. 1987, ARA&A, 25, 187
Song, J., Fang, G., Lin, Z., Gu, Y., & Kong, X. 2023, ApJ, 958, 82
Sorba, R., & Sawicki, M. 2015, MNRAS, 452, 235
Sorba, R., & Sawicki, M. 2018, MNRAS, 476, 1532
Speagle, J. S., Steinhardt, C. L., Capak, P. L., & Silverman, J. D. 2014, ApJS,
   214, 15
Spitzer, L. 1978, Physical Processes in the Interstellar Medium (New York:
   Wiley)
Steidel, C. C., Adelberger, K. L., Shapley, A. E., et al. 2000, ApJ, 532, 170
Stein, Y., Dettmar, R. J., Beck, R., et al. 2020, A&A, 639, A111
Stockton, A. 1990, in International Conf. on Dynamics and Interactions of
   Galaxies, ed. R. Wielen (Berlin: Springer), 440
Strolger, L.-G., Dahlen, T., Rodney, S. A., et al. 2015, ApJ, 813, 93
Suess, K. A., Bezanson, R., Nelson, E. J., et al. 2022, ApJL, 937, L33
Suess, K. A., Williams, C. C., Robertson, B., et al. 2023, ApJL, 956, L42
Sun, F., Helton, J. M., Egami, E., et al. 2024, ApJ, 961, 69
Suyu, S. H., Marshall, P. J., Auger, M. W., et al. 2010, ApJ, 711, 201
Swinbank, A. M., Dye, S., Nightingale, J. W., et al. 2015, ApJL, 806, L17
Tacchella, S., Carollo, C. M., Förster Schreiber, N. M., et al. 2018, ApJ,
  859, 56
Tacchella, S., Carollo, C. M., Renzini, A., et al. 2015, Sci, 348, 314
Tacchella, S., Dekel, A., Carollo, C. M., et al. 2016a, MNRAS, 458, 242
Tacchella, S., Dekel, A., Carollo, C. M., et al. 2016b, MNRAS, 457, 2790
Tadaki, K., Iono, D., Yun, M. S., et al. 2018, Natur, 560, 613
Tadaki, K.-i., Genzel, R., Kodama, T., et al. 2017, ApJ, 834, 135
```

```
Targett, T. A., Dunlop, J. S., Cirasuolo, M., et al. 2013, MNRAS, 432, 2012
Thompson, T. A., Fabian, A. C., Quataert, E., & Murray, N. 2015, MNRAS,
  449, 147
Thompson, T. W. J., Howk, J. C., & Savage, B. D. 2004, AJ, 128, 662
Thomson, A. P., Smail, I., Swinbank, A. M., et al. 2019, ApJ, 883, 204
Thornley, M. D., Förster Schreiber, N. M., Lutz, D., et al. 2000, ApJ, 539, 641
Toft, S., Smolčić, V., Magnelli, B., et al. 2014, ApJ, 782, 68
Trayford, J. W., & Schaye, J. 2019, MNRAS, 485, 5715
Treu, T., & Marshall, P. J. 2016, A&ARv, 24, 11
Treu, T., Suyu, S. H., & Marshall, P. J. 2022, A&ARv, 30, 8
Tsujimoto, T., Yoshii, Y., Nomoto, K., et al. 1997, ApJ, 483, 228
Tuffs, R. J., Popescu, C. C., Völk, H. J., Kylafis, N. D., & Dopita, M. A. 2004,
     &A, 419, 821
Umehata, H., Tamura, Y., Kohno, K., et al. 2015, ApJL, 815, L8
van der Kruit, P. C. 1971, A&A, 15, 110
van der Wel, A., Franx, M., van Dokkum, P. G., et al. 2014, ApJ, 788, 28
van Dokkum, P. G., Whitaker, K. E., Brammer, G., et al. 2010, ApJ, 709, 1018
Veilleux, S., Maiolino, R., Bolatto, A. D., & Aalto, S. 2020, A&ARv, 28, 2
Venemans, B. P., Röttgering, H. J. A., Miley, G. K., et al. 2007, A&A,
  461, 823
Venkatesan, T. C. A., Batuski, D. J., Hanisch, R. J., & Burns, J. O. 1994, ApJ,
  436, 67
Vorobyov, E. I., & Shchekinov, Y. A. 2006, NewA, 11, 240
Vulcani, B., Poggianti, B. M., Moretti, A., et al. 2019, MNRAS, 488, 1597
Wang, Q. D., Immler, S., Walterbos, R., Lauroesch, J. T., & Breitschwerdt, D.
  2001, ApJL, 555, L99
Whitaker, K. E., Franx, M., Bezanson, R., et al. 2015, ApJL, 811, L12
Whitaker, K. E., Labbé, I., van Dokkum, P. G., et al. 2011, ApJ, 735, 86
Whitaker, K. E., Pope, A., Cybulski, R., et al. 2017, ApJ, 850, 208
Whitaker, K. E., van Dokkum, P. G., Brammer, G., & Franx, M. 2012, ApJL,
  754, L29
Williams, C. C., Labbe, I., Spilker, J., et al. 2019, ApJ, 884, 154
Williams, R. J., Quadri, R. F., Franx, M., van Dokkum, P., & Labbé, I. 2009,
   ApJ, 691, 1879
Wilson, G. W., Austermann, J. E., Perera, T. A., et al. 2008, MNRAS, 386, 807
Windhorst, R. A., Cohen, S. H., Jansen, R. A., et al. 2023, AJ, 165, 13
Wise, E., Jogee, S., & Guo, Y. 2022, in ASP. Conf. Ser. 525, Compendium of
  Undergraduate Research in Astronomy and Space Science, ed. J. Jensen,
  J. Barnes, & B. Wardell (San Francisco, CA: ASP)
Wright, E. L. 2006, PASP, 118, 1711
Wright, E. L., Eisenhardt, P. R. M., Mainzer, A. K., et al. 2010, AJ, 140, 1868
Wuyts, S., Förster Schreiber, N. M., Genzel, R., et al. 2012, ApJ, 753, 114
Wuyts, S., Förster Schreiber, N. M., Nelson, E. J., et al. 2013, ApJ, 779,
Wuyts, S., Labbé, I., Franx, M., et al. 2007, ApJ, 655, 51
Yao, Y., Chen, G., Liu, H., et al. 2022, A&A, 661, A112
Young, D. R., Smartt, S. J., Mattila, S., et al. 2008, A&A, 489, 359
Yun, M. S., Reddy, N. A., & Condon, J. J. 2001, ApJ, 554, 803
Zavala, J. A., Casey, C. M., Manning, S. M., et al. 2021, ApJ, 909, 165
Zibetti, S., Charlot, S., & Rix, H.-W. 2009, MNRAS, 400, 1181
Ziegler, J. J., Edwards, T. D. P., Suliga, A. M., et al. 2022, MNRAS, 517, 2471
Zimmerman, D. T., Narayanan, D., Whitaker, K. E., & Davè, R. 2024,
  arXiv:2401.06719
Zolotov, A., Dekel, A., Mandelker, N., et al. 2015, MNRAS, 450, 2327
Zwicky, F. 1938, ApJ, 88, 529
```